UNIVERSITY OF SOUTHAMPTON

FACULTY OF ENGINEERING AND THE ENVIRONMENT

INSTITUTE OF SOUND AND VIBRATION RESEARCH

Nonlinear Signal Processing Techniques for Signal Detection

by

Julian Leslie Deeks

Thesis for the degree of Doctor of Philosophy

November 2017

UNIVERSITY OF SOUTHAMPTON

ABSTRACT

FACULTY OF ENGINEERING AND THE ENVIRONMENT

Institute of Sound and Vibration Research

Doctor of Philosophy

NONLINEAR SIGNAL PROCESSING TECHNIQUES FOR SIGNAL DETECTION

by Julian Leslie Deeks

The performance of underwater acoustic signal detection schemes can be reduced by extremes of variability in the input signal. Linear detectors such as spectral amplitude thresholding or matched filtering often show degrading detection performance as the power in the signal of interest reduces compared to the noise. Recently, literature examining weak signal detection has focused on exploiting nonlinear system models such as the Duffing equation, to improve detection. The applications in the literature include non-destructive testing, tool wear indication and seismic activity detection. However, not much attention has been paid to their application to underwater signal detection, and importantly very little is published on robust and comprehensive detection performance assessment. Two nonlinear mechanisms found in the Langevin system and the Duffing system, Stochastic Resonance and a transition from chaotic to stable motion, are examined in this thesis, as signal conditioning tools. Using Receiver Operating Characteristics analysis the detection performance is, for the first time, comprehensively measured for different input noise distributions and for different nonlinear pre-processing system configurations. A novel replica correlation detector is devised, that exploits a property of the stable motion in the normalised Duffing system. The often claimed noise immunity of nonlinear systems is refuted; the findings in this thesis strongly show that performance degrades with increasing noise in a similar to linear detectors. However it is also shown that under certain configuration conditions the Duffing transition mechanism generates better detection performance than a benchmark linear detector, when the signal of interest is mixed with highly impulsive real biological snapping shrimp noise.

Contents

List of Figures

DECLARATION OF AUTHORSHIP

I, Julian Leslie Deeks, declare that the thesis entitled Nonlinear Signal Processing Techniques for Signal Detection and the work presented in the thesis are both my own, and have been generated by me as the result of my own original research. I confirm that:

- This work was done wholly while in candidature for a research degree at this University;
- where any part of this thesis has previously been submitted for a degree or any other qualification at this University or any other institution, this has been clearly stated;
- where I have consulted the published work of others, this is always clearly attributed;
- where I have quoted from the work of others, the source is always given. With the exception of such quotations, this thesis is entirely my own work;
- I have acknowledged all main sources of help;
- where the thesis is based on the work done by myself jointly with others, I have made clear exactly what was done by others and what I contributed myself;
- parts of this work have been published as:

Signed

Date

November 2017

Acknowledgements

First of all I must pass on my sincere gratitude to Prof. Paul White my main supervisor, and to Dr. Gary Heald my workplace PhD supervisor. The support, encouragement, quiet expertise, patience and confidence bolstering they have shown me has been staggering and will never be forgotten. I must also thank many other staff at the Institute for Sound and Vibration Research at the University of Southampton, for granting me the much needed additional time to complete my PhD. As a full time employee at the Defence Science and Technology Laboratory (Dstl) based at Portsdown West above Portsmouth, it has been incredibly hard to perform my duties at work as well as complete a PhD part time. I knew it would be tough but quite how difficult, was a surprise. Consequently I had to carry out constant management of the expectations of a great many of my work colleagues. Fortunately my efforts were successful because in return they have shown extraordinary support for me, and they certainly had no obligation to do so. I must therefore extend a massive thank you to my senior managers who have offered encouragement and practical support in many forms. First, I must thank Peter Evans who first suggested I do a Phd, secondly I'd like to thank Richard Windell the then Group Leader for agreeing to fund 15 days a year for my time on the PhD. ("Julian I can offer you 10 days", "Richard I was hoping for 20", "How about 15?", "Done!"). My Team Leaders over the years; Dr. Jon Locke in particular, and most of all my current Team Leader, Trevor Gladwell. Trevor has bent over backwards to support me and ensure I have the time and space to work, thanks Trevor. I must also mention two of my Dstl Project Managers who have also offered time and other encouragements to ease the journey; Simon Corfield and Sharon Williams. In the last two years I have also

received considerable support from my current Group Leader, fortunately Dr. Robert Syddell "gets it" as to why I wanted to complete this PhD. As a result Rob has always supported my requests for time off work and has often enquired how things were progressing, with a knowing twinkle in his eye. Thanks Rob.
There are a host of other people who have helped me considerably, often unwittingly. The help has been in various forms such as; proof reading, checking my mathematics (Thank you Dr. Duleep Wikramasinghe and Brian Runyard!), idle discussions over coffee that sparked an idea, expressions of real interest in my topic, friendly enquiries as to progress and even just a friendly face at low points. All of these have been an incredible help. For all these, I thank: Nick Felgate, Dr. Amanda Page, Dr. Geoff Steel, Dr. Phil Bardswell, Gary Wood, Dr. Duncan Williams, Paddy Kennedy, Martin Litchfield, Mark Brown, Angela Brown, Wendy and Bob Stent, Barry Deeks, Aisling Gallagher-Deeks, Prof. Tim Leighton, Dr. Stephan Weiss and many more. And I save the final word to Prof. Paul White and Gary Heald. The humorous "duffings-up" you have given me as a double act over the years were so good I think you should both be on the stage .... there is one leaving in five minutes!

Acronyms

AUC	Area Under Curve (ROC analysis)
CDF	Cumulative Density Function
DAE	Duffing Array Element
FFT	Fast Fourier Transform
FPR	False Positive Rate
ISVR	Institute of Sound and Vibration Research
K-S	Kolmogorov-Smirnov (CDF pair similarity test)
LRT	Linear Response Theory
PDF	Probability Density Function
RK4	Runge-Kutta fourth order fixed step numerical method
ROC	Receiver Operating Characteristic
SOI	Signal of Interest, the wanted signal component
S/N	Signal to Noise Ratio
SHM	Simple Harmonic Motion
SR	Stochastic Resonance
TFR	Time Frequency Representation (transforms)
TPR	True Positive Rate

Mathematical notation

c_m	Maximal correlation coefficient
d	Threshold value
h	Runge-Kutta step size
l_1	Arbitrary force integration upper distance limit
L_2	Arbitrary force integration lower distance limit
n_m	Signal model: unwanted or 'noise' component
p	Generalised system parameter (for example; amplitude)
p	Grebogi transient length model, generic system parameter
p_c	Grebogi transient length model, critical transition value
p_c	Threshold value at which the strange attractor disappears
q	Rung-Kutta order
r_k	Average stochastic transition rate (Kramers)
s	Input signal model as in: $s(t) = Acos(\omega t) + n$
s_m	Signal model: wanted component
t	Time
t_0	Start time
x	Displacement
x_0	Initial condition, displacement
x_1	Lorenz system variable: proportional to convective intensity
x_2	Lorenz system variable: vertical temperature differential
x_3	Lorenz system variable: temperature distortion from linearity

x_a	Displacement output from the Duffing system at phase $\phi = 0$
x_b	Displacement output from the Duffing system at phase $\phi = \frac{\pi}{2}$
x_c	Displacement output from the Duffing system at phase $\phi = \pi$
x_d	Displacement output from the Duffing system at phase $\phi = \frac{3\pi}{2}$
x_h	Filtered displacement/signal
x_m	Signal model: measured signal sample
y_e	Excess kurtosis (excess standard fourth moment)
A	Sinusoidal nonlinear system input, amplitude
A_1	Energy function: first asymmetry controlling parameter
A_2	Energy function: second asymmetry controlling parameter
A_d	Input signal scaling, reference amplitude
A_m	Sinusoidal nonlinear system input, minimum amplitude
A_p	Peak sine wave amplitude amplitude
D	Kramers' rate noise amplitude factor (variance)
D_k	Kolmogorov-Smirnov goodness of fit measure (between two CDF's)
E	Energy in the Duffing system
F_i	Duffing, total input force term
F_n	K-S analysis: input signal, cumulative density function
F_r	K-S analysis: reference cumulative density function
F_s	Duffing restoring force
F_x	K-S analysis: noise-only data, cumulative density function
H_0	Likelihood ratio null or noise-only hypothesis
H_1	Likelihood ratio signal plus noise hypothesis
N	K-S analysis: Number of samples in the PDF
N_p	Measured average noise power, using power spectrum
P_e	Total probability of error in hypothesis selection
P_N	Average noise power

P_S	Average sine wave signal power
P_{FD}	Probability of false detection
P_{FR}	Probability of false rejection
S_p	Measured average signal power, using power spectrum
SNR	Signal to noise (power) ratio, in $\log_{10}$ decibels
snr	Signal to noise (power) ratio
T	Period
T_k	Kramers' time
T_τ	Grebogi model. Average transient time length
V	Potential energy function
X	All possible values of the parameter in a binary hypothesis test
X_0	Second region of the parameter in a binary hypothesis test
X_1	First region of the parameter in a binary hypothesis test
X_h	Fourier transform of the filtered power signal
y	Signal model: displacement
α	Linear term coupling factor
α_l	Lorenz system, Prandtl number
β	Nonlinear term coupling factor
β_l	Lorenz system, dimensionless geometry factor
δ	Damping factor
η	Data precision
η_T	Binary detector probabilities ratio, arbitrary threshold
γ	Nonlinear system internal force term amplitude
γ_c	Nonlinear system internal force term critical amplitude
γ_k	Kramers' rate friction term
μ	Mean
ω	Angular frequency
ω_0	Nonlinear system internal force term angular frequency

ω_b	Kramers' rate frequency of transition at the energy function central barrier
ω_n	Resonant frequency of the unforced nonlinear system
ϕ	Phase difference
ϕ_0	Phase of the internal Duffing periodic force term
ϕ_i	Phase of an input signal
ρ	Lorenz system, Rayleigh number
σ	Standard deviation
σ^2	Variance
τ	Grebogi transient length model, chaotic transient time length
φ	Bistable system energy function asymmetry scaler
ζ	Grebogi transient length model, critical exponent
Γ	Duffing minimum total periodic force transition amplitude (chaos to stable)
Λ	Collected eigenvalues of a system
Φ	Multiple phase values
$\ddot{x}$	Acceleration
$\Delta\omega$	Angular frequency difference
$\Delta\omega_e$	Estimated angular difference frequency (beat frequency)
ΔV	Potential energy barrier height in a bistable system
$\dot{x}$	Velocity
$\dot{x}_0$	Initial condition, velocity
$\dot{x}_a$	Velocity output from the Duffing system at phase $\phi = 0$
$\dot{x}_b$	Velocity output from the Duffing system at phase $\phi = \frac{\pi}{2}$
$\dot{x}_c$	Velocity output from the Duffing system at phase $\phi = \pi$
$\dot{x}_d$	Velocity output from the Duffing system at phase $\phi = \frac{3\pi}{2}$
$\mathcal{L}_\mathcal{R}$	Likelihood ratio

$n(t)$	Time varying generic noise function
$p_0(x_m)$	Null (*absent*) hypothesis, conditional probability density function
$p_1(x_m)$	wanted component *present* hypothesis, condtional probability density function

Chapter 1

Introduction

The detection of acoustic signals underwater, is a goal that is common across many activities including commercial fishing, oceanography, defence, oil industry and sea floor surveying. Various signal and data processing techniques have evolved to improve the detection performance of underwater acoustic systems but it still remains a key goal to improve the ability to separate the 'wanted' weak signal that corresponds to the object to be detected, from the unwanted noise that can arise from many sources underwater. Many techniques have been developed with assumptions of data stationarity (no variation with time in the principle data moments such as mean and variance) and with the assumption of a Gaussian distribution of the background (ambient) acoustic noise.

In the real world, signals of interest are usually unstable and often discontinuous, and the unwanted noise component may have statistics different to the convenient Gaussian distribution. One key cause of instability in acoustic signals underwater is due to the variation in sound speed profile (SSP) with depth. Some SSP's can cause the path of acoustic signals to diffract, which can result in the signal never reaching the receiving sensor. To improve the performance of weak signal detection schemes algorithms are required that take into account these real world characteristics.

The 'conventional' signal processing techniques used in underwater acoustic sensor

systems, such as military sonars, to detect an acoustic signal of interest are almost invariably linear in nature. The type of signals that it might be desirable to detect can be completely coherent, for example a transmitted single tone sine wave. Or they may be largely incoherent such as might be generated by an underwater seismic event. As a result, many linear detection techniques can be thought of as residing somewhere on a spectrum of coherency, that runs from incoherent energy detection schemes at one end, to fully coherent processing at the other end. In this model coherence refers to how periodic or regular, the signal to be detected is.

The success of detection schemes is determined by how well they can separate the signal of interest from the background noise. For coherent signals mixed with incoherent background noise, coherent processing techniques such as matched filtering or frequency transformation and time integration are commonly used. A problem arises with these techniques when the power in the signal is small compared to the power in the background noise. The problem is further compounded when the signals only last for a short time, so that time integration may not offer much benefit in terms of discriminating the signal from the noise. Ultimately most conventional linear detection technique fail progressively as the ratio of the powers worsens and/or the length of time the signal is present, shortens.

Over the last 25 years there has been some interest in exploiting nonlinear systems to aid in detection. A number of claims have been made as to their performance, such as immunity to noise and good success in detecting extremely weak coherent signals at very small signal to noise power ratios. The prospect that these nonlinear systems would perform as well in the case of underwater signal detection has not been examined in any comprehensive way.

1.1 Overview

The goal of this thesis is to investigate the hypothesis that nonlinear system models can be applied to the problem of detecting signals that are sometimes considered 'weak' in the sense that they are very low power compared to the noise. A variety of nonlinear system models exist and the state of the current progress towards successful weak signal detection based on these models is examined in detail in Chapter 2.

The phrase 'nonlinear systems' is broad in its coverage and so requires clarification. In this thesis nonlinear systems refers to those systems that can be modelled as mathematical equations, where those models can be configured to demonstrate repeatable nonlinear behaviours. The use of such equations readily enables their implementation as code in a suitable modelling environment. There are many such nonlinear model available; ranging from the simplest such as the Logistic (or Population) model [1], to the Navier-Stokes equations [2] or Einstein's field equations [3]. In this thesis the work is restricted to using two models that are commonly used in the context of signal detection, and that are relatively easy to solve numerically. These are the Langevin and the Duffing systems.

Early work on chaotic nonlinear systems has claimed successful detections at input signal to noise ratios (S/N) as low as -68dB, and more recent work has claimed a minimum detectable signal with a S/N of -91dB. Although these very low S/N values appear to indicate that nonlinear oscillators may have potential to improve detection it is not always easy to be sure the same definition of S/N has been used across all such claims. The use of the S/N metric alone is often used in the literature as the definitive measure of detection performance. However, the differing definitions of S/N used render it almost impossible to make quantitative comparisons. A standard method of measuring detection performance, that will allow quantitative comparisons to be made, is required. One aim of the thesis therefore, is apply more robust detection performance measures, and to do so for a larger range of input data types,

including real data. Such a comprehensive assessment has not been found in the literature.

1.2 Main developments

The work presented in this thesis can be divided into three main topics; Stochastic Resonance (SR), transition and applications. Each topic has its own chapter; SR is developed and assessed in Chapter 3, the transition from chaos to stable dynamics in the Duffing system is similarly treated, in Chapter 4. In Chapter 5 the transition in the Duffing is more deeply investigated, and two signal detection applications of the mechanism demonstrated. Chapter 3 is devoted to the exploration of the behaviours associated with SR, and their relevance to signal detection. Controlling the occurrence of SR in the Langevin and in the Duffing system is necessary in a practical detection scheme. The chapter demonstrates this, and then develops SR in a form suitable as a signal conditioning stage before detection. The detection performance is then explored for a small selection of simulated input signal types.

The assessment, presented in this thesis, was the most wide ranging quantification of detection performance on a nonlinear based system known to date, using Receiver Operating Characteristic (ROC) analysis. The ROC metric has the property that it is independent of the signal processing scheme it is measuring, in the sense that it collects statistical data in the same way regardless of which detector generated the data. Consequently the performance of very different detectors can therefore be quantitatively compared. The SR assessment presented here is the strongest confirmation known to date that SR is unlikely to provide any detection benefit in underwater acoustic detection applications. Moreover, the comprehensive analysis of output S/N ratio under different input conditions carried out here, undermines the implication present in commonly used SR terminology. A common assertion is that by adding noise to the input of an SR system, there is a nonlinear *beneficial enhancement* in the output S/N at one particular input S/N value. Although output

S/N does rise before falling again, the evidence presented in this thesis, for the first time, proposes that there is no benefit. Rather, that the increase in output S/N represents the system recovering to the equivalent linear system S/N value, from a large nonlinear reduction in output S/N, at lower input S/N values.

The thesis then turns to the second nonlinear mechanism, a transition by the systems dynamics from one dynamic state to another. The investigation of this mechanism as a pre-processing step prior to detection, is the focus of Chapter 4. The Duffing system is the model most used in Chapter 4, chosen over the Langevin system primarily for commonality with previous related published research on similar topics (see for example [4, 5, 6, 7, 8]). The Duffing system has several controlling parameters, that are used to configure the system to initiate distinctly different dynamics states. The specific transition of most interest here is between a low energy chaotic state and the first stable dynamic state, which is explained in detail in Section 4.2.2. One other transition type is briefly investigated in the chapter, between a very low energy unstable periodic state and the same first stable dynamic state.

One of the first tasks of the chapter is to verify that the transition mechanism can be used in detection by confirming the work of previous researchers [4]. The second order, inhomogeneous nonlinear Duffing equation is implemented in the models in this thesis as two first order coupled systems. The inhomogeneous part is comprised of either one, two or three forcing terms, depending on the test being carried out. The system is configured to operate in a lower energy chaotic state until additional energy is added, in the form of two of the forcing terms that represent an input signal. The two force terms of the model represent noise and one sine wave signal of interest. It is the two input force terms that add sufficient energy to trigger the whole system to transition from the low energy chaotic dynamics to the higher energy stable periodic state.

The properties chaos-to-stable transition are extensively explored in the chapter including for the first time, an assessment of a selection of different Duffing

configurations that all lead to the same transition. The impact on detection performance for a small set of input signal types was assessed towards the end of the chapter. The first evidence that a Duffing system configured as a transition pre-processing stage improves detection performance to be quantitatively comparable to a conventional linear detector, under certain conditions, is presented towards the end of the chapter.

The function of detecting a signal can be implemented as a binary decision process. A typical and simple, conventional linear detector might be comprised of the following signal processing steps.

1 Obtain a finite length of a time-series of input signal samples.
2 Perform a discrete Fourier transform into the frequency domain where the signal is now represented by amplitude versus frequency.
3 Select all frequency bins where the amplitude is larger than a fixed threshold.

The detector has 'decided' there is a signal present in those few bins with over-threshold amplitudes. Unfortunately it is the case that sometimes there is not a signal present at the frequency, and the high amplitude was caused by unwanted random background noise. The output from a Duffing system that has been triggered into stable dynamics may contain several coherent, usually harmonic, components. A binary decision detector operating only on amplitude may not always select all of these components. The development of a replica correlation processing stage is a key step presented in this thesis, on the route towards a practical detection system.

The desire to detect signals of unknown frequency requires a wideband detection system. Characterisation of the bandwidth and phase behaviour of the Duffing system was therefore a further component required, that supported the development later in the thesis (Sections 5.2.6 and 5.6) of an array of Duffing oscillators, each with a different internal drive frequency. The problem of unknown input phase was solved

by using four parallel Duffing systems, each with a different phase. The knowledge of the bandwidth, the addition of replica correlation detection and the four-phase solution, were combined into a single unit termed the Duffing Array Element (DAE). One of the final steps in the thesis was to implement an array of DAE's and characterise its behaviour using real and simulated input data.

In addition to the demonstration of the wideband DAE based system, a single DAE was used to confirm that it was possible to build a nonlinear detection system that would outperform Fourier transform based detection schemes at low false alarm rates, when the input single tone sine wave was heavily obscured by loud and highly impulsive biological noise.

1.3 Structure of the thesis

Chapter 2 establishes the state of the art from previously published literature, in topics central to nonlinear signal detection, as well as assessing some important supporting topics that will be referred to throughout the thesis. Nonlinear system models are discussed with emphasis on two particular systems, the Langevin equation and the Duffing nonlinear oscillator equation. Both systems form the basis for much of the investigation described throughout this thesis, and they will be referred to as the system 'models'.

The chapter also describes other topics, which are not necessarily state of the art, but are essential to the thesis. These essential methods and techniques will be used throughout the thesis as signal processing and data visualisation tools. Some of the tools described metrics that enable nonlinear system behaviours to be quantified, and detection performance to be measured. In many cases the chapter will include some explanation of how the methods operate, their relevance to the thesis and the benefit of using them.

The two nonlinear mechanisms are first introduced in Chapter 2, SR and a single step

transition between two distinct dynamic states of a nonlinear system. More specifically the second mechanism is almost exclusively confined to the transition from chaotic dynamics to a stable periodic limit cycle. However, a slightly different transition, from one lower energy stable state to the same limit cycle, is briefly considered in Chapter 3. Both mechanisms, SR and chaos-to-stable transition, were selected to form the core of the investigation in this thesis for two reasons. Firstly, both have a large extant body of relevant published research work, which provides a solid basis for this thesis to build on. Secondly, a comprehensive review of the potential of other types of nonlinear mechanisms was considered beyond the practical scope of the thesis reported here.

The first of the two nonlinear mechanisms is investigated in Chapter 3. SR is demonstrated using the Langevin system and the behaviours of SR relevant to improving detection performance, are explored and described in detail. The chapter opens by building on some of the techniques first introduced in Chapter 2, but adapting them where necessary to SR.

Chapter 4 follows a similar pattern to the SR chapter, but considers the Duffing transition. The transition is introduced, its properties explored and the basic detection performance measured for the ideal simulated data case (single sine wave in Gaussian white noise). The novel parameter space investigation is then used to select several configuration cases, the detection performance of each one is then measured and compared to the conventional linear (benchmark) detector.

Further properties of the Duffing system are characterised for their impact on performance, in Chapter 5. In this chapter, the DAE is developed and the final demonstrations of the system, either as a wideband sensor or a single sensor, are made using real data inputs.

1.4 Novel contributions

The novel contributions made in this thesis can be summarised as follows:

- The first known application of the mechanism of SR to the problem of underwater acoustic signal detection.
- The first known measurement of the detection performance by robust means, of a stochastic resonant system, for different input signal and noise types.
- A novel description of SR is proposed. SR has previously been described as a 'resonance' process that enhances the signal to noise ratio at the output, when the input S/N reaches a particular value. The SR condition is commonly achieved by adding more noise to a fixed (and relatively high) S/N input signal. The common description that SR is an enhancement to the output signal to noise ratio, can easily generate an erroneous belief that SR offers some additional discrimination between signal and noise. The findings presented in this thesis support a more accurate description of SR. SR is better described as a recovery from a catastrophic collapse in output signal to noise ratio, back to an S/N level that closely matches the expected S/N of an analogous linear system.
- The first known characterisation of a range of properties of the Duffing transition mechanism, with an assessment of their relevance and impact on detection performance.
- A novel approach to the review of various Duffing configurations that may have potential for improved detection, carried out by a characterisation of Duffing parameter space.
- The measurement of the detection performance of a chaos-to-stable nonlinear system, in the presence of different input signal and noise types.

- The development of a matched filter detection system specific to the Duffing transition pre-processor and based on replica correlation that uses a replica unique to the nonlinear system.
- The construction of a wideband time-frequency visualisation tool based on an array of nonlinear systems
- The application of the wideband time-frequency visualisation tool to real data in the form of a voice recording. This novel work significantly moves on from the only other known published example of a working array of nonlinear systems, by using real input data, by characterising its behaviour and by using the new detection scheme.
- Solid confirmation that the chaos-to-stable transition pre-processing mechanism is not immune to noise as much previous work had asserted.
- Confirmation of the detection performance of the chaos-to-stable mechanism when applied to signals comprised of highly impulsive real biological noise, mixed with simulated sine wave tone. The discovery of a new and potentially useful result that nonlinear pre-processing, with tailored replica correlation detection, outperforms convention linear detection for the impulsive noise case.

Chapter 2

Literature Review and Background

2.1 Introduction

Detection of underwater targets by separating their associated acoustic signals from unwanted acoustic background noise becomes increasingly hard as the level of the noise increases. Optimal detection theory for the ideal of Gaussian noise with an additive stationary sinusoidal signal is well established. This idealisation leads to detectors which may perform poorly in real world scenarios where the underlying assumptions are violated. The work reported in this thesis explores nonlinear detectors for use in such conditions.

The majority of this chapter develops a number of elements important to aid the understanding of the two nonlinear mechanisms in the context of signal detection. Elements of SR, nonlinear dynamics, signal detection theory and performance measurement, are described starting at a basic level. Methods of solving and presenting the output from, nonlinear systems are then introduced. There then follows a brief overview of some of the more complex properties and behaviours of nonlinear systems.

In the final sections of this chapter the state of the art in nonlinear mechanisms and behaviours, particularly SR and the transition, are reviewed to establish the background material which form the basis of this thesis. The chapters that follow will build on the material reviewed, to characterise the behaviours and properties of these mechanisms, most relevant to signal detection. Of most interest in this thesis are signals that are non-ideal because, for example the noise component does not have Gaussian distribution. The component to be detected is of most interest here, when it is very weak, in the sense of having a very small signal to noise ratio (S/N).

The breadth and maturity of our understanding as published in the literature and compared across the two mechanisms in the context of signal detection, is quite variable. Several identifiable steps have been made in advancing our understanding of SR over the last 30 years. Significant progress has been made in the mathematical description, cataloguing behaviours and finding conditions for existence. SR has been used to explain numerous observed behaviours in biology and earth sciences. However, application of SR to solve a wide range of engineering problems is very sparse in the literature. There has been a large body of literature looking at the transition mechanism in nonlinear oscillators for weak signal detection in the last fifteen years, but the scale of progress in terms of understanding and formal description, by comparison to SR is relatively small.

Linkage between SR and coupled synchronous nonlinear systems was investigated quite early [9]. Coupled nonlinear systems, such as the Duffing or Langevin systems, in general form a large and distinct body of research. Much of it relates to detection problems, either indirectly [10, 11, 12, 13, 14, 15] or directly as an application [9, 16, 17, 18, 19]. Coupled systems were reviewed in the early stages of the research for this thesis, however the topic was discarded as it was deemed beyond the scope. However, this domain is a strong candidate for future work.

Understanding the potential role of SR in weak signal detection has also been looked at [20, 21]. However to date no work has been published to establish how a weak

signal detection scheme, using the capabilities of SR, could be controlled for detection, or measurements made to establish how well it would perform as a pre-processor for a detector.

Sections 2.5 and 2.6 are primarily a literature review, and will focus on the most recent, relevant and significant advances made. The goal is to seek connections between the various areas that support the proposal that one or both, SR and the transition mechanism, nonlinear signal processing techniques can enhance detection performance compared to common linear detection methods.

2.2 Standard detection theory

Before introducing any topics related to nonlinear dynamics it is first necessary to establish what is meant by detection, and how detection performance is measured. Some theory relating to the type of signals to be detected, how they are detected and detection performance metrics, are introduced in this section. The section opens with some simple definitions.

2.2.1 Signal models

Throughout this document the stand-alone use of the term 'signal' refers to the total input to the system. The term 'signal' is also found used repeatedly throughout this thesis in the phrase 'signal-to-noise-ratio'. Its meaning in that context is distinctly different, and is defined below in Section 2.2.2. In the stand-alone usage case the term addresses any mixture of noise and periodic components, whether real or simulated. The nonlinear models used throughout this thesis are the 'system' referred to, and are defined later in Section 2.3.1. It is important to understand that the additive components of the input signal form an integral part of these system models, as distinct forcing terms. This is discussed further in Section 2.3.1.

The term 'signal of interest' (SoI) will be used to refer to that part of the signal that

is the component to be detected, $s(t) = A\cos(2\pi f_0 t + \phi)$. It is assumed that additive mixtures sufficiently model real data in the context of detection performance assessment. Consequently convolutive or multiplicative mixtures are not considered in the research reported here. All the simulated SoI's generated and used in this thesis are sine waves or sums of sine waves, the input 'signal' is therefore assumed to be modelled as shown in Equation (2.1).

$$y(t) = \sum_{i=0}^{\infty} A_i \cos(2\pi f_i t + \phi_i) + n(t) \tag{2.1}$$

Much of the literature on signal detection using the Duffing system refers to the Duffing system itself as the 'detector'. However, the nonlinear systems used here (and in the reviewed literature), only output a time-series of discrete samples that have dynamics representing a system state, that is dependent in a nonlinear way on the input signal it was given. The output time-series tells us nothing directly, about whether the SoI was present or not at the input. In other words a nonlinear system used in this way is not the detection decision maker. The terminology that will be used throughout this thesis, is to refer to all the nonlinear systems as pre-processing stages, or simply pre-processors. The detection decision stage is regarded as a separate signal processing step that follows the nonlinear pre-processor, to produce the SoI present/absent binary decision.

2.2.2 Signal to noise ratio

The terms 'signal' and 'SoI' were defined earlier in Section 2.2.1. Here a second, distinctly different use of the term 'signal' is defined as follows. Throughout this thesis, where ever the term 'signal' is used in the phrase 'signal to noise ratio', it is defined as meaning the SoI component only.

The S/N is a well established metric used extensively in the field of signal processing,

to indicate how strong a SoI is compared to the rest of the signal. A common way of using the S/N metric is to consider S/N gain, which is defined as the increase in output S/N relative to the input S/N. The S/N gain metric has been used for nonlinear systems [22, 23, 24, 25]. However, it can be extremely difficult to define a suitable method of measuring S/N on time-series data. The SoI can vary in amplitude over time, and the noise component may also exhibit rapid variation in colour, power and amplitude distribution. For example, the noise content in a signal might exhibit steeply sloping (colour) features in its spectrum, or large peaks not associated with the SoI but potentially close in frequency. That spectral profile may also vary significantly over time. In such an example it is far from clear which of the features should be included in the power estimate of noise. These complications are common features in underwater acoustic signals, and it will be shown later in the thesis, the spectrum of the output from a nonlinear system can also exhibit some of these features.

For these reasons S/N gain is not viewed as a suitable measure of the effectiveness of the preprocessor. S/N will be used, with care, particularly to aid in configuring some of the simulated signal input used in this thesis.

Recently, several researchers have applied S/N gain as a measure of the detection performance of nonlinear dynamical systems [4, 26, 27]. Signal to noise ratio at the output of a system has been viewed by some as a useful means of comparing different systems [7], however on its own it is not a comprehensive measure of detection performance.

The S/N as a variable, denoted snr, is most commonly defined as the ratio of average power in the sine wave signal component P_S to the average power in the noise component, P_N.

$$snr = \frac{P_S}{P_N} \tag{2.2}$$

A sine wave is commonly characterised using one of three amplitudes; zero to peak amplitude, A, peak-to-peak amplitude, A_p, or root-mean-square amplitude, A_{rms}. The power in the sinusoid P_S, is related to each, as shown in Equation (2.3). For all simulations in this thesis the simulated additive noise is generated with zero mean. The power in white Gaussian noise is therefore equal to its variance σ^2.

$$P_S = \frac{A^2}{2} = \frac{A_p^2}{8} = A_{rms}^2 \tag{2.3}$$

The S/N ratio for a sinusoidal signal in noise can be expressed as:

$$snr = \frac{P_S}{P_N} = \frac{A^2/2}{\sigma^2}$$

$$snr = \frac{A^2}{2\sigma^2} \tag{2.4}$$

$$SNR = 10\log_{10}\left(\frac{A^2}{2\sigma^2}\right) \tag{2.5}$$

Where SNR is the S/N expressed in decibels and σ^2 is the variance of the noise.

The true values of the signal amplitude and noise variance are usually unknown quantities in a real signal detection scheme. Therefore to estimate the S/N it is necessary to measure the average noise and average signal power. The definition of the *measured snr* variable used throughout this thesis is as follows:

$$snr = \left(\frac{S_p}{N_p}\right) \tag{2.6}$$

Where S_p is the signal power measured in a defined frequency band and N_p is the noise power in the same narrow band. This definition of *measured snr* depends on the bandwidth selected, so this bandwidth should be quoted along with the *snr* whenever it is used.

The estimation of S/N from the simulation data was based on measurements taken from the Power Spectral Density (PSD) of the Fourier transformed time-series data. The size of the Fourier transform was equal to the number of samples in the time-series data, typically this was > 8000 samples. Two copies of the PSD were retained, the second copy was then median filtered to smooth the spectrum in the signal frequency bin to the same level as the surrounding bins. The ratio of the first and smoothed second spectrum was then formed. The value in the frequency bin of the simulated sine wave was collected from the ratio power spectrum, which is an estimate of the required S/N. Finally the width of the frequency bin was calculated from the size of the Fourier transform, which is the noise bandwidth value required to make the S/N definition complete.

The S/N measurement procedure described above provides an estimate of the S/N. In all simulations the signal frequency was chosen to be centred in its discrete bin in the frequency domain, which reduced signal power measurement error caused by scalloping loss. Spectral leakage was reduced by leaving the data non-windowed, which is equivalent to applying a rectangular window function for a finite length of sampled data. Noise power estimation accuracy was improved by making a large number of iterations of the simulation and forming the arithmetic average of all power spectra.

All spectra were formed as one-sided, corrected and normalised PSD without additional windowing. The PSD smoothing filter was configured as a fixed sample length two-pass symmetric median filter. The filter length was selected by trial and error for each simulation case, based on a visual inspection of the output spectrum in and around the sine wave frequency bin. Typically the value most often used here is a length of 13 samples. The need to adjust the filter length was usually caused by the appearance of 'rise-up' artefacts in the smoothed PSD noise floor at the adjacent lower frequency bins.

The method of measuring the S/N is used extensively in Chapters 3 and 4,

occasionally in comparison with the expected (calculated values) where the noise and the signal are simulated.

2.2.3 Optimal detection

In this section some fundamentals of binary decision detectors based on a likelihood ratio criterion are reviewed. The background covered is necessary in order to place the detection scheme developed in Chapter 5 on a sound footing. There is no new work in this section as much of it is covered in text books on signal processing (see for example Chapter 13 [28] or Chapter 13-14 [29]). The starting assumption is that a signal has already been cast into a sequence of discrete time series samples, by the processing associated with the collecting sensor system.

It is assumed that one of only two possible hypothetical models will sufficiently accurately represent an unknown discrete time series data set x_m measured by the sensor. The first hypothesis H_1 models the signal as an additive combination of two components, the unwanted and the wanted component. In this context, 'wanted' refers to the signal to be detected (the SoI) s_m and 'unwanted' is all the remaining signal content, which will be referred to as noise n_m. The second hypothesis H_0 (the null hypothesis) models the signal as devoid of the wanted signal s_m, the two cases are conventionally written as shown in Equation (2.7).

$$\left.\begin{aligned} H_1 : x_m &= s_m + n_m \\ H_0 : x_m &= n_m \end{aligned}\right\} \tag{2.7}$$

The goal is to find an expression that can be used to maximise the probability that the wanted component s_m is present given the value of the current sample x_m measured on the sensor, whilst minimising the probability of the alternative hypothesis given the same sample value. The goal can be represented as an inequality of the two probability distributions, both conditional on the current value of x_m.

$$P\left(H_1|x_m\right) > P\left(H_0|x_m\right)$$

Note that each hypothesis has an associated probability distribution function, the two pdf's are assumed to be different as a result of the two different signal models of Equation (2.7). The pdf's are labelled here as $p\left(x_m|H_1\right)$ and $p\left(x_m|H_0\right)$, the reason for their introduction will become apparent in the following steps. The most probable of the two hypotheses is automatically selected for by forming the ratio of the probabilities associated with each hypothesis. If the ratio is greater than 1 the hypothesis represented in the numerator of Equation (2.8) is selected.

$$\frac{P\left(H_1|x_m\right)}{P\left(H_0|x_m\right)} > 1 \tag{2.8}$$

The next step is to recast the ratio of conditional probabilities in Equation (2.8) as a ratio of the two corresponding conditional probability distribution functions. This is necessary since in effect Equation (2.8) is a mixture of discrete and continuous random variables, H and x respectively. The approach seeks to find the total probability of error that the wrong hypothesis is selected, then to minimise the error. The procedure (see for example page 225 Schwartz and Shaw [30]) starts by finding integral expressions for the two types of error, over each of the two regions on X. The probability of false detection P_{FD} corresponds to selecting hypothesis H_1 when no wanted signal component is present, and the probability of false rejection P_{FR} corresponds to selecting H_0 when a wanted signal is present. The two error probabilities are made mutually exclusive by fixing a threshold value of $x_m = d$ so that all X is divided into two regions, commonly labeled X_1 for the signal present hypothesis H_1, and X_0 for H_0. Next, using the fact that the probabilities of the two

hypotheses are also mutually exclusive allows the use of the total probability theorem to find the total probability of error P_e. The expression for P_e is therefore as follows:-

$$\begin{aligned} P_e &= P_{FR} + P_{FD} \\ &= P(H_1) P(X < d|H_1) + P(H_0) P(X > d|H_0) \end{aligned} \tag{2.9}$$

$$P_e = P(H_1) \int_{-\infty}^{d} p(x_m|H_1)\, dx + P(H_0) \int_{d}^{\infty} p(x_m|H_0)\, dx \tag{2.10}$$

The need for the pdf's is now clear. It is necessary to integrate over a continous region of X bounded on one side by d in order to calculate the probability $P(X < d|H_1)$ (and similarly $P(X > d|H_0)$).

Note that the two integral regions cover all X and are mutually exclusive, as are the probabilities of the two hypotheses. Using these properties as well as simplifying the conditional pdf's to $p(x_m|H_1) = p_1(x_m)$ and $p_0(x_m)$ conditioned on the null hypothesis probability, leads to the following:-

$$P_e = P(H_1) + \int_{d}^{\infty} \left[(1 - P(H_1)) p_0(x_m) - P(H_1) p_1(x_m) \right] dx \tag{2.11}$$

The value $P(H_1)$ is fixed, so to minimise the total probability of error P_e it is necessary to minimise the value of the integral. However, the probabilities and pdfs in Equation (2.11) all non-negative by definition.

The final step in the procedure derives the expression for the likelihood ratio, which is the key relation used in the design of an optimal or maximal detector. Unfortunately the step itself contains an important inherent assumption not usually brought out in text books on the subject. The step proceeds as follows. It is assumed that the

majority of the area under the pdf curve $p_1(x_m)$ falls on one side of the single threshold $x_m = d$, and that the majority of the area under $p_0(x)$ falls on *the other side* of $x_m = d$. The situation is further constraining because the relative positions of the two pdf's are assumed fixed such that the mean of $p_1(x_m)$ is ordered *higher* than that of $p_0(x_m)$. The step at Equation (2.9) enshrines this ordering constraint by the choice of the direction of the inequalities. Clearly these assumptions are valid for the case that both pdf's are unimodal (for example Gaussian). P_e can be minimised by making the term $P(H_1)\,p_0(x_m)$ large so that the integral is as small as possible. The following inequality ensures minimum error in selecting the hypothesis, it is controlled by setting an optimal value for d.

$$P(H_1)\,p_1(x_m) > (1 - P(H_1))\,p_0(x_m)$$

The likelihood ratio is therefore

$$\mathcal{L}_{\Re}(x_m) \triangleq \frac{p_1(x_m)}{p_0(x_m)} > \frac{1 - P(H_1)}{P(H_1)} \tag{2.12}$$

The analysis described above is usually presented alongside examples of amplitude probability distributions for p_0 and p_1, that both have a single peak (unimodal). That is not to say the analysis is necessarily invalid for multimodal distributions, just that care needs to be taken in understanding the change in the distributions with and without signal present. More specifically, it is most desirable that the data output from the nonlinear system can be further processed to ensure there is a *single* boundary between the two probability inequality regions $P(H_1) < P(H_0)$ and $P(H_1) > P(H_0)$. In this way a single detection threshold is sufficient, and the two-integral relation of Equation (2.10) that encapsulates a single threshold, and the likelihood function of Equation (2.12), are then sure to be valid.

The option to measure more than one data sample x_m from the sensor will nearly always be the case in a practical detection system. Solving the likelihood ratio of

Equation (2.12) uses the probability distribution function for several samples, in both hypotheses. Averaging several samples has the effect of reducing the variance about the mean, for unimodal pdf's such as a Gaussian pdf. Assuming the two pdf's are already separated along x_m to some degree, the discrimination between the two hypotheses improves because the total error P_e reduces. Clearly, averaging in this way is desirable because the result is better detection performance in a binary decision detector.

Unfortunately, the amplitude distributions output from a nonlinear system are not necessarily unimodal, and the relative positions of the multiple peaks for both hypotheses, may not be optimal for an improvement in distribution separation, by averaging the data. A method of ensuring a unimodal distribution at the output of a nonlinear system, using correlation detection (and correlation coefficient distribution) rather than frequency binning and amplitude distributions, is described in Chapter 5.

The key points to note from this section in relation to the rest of the chapters is as follows. The output probability distribution functions may not necessarily be unimodal or ordered on the positive X parameter, such that the signal-present pdf has predominantly larger values of x_m. It may also generate x_m smaller than the noise only pdf.

Basic optimal detection theory was presented in this section. The question of how to measure the detection performance of a practical system, is introduced in the next section, and the performance metric described will be used extensively in this thesis. The measured results will be frequently presented as a pairwise comparison of two measures. One measure will be made on the nonlinear system in question, and the second will be made on a benchmark 'conventional' detector scheme. The benchmark scheme will be a simple threshold on amplitude (or power), of the Fourier transform of the signal. It is important to emphasise that the goal here is not to demonstrate how nonlinear systems can outperform 'conventional' FFT and threshold detection on a single sine wave in Gaussian white noise, but to indicate the offset from a constant

benchmark. In that way, comparison of the performance of different and disparate nonlinear schemes can be compared via the benchmark proxy.

2.2.4 Performance assessment

Receiver Operating Characteristics analysis (ROC analysis) provides a statistical method of measuring the performance of a receiver or detector. Some important attributes of the method make it attractive. It can be applied to any detector, which makes it a common metric so that the performance of quite different detectors can be quantitatively compared. The same technique can be applied at any point in the signal/data/information processing chain so the performance of the system up to that point can be assessed. ROC analysis quantifies the performance of a binary decision detector, which requires a single threshold applied to the amplitude at the frequency (signal) of interest. The decision then is made as 'signal present' for amplitudes higher than the threshold, and absent for amplitudes lower. However, in the presence of noise it is possible that the wanted component may in fact be absent but the noise momentarily generates an amplitude higher than the threshold, leading to a false positive. Conversely the desired component may be present but generates an amplitude too low for a detection to occur. This is a false negative. Both of these situations are false outcomes. For a binary decision detector then, there are four possible outcomes (two true and two false) created by permuting signal present or absent with amplitude higher or lower than the threshold.

ROC analysis can be conducted at any suitable point in a signal processing chain where a decision between outcomes (signal present or absent) can be made. Notice in this case there are two detection choices regarding the SoI. This situation is normally referred to as a two-class ROC analysis and will be the basis for all ROC analysis in this thesis [31]. It is possible to perform ROC analysis using three or more classes [32, 33].

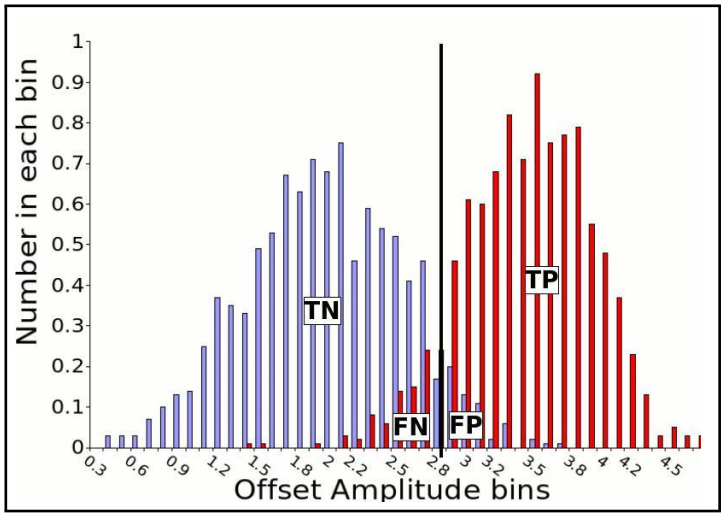

Figure 2.1: Stylised probability distribution functions. The four outcomes in a binary decision detector, testing for the presence or absence of the wanted component in an input signal. False positive (FP), false negative (FN), true positive (TP) and true negative (TN). Integrating over each region in each of the two PDF's calculates the probability value for each outcome.

The ROC analyses carried out in this thesis were usually made in the frequency domain, based on the bin corresponding to the frequency of the SoI. However, some of the ROC analyses in Chapter 5 were made at the output of the correlator, which is described in Section 5.2.4. In both cases the data were collected from multiple *pairs* of simulation runs. The first run generates the simulated noise and collects the signal bin amplitude with signal absent. The second run keeps the same noise used in the first run, adds a simulated signal, and collects one sample of the amplitude statistic in the signal frequency bin, with signal present. The pair of runs constitutes one iteration.

Pre-defining the frequency bin in this way clearly is not representative of real detection system because the frequency of a SoI will generally be unknown. False positives can be declared not only within the correct frequency bin, but also in all other frequency bins where the spectrum level is highest on a given occasion. The fixed-bin approach removes variation in detection performance resulting from this second type of false positive. The result is a falsely high ROC curve (detection performance) that is better for comparing different detection schemes because it removes a source of variation not relevant to the comparison.

The ROC analysis method is illustrated in the following example. A simple input signal to a basic detection scheme, was simulated by adding a single sine wave to white Gaussian noise. The average power of each of the two parts of the input signal were chosen so that the input SNR was -31dB, calculated using Equation (2.5). The simulated input signal was created using simulated Gaussian noise with a standard deviation of $\sigma = 1.4061$ (variance $\sigma^2 = 1.977$), and a sine wave peak amplitude of $A = 0.05604$. 1300 iteration pairs were generated, with the sine wave present and then absent, with the independent but identically distributed Gaussian noise regenerated for each iteration pair. The amplitude value in the pre-determined frequency bin, was collected for each of the pairs in an iteration.

The amplitude values collected from a sufficient number of iteration pairs are sorted into one of the four outcomes, forming what is sometimes referred to as a confusion matrix (see, for example, Figure 1 of [31]). The ROC algorithm sorts the amplitude counts into the two distributions illustrated in Figure 2.1, and proceeds to step a detection threshold across the two distributed amplitude (counts) data sets. At each step the four confusion matrix values are calculated by summing the counts within each of the four areas illustrated in Figure 2.1, (TP, FP, TN, FN). Using this information the True Positive Rate (TPR) and the False Positive Rate (FPR) are calculated using Equations (2.13) and (2.14) [31].

$$TPR = \left(\frac{TP}{TP + FN} \right) \tag{2.13}$$

$$FPR = \left(\frac{FP}{FP + TN} \right) \tag{2.14}$$

The set of paired values of TPR and FPR calculated for each threshold step, are then plotted. For the example described here the resulting plot is shown in Figure 2.2. The ROC curve for the simulated input signal configured with $SNR = -31dB$ is

shown, rising from the $(0, 0)$ coordinate to the $(1, 1)$ coordinate. ROC curves generated from a two-class analysis, will always start and finish at these points.

The second ROC curve shown in Figure 2.2, was generated with a calculated input SNR of $-34dB$, by changing the sine wave amplitude to 0.0397. The effect of reducing the input S/N on the position of the ROC curve is clear, the curve moves position down and to the left. Removing the sine wave component altogether from the input signal, leaving just the noise, would cause the ROC curve to shift further downwards, to become a straight line rising from bottom left to the top right corner on the ROC plot. This line represents the equal probability outcomes, a detector exhibiting this type of ROC curve has a detection performance no better than the toss of a fair coin. The generic terms TPR and FPR are used throughout this thesis. However, it is noted that the terms Probability of Detection and Probability of False Alarm, are commonly encountered where ROC analysis is applied to underwater acoustics and sonar performance.

Movement of ROC curve in the other direction, towards the top left is interpreted as improved performance of the binary decision system. The amount of improvement can be quantified, and represented by a single number, the Area Under Curve (AUC). Improved system performance is indicated by increased AUC. All the work described in this thesis uses the AUC metric [31]. Specifically, the AUC value is calculated as the area between the equal-probability line and the curve itself. The maximum value the AUC can take is therefore 0.5 [31]. An area integration function built into the modelling environment used for all simulations, was used to find all AUC values in the work reported here.

The frequency domain detectors used in this thesis, are all based on a single Fourier transform with no averaging, overlap or windowing. Unless otherwise stated, the SoI is chosen so that the frequency coincides with the centre of a frequency bin. Using no windowing on the finite length data is the same as applying a rectangular window

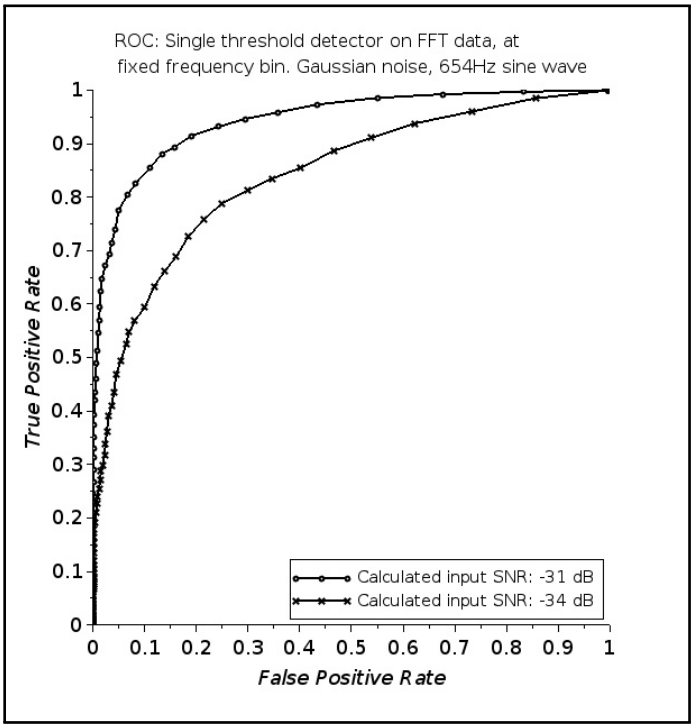

Figure 2.2: Example ROC curves at two calculated input SNR values, as indicated by the in-plot legend. $AUC = 0.3419$ for input $SNR = -34$dB, and $AUC = 0.4448$ for the input $SNR = -31$dB. Set up parameter values were as discussed in the text.

over the entire data length. There is therefore no leakage of energy into other frequency bins.

ROC analysis requires a large number of iterations in order that the ROC curves are estimated accurately. The more iterations each analysis uses, the longer it takes to generate the ROC curve. All the ROC curves in this thesis are therefore a trade off between tolerable simulation run time and reasonable stability. A smooth ROC curve is a good indication of stability in the result. Typically between 400 and 2000 iterations were used to generate all the ROC curves in this thesis, the model typically taking between twenty minutes and three hours to run on a basic specification laptop computer (CPU 2GHz, Memory 8GB).

Much of the available performance analyses of non-linear system based detectors carried out by previous researchers falls short for one or more of the following reasons. The performance measure chosen does not enable a fair comparison of disparate

detection schemes. The measure was applied to a specific configuration of the nonlinear system. An example of the first of these is provided by a performance analysis of a stochastic resonant based detector [34], where the probability of error and the probability of detection (P_e and P_d respectively) were measured. The problem is that they were considered as two separate performance measures, the final step of combining them to generate a full ROC analysis was not carried out. The more complete ROC analysis measure was however, applied to an array of stochastic resonance based detectors, (termed suprathreshold SR) [35]. The work was in effect an attempt to improve the sensitivity to the SR mechanism to very weak signals by averaging across an array of SR detectors. In this case unfortunately, ROC analysis was not applied to a single SR detector. To date the only known work quantifying performance of the Duffing transition mechanism uses only the probability of detection. False alarm rate was considered but a rather extraordinary claim that *'no false alarms occurred in our experiments'* was made [8]. In summary, only a small number of limited scope analyses quantifying the detection performance of various SR based systems exist, and no substantive ROC analyses of the Duffing (or any other nonlinear system) transition mechanism have been found to date.

ROC analysis was also carried out on a rather unusual application of chaotic systems [36]. The malleability of nonlinear models such as the Lorenz system was employed to generate tailored time series used as input to secondary nonlinear systems in order to improve the performance of the second system being used to detect faults [36].

2.3 Nonlinear systems introduced

The nonlinear system models used throughout this thesis, will now be described. They are introduced at this point, prior to covering the state of the art on the use of the two nonlinear mechanisms found in nonlinear systems, that form the focus of this thesis.

2.3.1 System models

Two nonlinear system models are considered in this thesis. The Langevin system is used predominantly in the investigation of SR, and the Duffing system is used to investigate the chaos-to-stable transition mechanism. Both system models are introduced and defined in this section.

The Duffing oscillator implemented in the model is a periodically forced, damped, spring system with a restoring force term composed of additive linear and nonlinear components. The version implemented was selected as the most commonly used, and is based on the system first introduced and extensively studied by G. Duffing in 1918 ([37] page 2. Duffing's original publication is in German [38], sections translated into English [39]). Two additional forcing terms are modelled representing the input perturbation noise and the SoI. The periodic components of the input are modelled as always additive to each other and to the noise components, where simulated input data are used. The system is shown in Equation (2.15), where the three terms on the right hand side are the three separate force terms.

$$\begin{aligned} \ddot{x} + \delta\dot{x} - \alpha x + \beta x^3 &= \gamma\cos(\omega_0 t + \phi_0) + F(t) \\ \ddot{x} + \delta\dot{x} - \alpha x + \beta x^3 &= \gamma\cos(\omega_0 t + \phi_0) + A\cos(\omega t + \phi_i) + n(t) \end{aligned} \tag{2.15}$$

where:-

$\gamma\cos(\omega_0 t + \phi_0)$ = Configurable periodic force term, internal to the system

and:-

$$\left.\begin{aligned} F(t) &= A\cos(\omega t + \phi_i) + n(t) \\ A\cos(\omega t + \phi_i) &= \text{SoI} \\ n(t) &= \text{Contaminating noise} \end{aligned}\right\} \tag{2.16}$$

The Duffing model represented by Equation (2.15) is a forced (inhomogeneous), damped, second order, nonlinear system.

The original formulation of the Langevin equation is a second order system and lacks the restoring force terms seen in the Duffing model. Its original form is shown in Equation (2.17).

$$\frac{d^2x}{dt^2} = -\gamma\frac{dx}{dt} + n\left(t\right) \tag{2.17}$$

However, in the domain of nonlinear signal processing and time-series analysis a version closer in form to the Duffing system is almost always used [40, 41, 42, 43]. This commonly used version is shown in Equation (2.18), and it is this form that is considered in this thesis.

Equation (2.18) can be configured to exhibit certain behaviours seen in the Duffing system. It is a bistable system with two stable points symmetric about $x = 0$. Three additive forcing terms are included on the right hand side of the Langevin equation, one periodic and two noise terms, the two force terms are designated as a model of the input signal $x_s\left(t\right) = s\left(t\right) + n\left(t\right)$ where $s\left(t\right) = A\cos\left(\omega t + \phi_i\right)$. The noise term $n\left(t\right)$ will be used as the main system control during the simulations, in the sense that the variance and distribution of the added noise $n\left(t\right)$ can be varied in order to initiate the stochastic resonance behaviour. Stochastic resonance will be introduced in Chapter 3. The meaning of the third force term $\xi\left(t\right)$ is described later in this section.

$$\delta\dot{x} - \alpha x + \beta x^3 = A\cos\left(\omega t + \phi_i\right) + \xi\left(t\right) + n\left(t\right) \tag{2.18}$$

The Langevin system in this form, is first order but Duffing is a second order system. The difference has implications impacting the use of phase space as a tool to visualise the behaviour of first order systems.

The Langevin system is the model most commonly used to demonstrate and

investigate SR, see for example [41, 44, 45, 46, 43]. In publications investigating SR that use the Langevin system, the equation is almost invariably defined in its first order Brownian motion (stochastic equation) form as shown in Equation (2.19).

$$\delta\frac{dx}{dt} - \alpha x + \beta x^3 = A\cos\left(2\pi ft + \phi_i\right) + \sqrt{2D}\xi\left(t\right) \tag{2.19}$$

The symbols used reflect the origins of the equation, in modelling the diffusion of gas molecules or other particles through a medium. It is more useful to re-state the model using more conventional signal processing symbols, by changing the stochastic diffusion term $\sqrt{2D}\xi\left(t\right)$. In Brownian motion the real physical quantity known as the one dimensional particle diffusivity is conventionally defined as

$$D = \frac{1}{2}\frac{d\langle\left(x_0 - x_n\right)^2\rangle}{dt}$$

where $\langle\left(x_0 - x_n\right)^2\rangle$ is the Mean Squared Distance (MSD), between an arbitrary datum point x_0 and the evolving discrete distance from the datum, of the position of a particle at discrete times x_n. Integration for a large number of particles over time leads to $\langle\left(x_0 - x_n\right)^2\rangle = 2Dt$. Considering x not as particle position but amplitude of a zero mean constant power random time series then MSD is simply the variance σ^2, and it is a fixed value at any time (including $t = 1$). Therefore the diffusion becomes $\sqrt{2D}\xi\left(t\right) = \sigma\xi\left(t\right)$, and this will be represented even more succinctly as the input signal noise $n\left(t\right)$.

The term δ in Equation (2.18) is always set to a value of 1 for the simulations used and results reported in this thesis, except in a small number of cases where indicated. This is in accordance with the Langevin configuration used by the majority of other researchers (for example [41, 44, 45, 46, 43]). With these changes the Langevin system is re-cast as Equation (2.20).

Most publications (including this thesis) introduce SR by describing how the resonant effect is initiated by adding a controlled amount of extra noise to the input. The

direct implication is that a third forcing term should be present in the model, that acts as the SR optimising control. This explains the presence of the third noise term $\xi(t)$ shown in Equation (2.18). The basis of such a model having three force terms is further supported because the nature of the real data input in underwater weak signal detection will generally be unknown and not controllable. So the simplest means of control and optimisation is via the third forcing noise term. In an implementation of SR pre-processing, with a later detection stage targeting real world signals, the Langevin pre-processor would therefore be more accurately modelled using three forcing terms; two unknown input terms and the third noise control term. However, the SR work described in this thesis, Chapter 3, concentrates on simulated data and not real data. Consequently it is sufficient to use a Langevin model that comprises only two force terms, both are modelled as the input signal so no third force term $\xi(t)$ is necessary. Therefore the two roles, of controlling the input noise, and simulating an 'unknown' input noise of a real signal, are represented by one noise force $n(t)$. The version of the Langevin system implemented and considered in the investigations in this thesis is therefore represented by Equation 2.20.

$$\dot{x} - \alpha x + \beta x^3 = A\cos(2\pi f t + \phi) + n(t) \tag{2.20}$$

2.3.2 Numerical solution

There are no analytic solutions to the non-linear system models used in this thesis. Developing fully accurate, robust, global analytic methods to solve these stochastic nonlinear systems is not a realistic expectation. However, locally accurate analytic solution methods do exist. Many of these are based on the local linearisation of the system in the region where a local solution is sufficient. Numerical methods provide the global solution needed, consequently these methods are used throughout this work.

A large number of methods of solving nonlinear systems numerically exist. They have been developed over a number of decades fulfilling a range of aims, targeting one or more of; speed, accuracy, accuracy specifically in the fast sections of the dynamic system solution, specific difficult applications or algorithm simplicity.

The primary numerical method used here is a fourth order Runge-Kutta four stage (RK4), fixed step method. Variable step methods are available but the Runge-Kutta method was selected for its ease of implementation. It was necessary to implement a version of RK4 where the input signal samples could be correctly integrated into the appropriate place in the four stage calculation. The RK4 numerical solver algorithm adopted for this thesis is derived in Appendix A. The derivation in the appendix uses the Duffing system reduced to two coupled first order systems, as the example nonlinear system. The bespoke method pays particular attention to the correct inclusion of the data samples at each RK4 stage, that represent the input signal.

2.3.3 System rescaling

It is often convenient to normalise the variables and parameters of a nonlinear system to make it simpler to configure. This is because there are fewer control parameters, but the system behaviours are left unchanged. Two different normalisation regimes are used in this thesis. The first is used in the SR investigations of Chapter 3, the second is used in the transition investigations in Chapter 4 and to a lesser extent in Chapter 5. The three main reasons for normalisation are as follows. First, normalisation to a particular regime used previously, maintains consistency with that previous research, which enables comparison and cross-validation of results. Second, for a non-normalised system more system parameters need to be changed in order to configure the system into a given state. The third reason is the likelihood of divergence in the numerical solution can be reduced by selecting a suitable normalisation scheme.

The two normalisation methods mentioned earlier, are introduced as follows. First, a

full re-scaling of the Langevin system to render it dimensionless, is used extensively in the SR investigation. Second, the method chosen for the the Duffing system (for the work in Chapter 4) is a more restricted frequency normalisation approach, rather than a full dimensionless Langevin re-scaling [4]. The derivation is reproduced in a slightly expanded form in Appendix A. The re-scaling method for the Langevin system is described in detail in the remainder of this section.

The normalised (dimensionless) Langevin system used in the SR study follows the scheme proposed by previous workers [47]. The derivation of the re-scaling factors starts by temporarily re-introducing the factor δ into the Langevin Equation, as shown in Equation (2.21). Recall that although the implemented models used in this thesis set $\delta = 1$ in all SR simulations, its inclusion provides clarity in the dimensional analysis that generates the two factors required to re-scale the time and frequency variables.

The Langevin system derived from considerations of Brownian motion, is usually described as a balance of forces. As such it is a model for a mechanical system where the variables represent real world quantities that have specific units. From this point of view, all the additive terms in the Langevin system (Equation (2.18) and repeated below) can be considered as force terms that have dimension $\frac{ML}{T^2}$, (here the capitalised letters stand for mass, length and time respectively). Dimensional analysis is used to find the dimensions of the two variables (x and t) and all the parameters (δ, α, β, A). Square brackets are used in the analyses to denote 'dimension of', for example $[x]$ means 'dimension of x'. A suitable combination of the three parameters δ, α and β is then found such that the resulting re-scaling factor has a dimension that is the inverse of force. The separate force terms are then re-scaled using this factor to make them dimensionless. It is also necessary to find one additional parameter combination to re-scale the time variable to a dimensionless form. Finding the dimension of δ is chosen as an example of the process, which proceeds as follows:

$$\delta\dot{x} - \alpha x + \beta x^3 = A\cos(\omega t + \phi) + n(t) \tag{2.21}$$

$$[\delta][\dot{x}] = \frac{M}{T}\frac{L}{T} = \frac{ML}{T^2}$$

$$[\delta] = \frac{M}{T}$$

The dimensions of the remaining quantities are found in a similar way and all are stated as follows: $[\delta] = \frac{M}{T}$, $[\alpha] = \frac{M}{T^2}$, $[\beta] = \frac{M}{L^2T^2}$, $[t] = T$.

At least one combination of parameters forms a re-scaling factor having a dimension that is the inverse of force. It is possible to use the full and formal dimensional analysis approach to derive the required factor however, in this case it was just as quick to find it by inspection because of the limited set of possible combinations. The force re-scaling factor was found as follows:

$$\left[\sqrt{\left(\frac{\beta}{\alpha^3}\right)}\right] = \sqrt{\frac{M}{L^2T^2}\frac{T^6}{M^3}}$$

$$= \frac{T^2}{ML}$$

The remaining re-scaling factors are found in a similar way. The full form of the factors for time and frequency require the damping parameter δ. However the Langevin system used in this chapter does not include the damping term. The impact on the re-scaling factors is to remove the damping term by setting $\delta = 1$. The two re-scaling factors can now be stated as; for force terms $\sqrt{\beta/\alpha^3}$, and for the time variable α/δ.

Re-scaling all additive force terms and the time variable produces a new set of dimensionless terms (denoted by the subscript $*$), in the following way:

$$
\begin{aligned}
\dot{x}_* = \quad \sqrt{(\beta/\alpha^3)}\ \delta\dot{x} \quad &= \quad \sqrt{(\beta/\alpha^3)}\ \dot{x} \\
x_* \ = \quad \sqrt{(\beta/\alpha^3)}\ \alpha x \quad &= \quad \sqrt{(\beta/\alpha)}\ x \\
{x^3}_* \ = \quad \sqrt{(\beta/\alpha^3)}\ \beta x^3 \quad &= \quad \sqrt{(\beta^3/\alpha^3)}\ x^3 \\
A_* \qquad\qquad\qquad\quad &= \quad \sqrt{(\beta/\alpha^3)}\ A \\
t_* \ = \quad (\alpha/\delta)\ t \quad &= \quad \alpha t \\
n_*(t) \qquad\qquad\qquad\quad &= \quad \sqrt{(\beta/\alpha^3)}\ n(t)
\end{aligned}
$$

The normalised Langevin system can be re-written with the $*$ subscript dropped, provided it is understood all terms except the driving frequency parameter f are now re-scaled and dimensionless. The natural frequency of the linear homogeneous part of the system is now fixed at a dimensionless value of $\delta/\alpha = 1/1 = 1$.

$$
\dot{x} - x + x^3 = A\cos(2\pi f t + \phi) + n(t) \tag{2.22}
$$

The form of the two systems, Equation (2.18) and the normalised version, Equation (2.22) above, is the same apart from the two factors α and β. This allows a single coded implementation of the Langevin system to be constructed, that can be used (with care) as either a non-normalised or a normalised system. Setting $\alpha = \beta = 1$ in the coded implementation of the non-normalised system of Equation (2.18) is equivalent to normalising the system, because all the scaling factors use one or both of α and β. This convenience is valid provided it is understood all output (x displacement) and control quantities (amplitude A, noise $n(t)$ and t time) are re-scaled and dimensionless.

The result is a normalised Langevin equation that retains all the SR related behaviours associated with a bistable system with two stable energy minima located at $\sqrt{|\alpha|/|\beta|}$, but with fewer control parameters. All modelling and simulation carried out in Chapter 3 using a Langevin system was therefore based on a single encoded implementation of Equation (2.22).

2.3.4 Phase space

Phase space is an abstract but concise way of visualising all the possible states of a system. The space is defined by the minimum number of degrees of freedom in the system and each point in the space represents one system state.

In dynamical systems the system state changes over time from one point in phase space to the next usually with a smooth transition. A continuous trajectory is traced out in phase space by the changing system state. Phase space plotted with trajectories is known as a phase portrait.

For conservative dynamical systems phase portraits are often simple closed loops or even one or more non-moving points (stable states). The phase portraits for dissipative systems such as those studied in this thesis tend to show a variety of additional and more complicated structures that reveal a great deal about the distinct dynamic and stationary states the system can occupy. The number of dimensions of the phase space of a system is the minimum number of degrees of freedom required to fully define all possible system states. Clearly graphical representation of phase space is difficult for systems with more than three dimensions.

It is still possible to extract information from higher dimension portraits by taking appropriate two dimensional sections through the phase portrait. This technique was initially developed by Henri Poincaré and the simple fixed position planar approach is known as a Poincaré section.

Another 'dimension reduction' technique is known as a Recurrence plot. In this case the two dimensional plane is not a fixed section through the original phase portrait but an abstract manifold where the trajectory crossings are equidistant in time not space. Recurrence plots are most useful when the manifold is approximately transverse in phase space, to the major trajectory flow pattern. Such plots can reveal complex cyclic behaviours in the trajectories themselves. Poincaré sections therefore

can be considered as a specific type of the more general recurrence plot technique.

Phase space plots generally require the originating system to have two or more dimensions, to generate the corresponding plots of two or more dimensions. An estimate of a two dimensional phase space can be made from the single one-dimensional time-series solution of a one dimensional system such as the Langevin system of Equation (2.18).

Phase portraits are such a fundamental and useful tool revealing many of the behaviours of a dynamical system that they are used extensively throughout this thesis.

2.3.5 Lyapunov exponents

Lyapunov exponent techniques are widely used as an indicator that a dynamical system is in a state of chaos. It achieves this by calculating an estimate of the rate of divergence of two proximal trajectories in the phase space of a system. There are two approaches available for calculating Lyapunov exponents depending on whether the system equations are known [48] or alternatively for when only a system time series output is available [49, 50, 51]. Both techniques are powerful tools to characterise phase space and parameter space for nonlinear dynamical systems [52]. However estimating Lyapunov exponents from a time-series can be a difficult and imprecise task [53] and ([54] page 70).

The time series based technique calculates the logarithm of the ratio of the distance between a base trajectory and another nearest adjacent trajectory in phase space, before and after one discrete time step. The process then finds a new trajectory nearest the base and repeats the ratio calculation, stepping along the base at each iteration. After sufficient repeats the average exponent is found. This procedure is well described [53] and finds the maximal exponent value rather than the spectrum, from a time series of data.

A positive maximal exponent is taken as an indication of the system being in a chaotic state. However, non-chaotic but very noisy time series data can also produce positive exponent values. Maximal exponent values derived from a time series therefore may not be a sufficient indicator of chaos. More robust confirmation of chaos can be made if the technique is used in conjunction with others such as calculations of data dimension. A non-integer dimension value can indicate the presence of a strange (chaotic) attractor (see Section 2.3.6 for more detail).

One area of recent active research has investigated Lyapunov vectors [55, 56] to explore more robust characterisation of predictability and stability in chaotic systems. It is considered desirable to have a more precise method of assessing the stability of a nonlinear detection system as one contribution towards improving its performance as a detector.

2.3.6 Some essential features of dynamic systems

Features and behaviours relevant to the dynamical systems investigated in this thesis are introduced and briefly described in this section. Most of the structures described here can be revealed by constructing the system phase portrait, recurrence plots or Poincaré sections described previously. Using these visualisation tools these features present as clearly identifiable patterns or structures which are repeatable but not necessarily permanent over time. Several of the structures can be found in linear systems as well as nonlinear ones.

The state of a dynamical system, or system state, has two distinct but specific meanings in the context of this research. The first is the more widely understood meaning particularly in relation to phase space and is best described by illustration. The phase portrait of a two dimensional system whose dimensions are represented by displacement and velocity, is a two dimensional plot of velocity versus displacement. Any point in this space has these two variables that uniquely identify it. Any pair of values for those two variables represents a unique system state for that particular

system. This meaning of the term 'system state' will be distinguished in the rest of this thesis (where necessary) as that associated with there being a state vector of unique variable values.

The second meaning of 'system state' used in this thesis refers to a region or manifold having common gross system behaviours. This meaning will be described in more detail at the end of this section. First it is necessary to describe structures found in the visualisations of dynamical systems.

The path marked out in phase space from one point to the next by the continuous change with time, of the variables representing the system state (the state vector) is termed a trajectory. A dynamical system can have two or more dimensions and, in general, the system state trajectories have the same dimension, clearly identifiable in the system phase portrait. For example, the Lorentz system is three dimensional and its full phase space is also three dimensional.

The notion of 'trajectory' or 'path' implies that the evolving state vector always changes to some nearby neighbouring state, and does so in some orderly or perhaps deterministic way. State vector evolution does not always move from one previous state to a single following state. Under certain conditions a system can bifurcate to two states existing simultaneously at one time point. It does not necessarily mean the system exists at both states simultaneously rather that it can jump apparently randomly to one or the other.

It is usual to describe the fixed points of a simple linear dynamical system, but the more general name used for a special class of the analogous features found in nonlinear systems is the term attractor. The properties of attractors are that they can be stable or unstable, moving or stationary, closed or open, transient or permanent, and one, two or more dimensional. They can be a closed manifold that bounds finite regions of phase space or be the simplest of singular fixed points. The name attractor is a little misleading in that if it is an unstable feature all nearby

trajectories may in fact diverge away from it rather than converge towards, or be attracted to it. In both cases the name attractor is most commonly used although the term repellor can be encountered.

The common feature for all attractors is that when a system evolves towards (or away from) it the gross behaviour of the system will change. For example a single fixed point in phase space may be a permanent stable point for the given system. A system state trajectory close enough will often move with one characteristic behaviour towards the fixed point where it will terminate. In this case the gross system behaviour alters from one of changing state to unchanging state.

If the attractor is not a point, but a stable, closed state trajectory, then any trajectory starting close enough may move towards it, where it becomes entrained onto that attractor. In this case the system state is still changing but it remains on this attractor trajectory for all time unless acted on by a new force that causes the fundamental system to alter. This type of closed attractor is given the name limit cycle to indicate the resulting system state periodicity usually associated.

A closed attractor of more than one dimension encloses a finite region in phase space. All trajectories within the enclosed region can sometimes either become entrained by the bounding attractor, or be continually forced away from the enclosing boundary. Regions in phase space containing an attractor, where all starting points for trajectories in that region, terminate at the attractor, are called basins of attraction. Some or all of the region bounded by a closed limit cycle may form part of its basin of attraction.

The boundary between basins of attraction is a trajectory that can also be an attractor of more than one dimension. For some systems some of their attractor basin boundaries may not necessarily be smooth. Some irregular boundaries it can exhibit the additional property of being either self-similar or otherwise non-smooth, at all scales of the systems dimensions. In this case it is referred to as a fractal boundary.

Strange attractors are a class of attractors usually associated with chaotic nonlinear systems, although they can exist in non-chaotic systems too. They can be temporary or non-moving permanent structures and usually have non-integer dimension. A key property of strange attractors is that the gross system behaviour on a strange attractor is distinct from that found on other attractors. The system state moves with a fixed sequential path over the attractor manifold for most other multi-dimensional attractors. For example in a limit cycle the system state moves in one direction around a periodic orbit. However trajectories near a strange attractor converge towards it in the same way as they do with other attractor manifolds. Once entrained by the strange attractor the gross behaviour of the system is quite different in that the system state can move to any other point on the entrapping manifold in a seemingly random way. But even with this seemingly random behaviour, some complicated but cyclic behaviour can be captured by visualising the system time evolution using either a Poincaré section or a recurrence plot. A key point to note is that the system behaviour entrained to a strange attractor can produce processes that appear to be random, in one or more of the system state variables, but such processes are fully deterministic. This rather alarming assertion is what marks such chaotic behaviour as different from true stochastic behaviour. Both appear to be random but only chaos is deterministic. However, because of the extreme sensitivity to initial conditions exhibited by chaotic systems it is almost impossible to actually predict the course of the chaotic random process in any real-world practical chaos system.

The mere presence of a permanent stable attractor does not always cause all nearby trajectories to converge towards it (or diverge from it). The nonlinear system may be configured such that other transient attractors appear that serve to seduce a trajectory temporarily.

The second meaning of the term system state can now be more easily understood. This use of the term ‘system state’ refers to a behaviour of the system at a gross level, such as periodic stable behaviour or bounded chaotic behaviour inside a basin of

attraction or unchanging state when terminated at a fixed point. In these examples the values of the system variables (the state vector) may be fixed or changing but they can only take on values that are constrained in some way. The constraint will be a limit cycle, a region of phase space bounded by an attractor a fixed point or one of the other features described in this section.

In summary, a bounded or constrained set of different state vectors that all result in the same gross system behaviour gives the definition of the second meaning of the term 'system state'. This meaning will be used throughout the rest of this thesis unless it is specifically made clear to the contrary by evoking the 'state vector' clarification.

2.3.7 Dynamic behaviours of nonlinear systems

In this section the dynamic behaviour of several variants of a system model based on the Duffing nonlinear system are described and illustrated. The aim is to provide a good grounding the type of dynamic behaviour that should be expected when the given system is configured in different ways. The simplest system is the starting point, which is an homogeneous (unforced) and linear system, before moving onto damped variants. Finally the results using the version used in the rest of this thesis are presented, i.e. the fully nonlinear, damped and forced Duffing system. At each step, examples of the time-series output and the phase space behaviour are given.

The full version of the Duffing system model was defined in Equation (2.15). Note that the form of Equation (2.15) uses the convention of a negative stiffness term. Consequently a *positive* value of α results in *negative* linear term scaling, and vice versa. The variants of the Duffing base model investigated in this section are defined

in Equations (2.23), (2.24) and (2.25).

$$\ddot{x} - \alpha x = 0 \tag{2.23}$$

$$\ddot{x} + \delta\dot{x} - \alpha x = 0 \tag{2.24}$$

$$\ddot{x} + \delta\dot{x} - \alpha x + \beta x^3 = 0 \tag{2.25}$$

Indication of the dynamic behaviour of a system can be found by investigating three properties of the system. The existence and position of all fixed points, the existence of complex roots for the system (where they can be calculated), and the nature of any damping factor. The analysis method used to reveal the nature of these properties for an homogeneous differential equation can be illustrated by using Equation (2.25) in an example. Note however, the same procedure can be applied to all three second order homogeneous (autonomous) systems shown in Equations (2.23), (2.24) and (2.25). The example analysis proceeds as follows.

1 Reduce the second order equation to a system of two first order equations. If the equation (or system) is already first order, this step can be omitted. Equation (2.25) reduces to the following:

$$\dot{x_1} = x_2$$

$$\dot{x_2} = \alpha x_1 - \beta x_1^3 - \delta x_2$$

2 Find the Jacobean matrix of the first order system.

$$\boldsymbol{J} = \begin{pmatrix} \frac{\partial \dot{x_1}}{\partial x_1} & \frac{\partial \dot{x_1}}{\partial x_2} \\ \frac{\partial \dot{x_2}}{\partial x_1} & \frac{\partial \dot{x_2}}{\partial x_2} \end{pmatrix} = \begin{pmatrix} 0 & 1 \\ \left(\alpha - 3\beta x^2\right) & -\delta \end{pmatrix}$$

3 Find the fixed points of the system, which are defined as follows:

$$\begin{aligned} \dot{x_1} &= x_2 &&= 0 \\ \dot{x_2} &= \alpha x_1 - \beta x_1^3 - \delta x_2 &&= 0 \end{aligned}$$

The three fixed points are therefore found at $x = 0$, $x = \pm\sqrt{\frac{\alpha}{\beta}}$.

4 Use the Jacobean to investigate the nature of the fixed points. Substitute each fixed point value in turn, into the Jacobean. The eigenvalues (λ) of each of the three resulting matrices are then found, as the roots of the determinant of $(J - \lambda I)$.

$$\det(J - \lambda I) = \lambda^2 + \delta\lambda - \left(\alpha - 3\beta x^2\right) \tag{2.26}$$

The nature of the eigenvalues (the roots) found from the resulting characteristic equation, Equation (2.26), determine the stability and type of the fixed points, and therefore the dynamic behaviour of the original system near the fixed points. Real valued roots be positive or negative, and when the roots are complex, the real part may be positive, negative or zero. These combinations determine the classification of the fixed points as follows.

- Both real, one positive one negative. The fixed point is a saddle point and the dynamics are always unstable.
- Both real, both positive. The fixed point is an unstable node
- Both real, both negative. The fixed point is a stable node
- Both are complex, both real parts are positive. The point is an unstable focus
- Both complex, both real parts are negative. The point is a stable focus
- Both complex, both real parts are zero. The point is a centre

When a fixed point has been identified as an unstable point (of any type), then the system will be characterised by phase space trajectories that diverge away from the point. How the trajectory diverges is different for each type, for example the

dynamics follow a divergent spiral path around an unstable focus.

Inspection of Equation (2.26) shows that the nature of the roots is determined by the values assigned to α, β and δ. For example assigning $\alpha = -1$, $\beta = \delta = 0$ in Equation (2.25) and using the analysis method described above, generates complex eigenvalues with a zero valued real part. In this case, the fixed points are classified as centres. Closed trajectories around (and near to) a centre can be ellipses. However, for this case, the phase space trajectory remains at fixed distance from the centre. This is the Simple Harmonic Motion (SHM) case. The dynamics for this case are illustrated in Figure 2.3 (a) shows the phase space trajectory and the displacement time-series is shown in (b). By introducing a small positive damping factor into the system, $\delta = 0.1$, the eigenvalues are still complex but both real parts are now negative. The fixed point is therefore classified as stable, and nearby trajectories in phase space will spiral into the point. This case is illustrated in Figure 2.3 (c), with the corresponding displacement time-series shown in (d).

A similar analysis was applied to Equation (2.24) to find the behaviour of that system. The damping factor was set non-zero so an oscillatory output with reducing amplitude is expected. Figure 2.3 ((c): phase space and (d) time-series) shows the implemented model exhibits this behaviour, further validating the model.

Equation (2.25) introduces the nonlinear term, controlled by the scaling factor β. The analysis of the fixed point for this system was carried out in the same way as described earlier. The introduction of the nonlinear term significantly modifies the function by generating two new stable equilibrium points when α in Equation (2.25) is positive. In all the work described in this thesis these are always symmetrically positioned either side of $x = 0$.

The point $x = 0$ itself is also changed into an unstable point. Equation (2.25) is a damped, unforced nonlinear system. The presence and sign of the damping factor

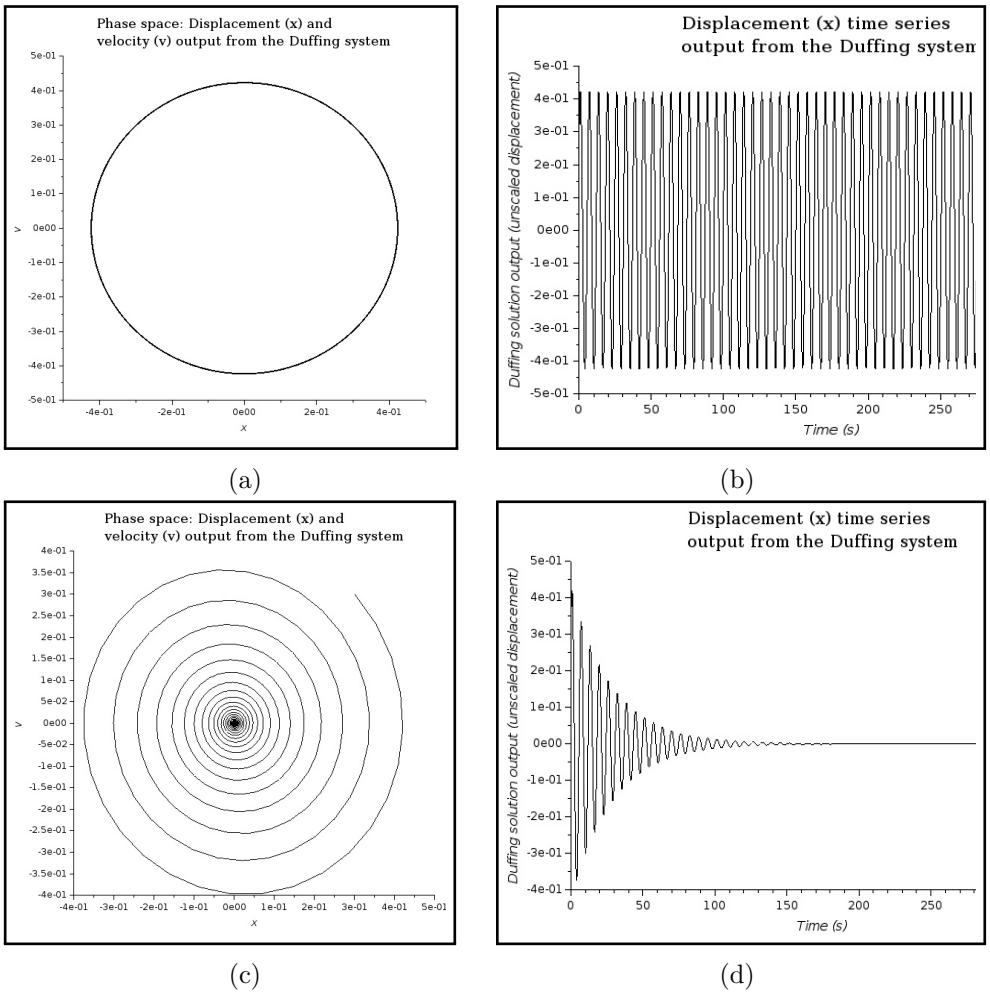

Figure 2.3: Unforced Duffing behaviours (linear cases): a) Phase space; linear, unforced no damping ($\alpha = -1,\ \beta = 0,\ \delta = 0$), the 'simple harmonic motion' (SHM) case. b) Time-series for the SHM case, ($\alpha = -1,\ \beta = 0,\ \delta = 0$). c) Phase space; for the damped SHM case, ($\alpha = -1,\ \beta = 0,\ \delta = 0.1$). d) Time-series for the damped SHM case, ($\alpha = -1,\ \beta = 0,\ \delta = 0.1$)

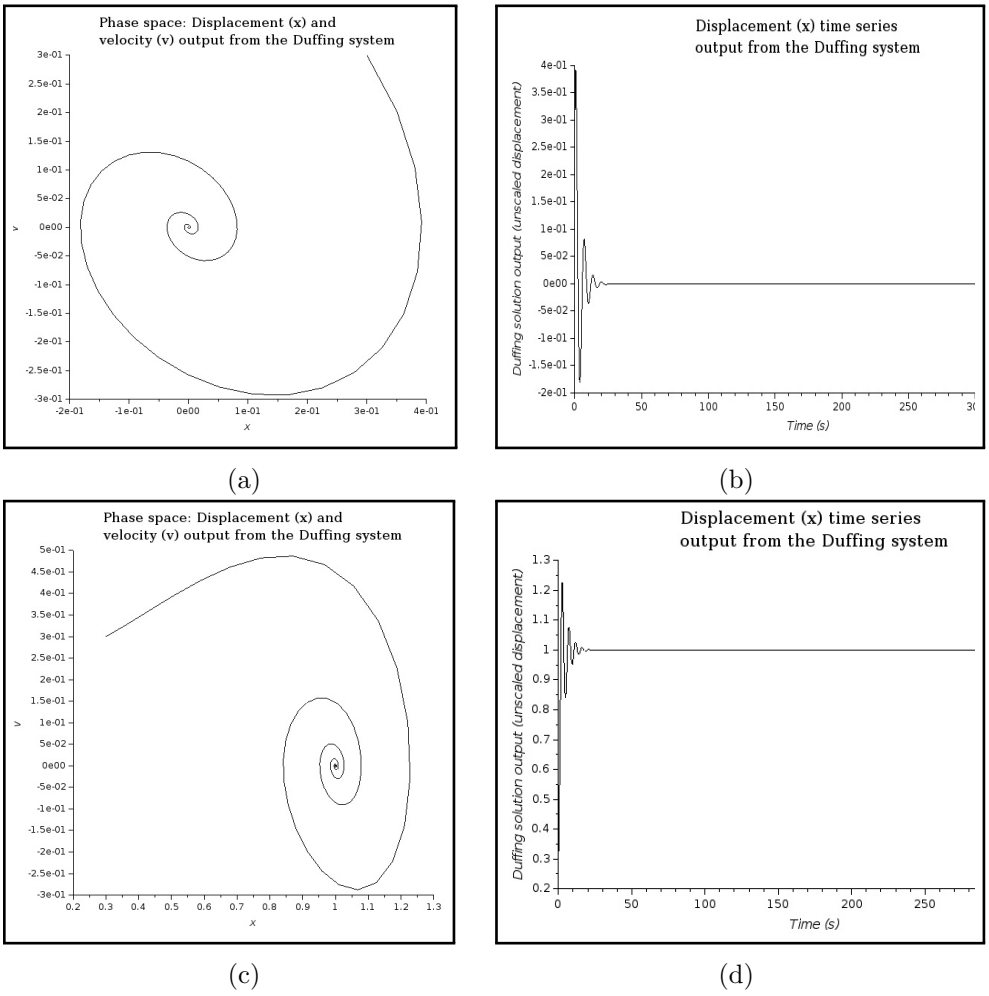

Figure 2.4: Unforced Duffing behaviours (nonlinear, damped cases): a) Phase space; nonlinear, unforced, damped ($\alpha = -1,\ \beta = 1,\ \delta = 0.5$) b) Time-series; ($\alpha = -1,\ \beta = 1,\ \delta = 0.5$) c) Phase space for the positive linear coupler case; ($\alpha = 1,\ \beta = 1,\ \delta = 0.5$). d) Time-series for the positive linear coupler case; ($\alpha = 1,\ \beta = 1,\ \delta = 0.5$).

means a decaying amplitude output should be expected. Setting the input linear scaler α to a *negative* value results in a positive scaling of the linear displacement term. This configuration does not generate any real-valued equilibrium points other than the single (trivial) solution at $x = 0$. A decaying output with amplitude should be expected. Figure 2.4, phase (a) and time-series output (b), confirms this is the case. The plots (c) and (d) of the same figure show the same system but with a *positive* α value input. The output will be oscillatory for α positive or negative, provided the system is not critically damped. However, in the positive α case, the

dynamic will occur in the region near one or the other of the two stable fixed points (at $x = -1$ and $x = 1$). In the case illustrated, the dynamic behaviour converges to $x = +1$ because the initial conditions set were both positive. It can easily be demonstrated that with a negative value for the displacement initial condition, the output dynamic converges to the negative equilibrium point at $x = -1$.

Clearly the two additional equilibria play an important role in the nonlinear system behaviours. These equilibria are discussed in terms of an energy function, in more detail in the Section 2.4.1.

2.4 Nonlinear systems and signal detection

The next three subsections in this chapter are primarily included to provide some minimum necessary background to the use of SR as a pre-processing stage to improve detection performance. Before describing the energy in a bistable nonlinear system and the conditions necessary for the mechanism of SR to manifest in the system, it is necessary to first describe what SR is. SR refers to an amplitude enhancing resonance between a periodic force such as a sine wave, and the *average* rate of transition between states in a dynamic system initiated by a random (stochastic) force. The transition in this context refers to the transition between two stable states (the bistable system), when the combined energy of the stochastic and the periodic forces is sufficient to maintain a regular periodic transition. The dynamics of a nonlinear system in a state of SR, is usually characterised by a noisy periodic orbit. A sufficient energy supplied by the two forces, is therefore required in order to move the system from a quite different and lower energy dynamic, to one of SR. To understand this better, the next section describes the energy in a nonlinear system in detail.

2.4.1 Energy in nonlinear systems

The concept of an energy function is a powerful tool to understand SR. The energy function can be derived from the model for a nonlinear system such as Duffing. Examination of its behaviour is a useful way of visualising how such systems can be controlled and used for weak signal detection by the mechanism of SR. Capturing the effect of various forcing regimes (noise or periodic) and the variable controlling parameters will enable the choice of configurations for optimal detection. The background ideas described in this section will be employed primarily in the investigations of SR in Chapter 3. The analyses in this section are carried out using the Duffing system, but the same arguments apply equally to the Langevin system, which will be used extensively in the SR investigations.

The Duffing nonlinear oscillator system used in this thesis, Equation (2.27) can be regarded as a summation of forces. The force terms $\ddot{x}$ and $\delta\dot{x}$ are dynamic forces that varies with time, whereas the terms $-\alpha x$ and $+\beta x^3$ combine to form a stiffness term, the spring restoring force, that varies with displacement.

$$\ddot{x} + \delta\dot{x} - \alpha x + \beta x^3 = \gamma \cos(\omega_0 t + \phi) + A\cos(\omega t) + n(t) \tag{2.27}$$

Derivation of the potential energy function can be found using the standard 'work' integral. The potential energy V is calculated by integrating the restoring force F_s applied, over an displacement range $x = l_2$ to $x = l_1$, as follows.

$$V = \int_{l_1}^{l_2} F_s dx$$

For the Duffing system the potential energy is:-

$$V = \frac{\beta x^4}{4} - \frac{\alpha x^2}{2} \tag{2.28}$$

The potential energy function of Equation (2.28) is shown in Figure 2.5.

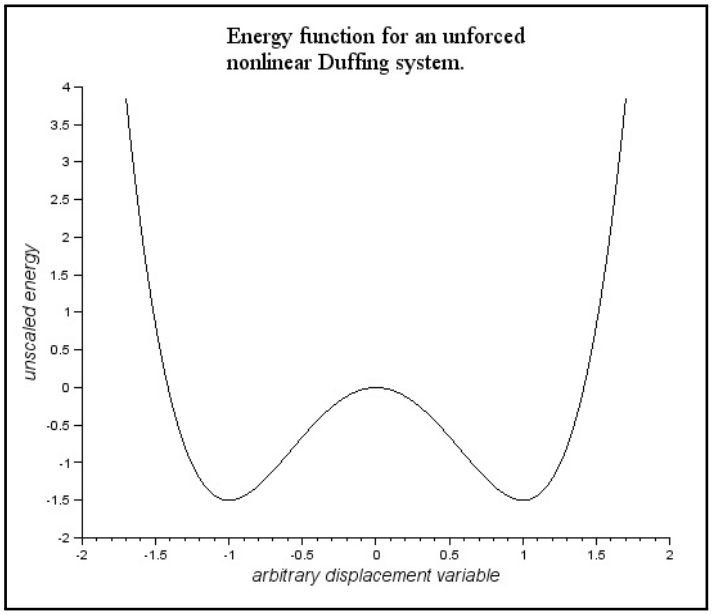

Figure 2.5: Energy function example. Generated by the model of Equation (2.28) In this example the coupling terms were arbitrarily scaled as $\alpha = \beta = 6$, however the two energy wells (at $x = \pm 1$ in this example) will always exist but the height of the energy barrier between them reduces as α and β reduce

There are several features to note in Figure 2.5 and in particular, which system parameters control the feature. The energy function shown is clearly that of a symmetric double-well system, frequently termed a bistable system because the function exhibits two stable minima. The third fixed point at $x = 0$ is unstable. The height of the central raised energy 'barrier' is defined by $\alpha^2/(4\beta)$, α and β are the linear and nonlinear coupling factors in the Duffing system of Equation (2.27). The position of the two minima are defined by $\pm\sqrt{\alpha/\beta}$, in a symmetric bistable system.

However, this model needs to be modified to reflect the forced Duffing system used in the work described in this thesis. The inclusion of the forcing terms from the right hand side of Equation (2.27) in the derivation of the new energy function mean it is no longer a solely potential energy. The modified energy function E, now contains a mixture of potential energy V and some additional kinetic energy terms, is shown for a Duffing system in Equation (2.29). The derivation, which now includes three (right hand side) forcing terms (two periodic and one stochastic), is derived in the same way

as before.

$$E = \frac{\beta x^4}{4} - \frac{\alpha x^2}{2} + xA\cos(\omega t) + x\gamma\cos(\omega_0 t + \phi) + xn(t) \tag{2.29}$$

The forced system energy function of Equation (2.29) is different to the unforced case in that it is no longer static with time, because all three force terms on the right of Equation (2.27) are time dependent. The behaviour is revealed in Figure 2.6, periodic forcing rocks ([57, 47]) the energy function in plot (a), and stochastic forcing destroys the smooth nature of the function but does not rock the overall form of the function, see plot (b). It is the combination of both these force types that can lead to stochastic resonance (introduced in Chapter 2 Section 2.5), provided the *static* energy function well depths are slightly higher than the rocking energy provided by a periodic force, then the further addition of a stochastic force supplies sufficient energy to overcome the potential energy barrier and pass the *system state* back and forth between the wells with a period related to Kramers' rate (see Section 2.4.2).

It must be pointed out that while the method of illustrating how the energy function is affected by the forcing terms, is the same as used in earlier work ([57, 47]), the method 'looses' the *dynamic* force terms on the left of Equation (2.27), $\ddot{x}$ and $\dot{x}$. The rocking motion (a) and the noise motion (b) shown in Figure 2.6 are still valid. Including the 'lost' time varying force terms may be expected to alter the simple noisy rocking motion shown in Figure 2.6. However, the impact on SR is not expected to be great because, in general, the right hand side forcing terms will have a significantly different amplitude compared to the left hand side time varying terms of Equation 2.27.

2.4.2 Kramers' rate

During 1940 H. A. Kramers developed a theory governing chemical reaction rates based on models of the Brownian motion of particles and the amount of thermal excitation (reviewed within [47]). The concept has been applied to more general

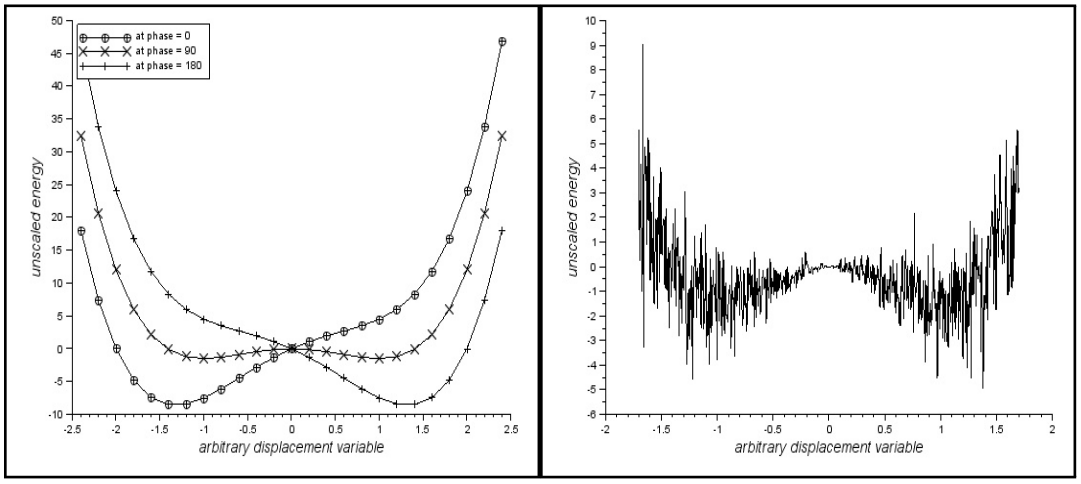

(a) (b)

Figure 2.6: Energy function example. (a): The energy function rocks with a period equal to the frequency of the drive force. Three time-snap shots at phases $\Phi = \{0, \pi/2, \pi\}$ shown. (b): No periodic forcing, extreme additive Gaussian noise ($\sigma = 1.6, \mu = 0$).

nonlinear systems particularly those with double well energy potentials where random processes can excite the system to jump between the wells with a predictable period. Kramers' rate emerges as a condition on the existence of stochastic resonance in a nonlinear system and will be discussed and applied further in Section 2.4.3.

In the context of nonlinear systems, Kramers' rate is a means of describing the average period with which a dynamic 'particle' will transition between the potential wells in a potential energy double-well system such as Duffing when a stochastic forcing input is present.

There are several different versions of the equation for Kramers' rate, as applied to nonlinear models [20, 58, 47]. The variation tends to depend on whether the nonlinear system has had variable re-scaling applied, whether a term for friction is excluded [20] and/or how the frequency is defined. The original Kramers' rate equation contains additional terms that can be simplified for high *friction* cases. This corresponds to *overdamping* in unforced systems such as an unforced Duffing system. The simplified form governing the average well to well transition rate, was re-stated by Gammaitoni

[47] (from Kramers' original 1940 paper), and shown in Equation (2.30).

$$k_r = \frac{\omega_n \omega_b}{\pi\sqrt{2}\gamma_k}\, e^{\left(\frac{-\Delta V}{D}\right)} \tag{2.30}$$

Where $\omega_n =$ resonant frequency of the unforced nonlinear system

$\omega_b =$ a transition rate associated with the slope over the energy barrier

$D =$ Diffusion coefficient (the noise amplitude factor)

$\gamma_k =$ Kramers' friction term

$\Delta V =$ the energy barrier height

Equation (2.30) is the representation found for one limiting case where γ_k is large $\gamma_k >> \omega_b$. The term γ_k itself is called viscous friction in the chemistry literature and normally represents a mechanism that either slows down or speeds up a chemical reaction rate. This is the 'large friction' case, in some treatments [20, 59] the system in consideration is considered to be 'overdamped' when the friction term is set to a value of $\gamma_k = 1$. In the context of Brownian motion it is sometimes regarded as a scaled temperature or thermal excitation term. In the work described in this thesis it will be assumed that the energy of the noise will be fully encapsulated in the diffusion coefficient (noise) term of Equation (2.30) D. The two terms ω_n and ω_b have been described as frequency terms [47], and elsewhere [58] as '..related to the slope of the potential barrier...'. Specifically, ω_n is described as the frequency of the potential in the minima of a double well system, and ω_b is the frequency at the top of the potential barrier [47].

The behaviour of the double well potential function $V(x,t)$ in the presence of a periodic forcing term was described in Section 2.4.1, where it was shown that a periodic force such as $\gamma\cos(\omega_0 t) + A\cos(\omega t)$ will cause the potential function to rock back and forth with time (for example see Figure 2.6). Therefore the potential barrier

height in one energy well will be different to that in the other, most of the time. A transition of the phase space trajectory of the dynamic system from the low barrier well to the higher barrier well in that half of the cycle of the periodic forcing will be more likely than a transition in the other direction. In other words the probability of transition (or escape as it is sometimes termed) is direction dependent when a periodic force is present. The connection to stochastic resonance stems from the fact that if the system is appropriately configured, a periodic forcing term alone will not provide enough energy for the system to transition between the wells, the potential barrier between them always has a finite value. The addition of another forcing term, stochastic noise, may just provide the required additional energy for the trajectory to escape. The key point is that the cycle of escape back and forth is now initiated by the addition of noise, and it is maintained mostly periodic with much greater amplitude, by the original periodic forcing. Occasionally the noise fails to provide enough energy because it is random. The relevance to the current work lies in the phrase just used 'appropriately configured' (for stochastic resonance). The investigations in later sections of this thesis look at configuring nonlinear systems to operate as nonlinear detectors using two different phase space trajectory transition mechanisms. Given one unknown input noisy signal, is it possible to trigger both transition mechanisms when they seemingly require different signal to noise ratio regimes to do so.

Note that the height of the central potential energy barrier in a bistable system is given by $\Delta V = \left(\alpha^2/4\beta\right)$. This has significance not only in the stochastic resonance discussions of Chapter 3 but also in the topic of alternative Duffing configurations investigated in Section 4.6.

2.4.3 Conditions for stochastic resonance

Most of the conditions and bounds governing the occurrence of SR in a system were established in theory based work by early researchers [43, 60, 61, 62, 47]. This early work centred on bistable non-linear systems and at first it seemed that bi-stability

was a necessary condition for SR to exist. Since then SR has been demonstrated in monostable systems [63].

The following list is a summary of the main set of conditions for SR to exist. Unfortunately the published material does not always make it clear if these conditions can be individually labelled as necessary, sufficient or both. However the consensus is that if the system meets them then SR can probably be found provided the system is configured appropriately.

- The system must be nonlinear and subject to at least two types of forcing; one periodic and one random (stochastic)
- The periodic force must be 'weak'. Qualitatively this is related to whether the system can transition the potential barrier (see Figure 2.5) by obtaining energy solely from a single periodic force alone. A periodic force imposes a time evolving rocking motion on the otherwise static (unforced) energy function. Such a force is considered 'weak' if the force rocking motion amplitude never causes the central energy barrier height to become ≤ 0, in either of the energy function minima.
- The principle SR condition is the so called time scale matching condition $T \approx 2T_k$ [61], where T is the time period of the periodic force and T_k is Kramers' time, which is the time is period corresponding to the *average* stochastic *one way* transition between stable states. Kramers' time is the inverse of Kramers' rate and this leads to the SR *rate* condition, Equation (2.31).

$$\omega = \frac{k_r}{2} \tag{2.31}$$

  The factor 2 is a consequence of the original formulation of Kramers' rate, which was designed as model of *one way* chemical reactions. The condition provides an upper bound on the periodic frequency, stochastic resonance always rapidly reduces at periodic force frequencies higher than $\frac{k_r}{2}$. The time scale matching condition has been described as ensuring the forcing frequency is much slower than the rate adiabatic limit in the chemical reaction [60], which is the time taken to achieve

stability or equilibrium in one stable state or the other. In this sense it probably related to the same mechanisms that govern the length of the chaotic (or stable) transient found in the Duffing system, which was discussed previously, starting at Section 4.6.

- SR was discovered to exist in the Langevin system if the variance of the additive noise is confined within certain bounds determined by the forcing frequency and its amplitude. Upper and lower bounds on the noise variance $\sigma_1^2 \leqslant \sigma^2 \leqslant \sigma_2^2$ were first suggested by Benzi *et al.* [43, 64]. The Langevin system was originally developed as model for Brownian motion. This system can be used as an alternative formulation of the model of a nonlinear system such as Duffing, it incorporates a noise term and a generalised energy function term. The variance bounds are not strictly a condition for SR, but the are an indication of how to configure a system SR to occur.

Note that none of the conditions have any dependence of any given specific nonlinear system such as the Langevin or the Duffing system. However, its existence does clearly depend on certain generic aspects for example bistability in the energy function of the system [60]. In this case though it has been shown that bistability is not a necessary condition, recent work has shown the existence of stochastic resonance in systems that are not bistable [63]. Therefore bistability is at least a sufficient condition.

The energy minima in symmetric bistable system are found at $\pm\sqrt{\alpha/\beta}$, as described in Section 2.4.1. The energy barrier height can derived from the static potential energy function (Equation (2.28)) by setting $x = \sqrt{\alpha/\beta}$, and for the barrier maximum, by setting $x = 0$. The difference between the two energy levels gives the barrier energy (height) ΔV in Equation (2.32). Note here that symmetry of the energy function is now inherently assumed, asymmetry would produce different values ΔV for either side of the barrier.

$$\Delta V = \frac{\alpha^2}{4\beta} \tag{2.32}$$

The periodic force term critical amplitude required in the absence of noise, A_c to cause a dynamic trajectory to just surmount the barrier is given by Equation (2.33) [65].

$$A_c = \sqrt{\left(\frac{4\alpha^3}{27\beta}\right)} \tag{2.33}$$

A_c, α and β are the critical (periodic SR) amplitude, linear coupling and nonlinear coupling respectively. The SR condition of a weak periodic signal discussed earlier is related to Equation (2.33). The signal is considered weak if the amplitude of the periodic component is less than A_c [20].

The work reported here is based on a Duffing system implementation without variable re-scaling or frequency normalisation. A practical detection system based on SR will need to be controllable for a wide frequency spectrum, and for unknown input data statistics. Therefore the system parameters of most interest are the additive noise variance and the frequency. The frequency of the signal to be detected is cast as the periodic forcing term satisfying the SR rate condition $\omega = \frac{k_r}{2}$. Selecting the required Kramers' rate by configuring the linear and nonlinear coupling values provides a convenient way to fix the range of frequencies that can be detected using SR. Pre-selecting an appropriate variance for the additive Gaussian noise will also provide some amplitude control compared to the scaled (but unknown S/N) input signal. A more convenient version of the Kramers' rate is shown in Equation (2.37), which will enable the type of control of the Duffing system configuration required. This version of the Kramers' rate relation clearly relates to the controlling parameters used in the nonlinear systems considered in this thesis.

Some of the relevant discussion points and equations introduced in Section 2.4.2, and Equation (2.32) in this section, can be used to derive the version of the Kramers' rate relation shown in Equation (2.37). The treatment that the diffusion coefficient D [58] is the same as noise in a noisy signal [47], and the assumption made in Section 2.4.2 that D encapsulates all the noise energy in a noisy signal, leads to the relation in Equation (2.34), where σ^2 is the noise variance. The discussion in section 2 of Gammaitoni et al. [47] describes a Kramers' rate relation for an unforced and frequency normalised system, such that $\omega_n = \omega_b = 1$. However, for the non-normalised systems considered in the context of SR in this thesis, the relation shown in Equation (2.35) holds. This is consistent with other work [65].

$$D = \sigma^2 \tag{2.34}$$

$$\omega_n \omega_b = \alpha \tag{2.35}$$

$$\gamma_k = \delta \tag{2.36}$$

Kramers' friction term equates directly to the damping factor δ [65] of both the Langevin and Duffing systems' in Equations (2.19) and (2.18). The friction term γ_k can therefore be replaced by the damping term, as shown in Equation (2.36). It is assumed that SR investigated in the Langevin system will always satisfy the large friction assumption [47], where the damping factor is set as $\delta = 1$. The Duffing system is also investigated in Chapter 3, but the value of the damping factor may vary.

Substituting Equations (2.34), (2.35), (2.36) and the relation for the barrier height found earlier (Equation (2.32)), into Equation (2.30) leads to the form of Kramers' rate shown in Equation (2.37). This derivation follows a similar scheme described by Lai and Leng [65].

$$k_r = \frac{\alpha}{\pi\sqrt{2}\delta}\, e^{\left(\frac{-\alpha^2}{\sigma^2 4\beta}\right)} \tag{2.37}$$

Equation (2.37) will be used in all calculations of Kramers' rate carried out in this thesis.

The necessary background understanding required to proceed to the new work described in this thesis, has been established in this chapter. Before proceeding to the next chapter, where the application of nonlinear system properties to signal detection is investigated, it is necessary to review the state of the art for the two nonlinear mechanisms of primary interest in this thesis. The next section reviews Stochastic Resonance advances, and the final section in this chapter, reviews the prior art relating to the transition mechanism.

2.5 Review of Stochastic Resonance

Stochastic Resonance (SR) is the name generally used for the occurrence of a significant increase in the output S/N, reaching a maximum value before decreasing again, all as the input S/N reduces monotonically. It is a nonlinear effect dependent on the system itself. This counter-intuitive mechanism only occurs when a suitable system is configured in a specific way.

SR has been found in several physical systems [66] as well as simulated either using electrical circuits or computer models [67]. Stochastic resonance has also been demonstrated in models including the damped forced Duffing system. A Duffing model was used to investigate residence time distributions as a means to identify the existence of SR [68]. A physical electrical circuit implementation of the Duffing oscillator has also been used to study SR [69]. Analogue circuits have also been used to widen the scope to forced damped bistable systems [61]. The effects of designing

controllable asymmetry into the energy function of a bistable system has been studied [70], and this approach may offer a route to the optimisation of an SR based signal detector. However that investigation is left to future research.

A theoretical basis for SR [60] was established soon after the first identified existence in the Lorenz system [43]. There followed the establishment of theory specifically for bistable systems such as the Duffing system [61, 46]. A common indicator of the existence of SR is the non-monotonic change in the observed S/N, however caution is required when determining the value of S/N [71, 62]. Since these early steps SR has been integrated into detection theory [72, 73]. A key finding is the derivation of the optimum noise probability density function for maximising any improvement in the S/N.

SR cannot improve the input-output S/N gain beyond unity except when the detector is configured so that Linear Response Theory (LRT) no longer applies [23]. There are at least three SR related mechanisms available to optimise a single bistable Duffing system. Firstly, select the optimal pdf of the noise to add. Secondly, select a configuration where LRT is not applicable. Thirdly, configure the Duffing system so that there is an optimal balance in the trade off between it being a suboptimal detector (where SR is applicable [74]) and any other drivers on the system configuration.

In fact the same LRT issue was identified by Inchiosa et al. in their early, but key paper [75] that links SR, coupled systems and specifically the Duffing nonlinear system. It was asserted that a bistable system such as the Duffing system is clearly a system that presents a nonlinear response to certain input stimuli, and so LRT is not necessarily applicable and therefore the potential for greater than unity S/N gain may well exist. But this has not been demonstrated in the Duffing system to date.

More recent work has systematically investigated a Duffing system with asymmetric potential wells. Three types of asymmetry were considered in [70], and the effect on

the output S/N versus the noise level were measured. One metric that can be used to reveal asymmetry in a bistable system such as Duffing, is to consider the average amount of time the dynamics of the system spends within one energy well, compared to the time spent in the other well. This dwell time is referred to as residence time. The start and stop times defining it, correspond to when the system dynamics cross the energy barrier between wells, into or out of a well, respectively [70]. Residence times were measured [70] and found to show asymmetry although the average total residence time in each potential well totalled the periodic drive frequency. The authors point out that SR in an asymmetric Duffing has been studied previously (see references therein) but theirs is the most systematic investigation. A similar investigation of asymmetry was carried out a year earlier by Rajasekar et al. [76], but with some important differences in scope. The subject of the earlier paper was a different form of SR, where the added noise is replaced by a very high frequency periodic term to generate the so-called *vibrational* SR. The paper also approached the topic from a much more theoretical point of view. Vibrational SR will not be investigated further in this thesis but is noted here as a possible avenue for future work.

The Duffing system has recently found application to the modelling of nonlinearities in physical nano-mechanical resonators [77]. The application itself is not of interest to the work reported in this thesis, but some of the findings are relevant. The work considered a quadrature formulation of the displacement and the input of white noise to enable very precise measurement of the resonant frequency of the system. The noise level was deliberately kept below the energy levels required for frequent transition between the two stable basins of attraction. Increasing the noise power is in effect analogous to reducing the difference between the 'natural' frequencies of the two stable basins. The implication on the detection performance when impulsive noise forms part of the input to the Duffing system is discussed in Chapter 5.

The same issues of post system detection, performance analysis, non-Gaussian noise

and non-trivial signals are of interest in SR as they are for the nonlinear oscillator mechanism. In the context of SR some progress has been made individually across all of these issues. For example impulsive noise has been explored [78] but detection performance not fully assessed. More recently nonlinear pre-processing and non-Gaussian noise impact have received attention [34], but the nonlinear elements used were not relevant. The detection performance of SR has been addressed from the point of view of system design [79] and also performance analysis [35], but for SR as a stand alone mechanism only. Different types of additive noise, and evidence that signal to noise enhancement can be greater than unity (in ratio to input S/N) was most recently explored for an array of nonlinear elements [22], but note that the array elements were uncoupled. Although the array was comprised of 'arbitrary nonlinear elements' (not necessarily Duffing oscillators) the key results are still relevant, and are as follows. The nonlinear elements must be sub-optimal, S/N gain (input/output) can exceed unity if the array is large enough and the gain in signal to noise improvement increases with the number of nonlinear elements in the array.

The term Stochastic Resonance originates with Benzi and co-workers in 1981 while investigating the apparent periodic occurrence of climate change markers [43] and [80]. The majority of research effort since 1981 has concentrated on discovering SR in an increasing range of physical and natural systems. Broadly, the goals of that body of work were to first show the existence of SR in the chosen natural system (climate change, neuron firing, lasers [66] etc) then to use models of SR to further explain some of the behaviours observed in the system. Much of this effort is summarised and cited in two comprehensive surveys of SR research, conducted independently. The first was prepared by Mitaim and Kosko in 1998 [81] while more recent work was captured by Gammaitoni *et al.* in 2009 [82]. In parallel a number of researchers have developed aspects of the theory of SR without necessarily basing their approach on real physical or natural systems. A major part of this area of research concentrated on understanding the timings associated with various stages of traversing the energy function (introduced in Section 2.4.1) during well to well transitions as initiated by

stochastic forcing (see for example [68]). The phase state change in time of the output from a stochastic resonant system is determined by the dwell time at each energy state at each point in time during the backward and forward traverse of the energy barrier. Understanding the dwell times leads to an understanding of the shape of the periodic output from the system.

Investigating possible applications of SR appears to be a smaller field of research compared to the body of work focusing more on the theoretical aspects of SR or on discovering examples in nature. Even so, there are a number of researchers who have investigated how SR might be applied to a wide variety of signal detection problems. See for example: signal detection in heavy tailed non-Gaussian noise [35] and in impulsive noise [78], varying the system parameters to optimise SR signal detection [44]. Inchiosa and Kosko provided some of the first research on SR detection performance in coupled systems [75], while work on connecting detection based on SR to conventional detection theory was carried out by Kay [74] and by Hari *et al.* [35]. Asdi and Tewfik also used cascaded nonlinear systems to investigate SR [20] and came to the conclusion that SR based detectors do not suffer from reducing performance with reducing observation time, in the way that conventional matched filter based detectors do.

Over the last 30 years attempts to apply the stochastic resonance mechanism to the detection of signals considered weak in the sense they have low signal to noise ratios, have been made. Such attempts have addressed the detection of gravitational waves [83], fault diagnosis usually in rotating machinery of various types [41, 65], and ultra wideband radio signal detection [84]. Of all these applications by far the largest body of published material deals with the application of SR to fault diagnosis in rotating machinery. The recent publications by Wang *et al.* [41] contains several example citations within. Most of the work related to detection exploits the apparent nonlinear and dramatic increase in amplitude of the coherent (signal of interest) component output from the nonlinear system, that occurs at the onset of SR. The

mechanism causing this was described in terms of the energy in the system in Section 2.4.1 of the previous chapter. The amplitude increase resulting from the system dynamics becoming energetic enough to transition periodically between two energy wells rather than remaining contained within one well, provides most of the motivation in the published research to investigate detection applications.

The first known publication having relevance to underwater acoustics discusses a rather indirect application of SR [85]. The technique uses SR to enhance the performance of a radon transform to select linear features otherwise obscured, in a noisy image. The method is applied to static LOFAR images, which are normally real time updating waterfall time-frequency spectrogram sonar displays. Linear frequency lines appear to be visually enhanced in their example, however there is no quantification of the apparent improvement. Zhang and co workers applied SR as a pre-processing stage to the problem of signal detection in the presence of underwater reverberation noise [44]. This is the only publication found to date that uses ROC analysis, albeit for one particular type of input and only for simulated data. Nevertheless, this is a step forward because a performance measure was used that for the first time enables global comparison of detection performance.

More recently the first papers attempting to apply stochastic resonance to underwater weak acoustic signal detection have been published [86, 59]. In both papers the Langevin model was employed as the nonlinear stochastic resonant system. Real acoustic data in the form of simple transmissions, either single frequency tone pulses or linear frequency modulated chirp [86], were collected and in the pulsed single frequency case, filtered to remove most of the noise power in frequencies away from the signal [59]. The signals were then input into the Langevin system and results displayed either is an increase in output S/N or increase in output amplitude, as evidence that stochastic resonance has in fact occurred. One of the research teams recognises that in a real situation it will often be the case that little or nothing would be known about the nature of the underwater acoustic signal [86]. To mitigate that

problem they apply a simple genetic algorithm to adapt the linear and nonlinear coefficients of the Langevin system to maximise the output amplitude from the system. Crucially none of the papers goes on to apply a recognised metric to measure the detection performance, and neither do they attempt to compare the performance of their stochastic resonance based system to a more conventional linear detection scheme. In short these publications do not answer the question of whether stochastic resonance can enable a detector of underwater acoustic signals to perform measurably better than a benchmark, commonly used detection scheme.

2.6 Review of Nonlinear systems and detection

Many models, originally developed to represent real systems, can exhibit nonlinear and chaotic behaviour. Examples include the logistic or population model, Chua's circuit, Duffing's circuit, Lorenz's weather cell model. Applying them to the problem of signal detection began in the mid 1990's by considering the small perturbations used for chaos control as a signal to be detected, [87]. The tone of the paper [87] implies the application to signal detection was already known however a search for any earlier references has not so far been successful.

The nonlinearity we focus on in our work is a specific chaos to stable transition brought about by a small input perturbation. As far as the author of this thesis can discover, the potential for this basic mechanism to enable weak signal detection was first established in 1996 [88] and then apparently independently in 1999 [4]. Most of the subsequent published material builds on the work of Wang and co-workers [4] and usually focuses on applications, with some occasional progress in advancing understanding. The notable steps include the following. A method of finding the transition point, the phase and the frequency [89], realisation that increasing the nonlinearity in the system may offer better sensitivity [5], and a more formal description of two particular behaviours (intermittent chaos and the transition) [90], [91]. The optimal configuration of the chaotic oscillator was also addressed. The

coefficients of the restoring force (the linear and nonlinear terms combined) can be optimised to achieve lower S/N values at which a signal can be detected [26].

A theoretical basis for selecting appropriate parameter values for a Duffing nonlinear system was also explored [91]. Expressions for the threshold of nonlinearity and amplitude were found and these will contribute to the validation of my work by demonstrating consistency with established findings. The stability of the system was shown to depend on the level of the damping and restoring force coefficients. Instability can be controlled (eliminated) by sufficient damping, even if it is nonlinear [92].

The fact that most work labels the nonlinear transition mechanism itself as a 'detector' is not strictly valid in the sense that a detector is (most commonly) an automated step in the signal processing, that makes a binary decision as to whether the wanted signal is present or not. A simple amplitude threshold test applied after transformation from the time to the frequency domain is an example of a separate, and linear, detector. A true detection scheme implemented as an additional processing step after the nonlinear system has been described [93], however the approach was limited to the application, without a performance measure, of thresholding the Lyapunov exponents. Detection will be explored in more depth in Chapter 5.

The basic nonlinear transition scheme has been applied to fault diagnosis and early fault detection [94, 95], radiated underwater [96] and above water narrowband signals [97], seismic signals [98], tool wear signature [99], GPS signals [93] and blood flow speed measurement [100]. Apart from a few examples (some cited earlier) only limited progress in generalising any mathematical description of the idea has been made and crucially, no complete quantification of how the mechanism affects the final detection stage performance has been carried out. Detection performance assessments will form the bulk of Chapter 5.

The detection mechanism based on a binary classifier is presented with the output

from a nonlinear filter instead of the traditional linear matched filter output. Processing the nonlinear filter output for optimal classifier performance includes applying some measure of the nonlinear change of filter system state caused by the presence of a signal. The most commonly used measure is the first or largest Lyapunov exponent [7] which measures the rate at which adjacent trajectories in phase diverge over time. A positive value for the maximal exponent is taken as one indicator of chaos. However the approach can produce misleading results if the data set is very noisy or very short, because all methods for estimating Lyapunov exponents rely on temporal averaging.

Most recently a simple measure of the minimum radial distance in phase space to the nearest trajectory point [96] was proposed as a measure as the basis for a detection decision. Phase space is described in Section 2.3.4. By the proposed measure a small radial distance value indicates that the nearest trajectory is close and therefore the system is likely to be in a dynamic state of chaos. A larger value is assumed to indicate the system is possibly stable. The algorithm is trivial to implement and is computationally cheap. However the output will have some sensitivity to the initial conditions and for very short data sets the result could be increasingly misleading if the initial transient is not managed carefully.

As we have seen, no published material presenting a *complete* detection performance assessment has been found, but a small number of limited scope performance analyses have been carried out. Most published work tends to echo the two claims of Wang *et al.* [4] that the mechanism is immune to noise and that weak signals having a S/N as small as -26 dB can be detected. These properties, while attractive, are neither a complete nor a robust indication of detection performance because they do not consider false alarm rates.

Noise immunity has become an assumed baseline property and is much quoted in the introduction to many papers looking at applying the Duffing system as a weak signal detector (see for example: [4, 5, 8, 101]). The qualitative definition of noise immunity

in the published material derives from the behaviour of the trajectory in phase space. The observation is that additive noise does not cause the system to exit the basin of attraction of the strange attractor. None of these papers bound or modify the apparent 'universal' nature of the supposed immunity to noise. The most robust examination of 'noise immunity' in Duffing like systems found to date [102] makes the point that noise will affect the neighbouring attractor basins if the intensity is large enough, and that in the case of the Duffing system, any noise effect acts only through the initial start transient observed in nonlinear systems with initial condition sensitivity. Their analysis is also carried out using a modified version of the Duffing system, which differs by the addition of an extra nonlinear term x^5. The qualitative results are still applicable to the work reported in this thesis because both systems (with or without the x^5 term) exhibit one stable and one unstable (chaotic) attraction basin next to each other.

A more recent theoretical analysis of the noise immunity [84] asserts that the noise can do no more than impose a variability on the phase space trajectory without changing the course the basic noise free trajectory would take. This may be a valid finding all the while the noise is small and the trajectory remains in the attractor basin. It will be shown in Chapter 5, that in the context of detection performance the noise immunity claim is by no means true for all signal to noise regimes.

Transition from chaos to stable limit cycle is useful but the reverse transition can also act as a detection indication [94]. The reverse transition method seems to offer wider bandwidth as the input frequencies move away from the drive frequency.

Recently a complex version of the Duffing oscillator has been used to detect complex signals [8], interestingly this is one of the few publications to consider probability of detection as another measure of performance rather than just the minimum S/N and the ubiquitous claim of 'definite immunity to noise'. However, the publication stops short of a full detection performance assessment.

Chapter 3

Stochastic Resonance

3.1 Introduction

In this chapter the mechanism of Stochastic Resonance (SR) is considered for its potential as a signal processing technique applied to the detection of narrow band signals mixed with additive broadband noise. In particular the aim is to quantify the impact of SR on detection performance when considered as a pre-conditioner to improve a signal detection processing scheme. The investigation proceeds within the context of the application of SR to underwater weak acoustic signal detection. In Chapter 2 some basic properties of SR in context of the energy function of a nonlinear system were discussed. It was established that prior researchers have made some initial steps in applying SR to signal detection. However in most of those applications the signals of interest were in a high signal-to-noise regime or there was some prior knowledge of the signal that could be exploited in the detection scheme. Very little research looks at applying SR to underwater weak signal detection, or to adequately measuring the performance of the SR based detection scheme.

To recap, SR refers to an amplitude enhancing resonance between a periodic force and the *average* rate of transition between states in a dynamic system initiated by a random (stochastic) force. SR occurs in a dynamic system for a particular subset of

all possible parameter combinations that control the system configuration. The commonest indicator of the presence of SR is the onset of a clear and abrupt increase, followed by a slower decrease, in output signal-to-noise ratio (S/N), as the variance of the noise at the input increases for a fixed signal amplitude.

Detecting signals in low S/N is a common problem in passive sonar. In the underwater environment the unwanted components of any input signal might be comprised of ambient noise in the sea, man-made noise, other biological noise, rain and other above water weather noise and underwater seismic events. Can SR be exploited to improve the detection of narrowband signals in the underwater, where they are weak in the sense that the S/N is very low.

The application of the SR mechanism to detection problems in general was introduced and discussed in Chapter 2. Only two publications attempt to apply SR to weak underwater acoustic signals, and no prior work comprehensively measures the impact of SR on weak signal detection performance. Most prior research that investigates detection, tends to consider higher S/N regimes than are usually encountered for weak signals, (underwater or otherwise). The implications of this are discussed in this chapter, particularly the significance for system configuration in a practical detection scheme.

The nonlinear, or anomalous, behaviour in output S/N is usually presented in published research in a way that implies it may offer benefit in signal detection or for other signal processing tasks. The language used is most often very positive, describing an 'increase' in S/N, and asserted in the context of signal detection. The underlying system behaviours that generate the apparent anomalous increase in output S/N (which is usually labelled as SR) have not so far been presented, and certainly not as a wider view of the behaviours at lower and higher S/N regions. The concept that SR (the peak in output S/N) is beneficial is investigated and quantified in this chapter.

3.2 Outline of chapter contents

The chapter opens by first defining some basic aspects of the methods and approach used, including system model definitions. Then follows a consideration of the behaviours and properties of the SR mechanism. The chapter includes a quantification in terms of metrics such as S/N, where SR will occur within the configuration/parameter space of the defined nonlinear systems. The existence of SR in both the Duffing and the Langevin systems is confirmed, and the means to control it in order to exploit it for signal detection is also established.

This chapter also serves to introduce the application of the metrics, which will be used throughout the rest of the thesis. A brief discussion on the use of input/output nonlinear system gain will be made, in particular on its suitability as a measure of detection performance. The basics of Receiver Operating Characteristics (ROC) analysis was introduced in Chapter 2, and ROC curves will be measured for all SR cases discussed in this chapter.

The latter part of the chapter predominantly investigates and describes the application of SR to a few realistic underwater weak acoustic signal scenarios, this is restricted to simulated signals. The detection performance with and without nonlinear SR pre-processing, is measured in each scenario and comments on the utility and outcome of the scheme made.

3.3 Methods

The approach taken in this chapter is to define two suitable nonlinear system models, confirm the existence of SR in them, collate the conditions for SR and understand how SR can be controlled in those systems. The chapter will also establish how SR can be used to improve signal detection, demonstrate a SR based detection scheme and measure the detection performance as compared to that of a suitable and more

commonly used signal processing scheme. The nonlinear systems are treated as a pre-processing stage, with a separate detection stage that follows. Detection is a simple binary decision on whether the signal is present or absent, based on a fixed amplitude threshold set in the frequency domain.

3.3.1 System model definitions

The configuration and form of any chosen nonlinear pre-processing systems is crucial to how they behave. All of the work described in this chapter will be carried out using the following two nonlinear system models. The main model used in this chapter is the Langevin system, with some comparative assessment made using the Duffing system. The two systems were introduced in Chapter 2, and the versions of each system used in this chapter are re-stated below:

$$\text{Duffing} \qquad \ddot{x} + \delta\dot{x} - \alpha x + \beta x^3 = F_i(t) \tag{3.1}$$

$$\text{Langevin} \qquad \dot{x} - \alpha x + \beta x^3 = F_i(t) \tag{3.2}$$

The both systems use two additive forcing terms (one *periodic* and one *stochastic*), which are modelled in the same way; $F_i(t) = A\cos(\omega t + \phi) + n(t)$. Together the two force terms form the modelled signal input to the nonlinear system. The output is derived by numerical solution using either the Heun method or the fixed step 4^{th} order Runge-Kutta method.

3.3.2 Signal to noise ratio

The S/N metric is used extensively in this chapter, either as a calculated value based on the amplitude and deviation values used to generate simulated signals, or as an estimated value based on measured noise and sine wave power spectrum levels. The concept of S/N was introduced in Section 2.2.2, where it was defined in the most

commonly encountered form, and this version is repeated below.

$$snr = \frac{A^2}{2\sigma^2} \tag{3.3}$$

The true values of the signal amplitude and noise variance are usually unknown quantities in a real underwater acoustic signal detection scheme. Therefore to estimate the S/N it is necessary to measure the average noise and average signal power. The method for estimating the snr (and SNR) by using measured data taken from a power spectrum, was described in detail in the latter part of Section 2.2.2 in the previous chapter. The measurement method is used in this chapter.

3.3.3 Normalisation

The normalised (dimensionless) Langevin system used in this chapter follows the scheme proposed by previous workers [47]. The derivation of the re-scaling scheme was described in detail in Chapter 2 Section 2.3.3. Three generic reasons for normalising a system were also offered in that section. Agreement with the methods used in previous research and a reduction in the number of controlling parameters, were the primary reasons for the re-scaling used here. Controlling severe divergence in the numerical solution (the third reason offered) was found to be less of an issue for the Langevin system used in these SR investigations.

The full re-scaling scheme aimed to render all the components of the Langevin system dimensionless. The approach primarily concentrated on removing the dimensions of force from each term in the system model, by finding a suitable mixture of the existing parameters, which in combination, had the inverse dimension for each term. A similar approach was used to render the time factor as dimensionless. The now re-scaled version of the Langevin system was then implemented as part of an encoded model where solutions were found using a the RK4 method.

3.3.4 Methods of assessing performance

In this chapter measuring the detection performance of a system based on SR will be carried out using ROC analysis. The technique of ROC analysis was described in Chapter 2. ROC analysis is a robust approach to measuring detection performance as it provides a valid and quantified comparison between widely different detection schemes and associated signal processing, because the method is independent of the detection scheme being measured.

3.4 Demonstration of SR in two systems

It is necessary to demonstrate SR in the chosen models to illustrate how a detector will function, to show how the conditions for SR are met and therefore show how SR can be controlled and how the model performs as a pre-processing stage before the detection stage. The first system investigated was the Langevin system (see Equation (3.2)), and the variation of output S/N with input noise deviation was selected for investigation because it is the indicator most commonly used to visualise SR.

The Langevin system was configured for the normalised case, where the parameters of the system were set as $\alpha = \beta = 1$. The simulated input signal was composed of two additive parts, a sine wave and a Gaussian white stochastic (noise) term. The periodic component amplitude was fixed at a sub-threshold value of 0.18 for all simulations in this section. The energy barrier height between minima in a bistable system determines a critical amplitude, above which the system can begin to switch between energy minima periodically. If the periodic component has an inherent amplitude greater than this critical or threshold amplitude A_c the behaviour is called supra-threshold SR. Using Equation (2.33) leads to a value of $A_c \approx 0.385$, which is greater than the periodic amplitude used in this section $A = 0.18$. The system in this case is configured to exhibit sub-threshold SR.

Using Equation (2.37) and setting the model as a normalised system ($\alpha = \beta = 1$) the Kramers rate for the Langevin configuration used here is $k_r \approx 0.22$. Recall that Kramers rate describes the *one way* transition between two energy minima. One key condition for SR to exist is that the periodic force must have a frequency $f \leqslant (k_r/2)$. Note the distinction between the existence of a 'Kramers rate' for a system, and the condition for SR imposed by 'half the Kramers rate'. The four plots shown in Figure 3.1 illustrate the effect of incrementing the sine wave frequency from $f = 0.01045$, which is << half the Kramers rate, to approximately twice the Kramers rate.

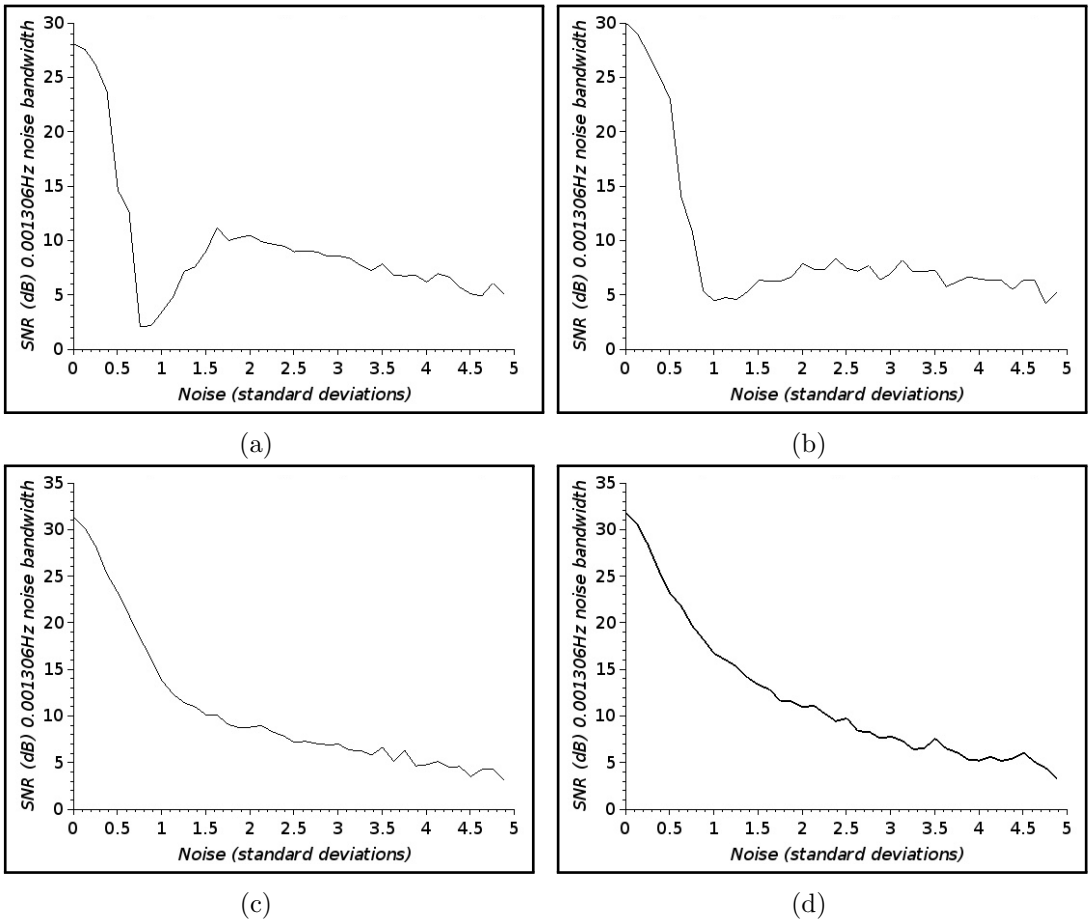

Figure 3.1: Langevin system SR variation with increasing frequency. Output S/N variation with noise deviation. The four plots reveal the disappearance of the signature SR peak as the frequency increases to approximately twice the Kramers rate. a) frequency = 0.01045, b) 0.03005, c) 0.10975, d) 0.44032. The Langevin system was normalised: $\alpha = \beta = 1.0, A = 0.18$.

The Kramers rate for the re-scaled dimensionless system described here will always become asymptotic to the same value because in such a normalised system it is dependent only on the noise (σ) and is independent of the remaining control parameters (forcing frequency f and periodic component amplitude A).

Figure 3.1 shows four plots at four different input sine wave frequencies. All four plots show the S/N (value in decibels, SNR) measured at the output of the Langevin system, for increasing input additive noise deviation σ. With the sine wave amplitude fixed constant the input S/N is therefore decreasing as the added noise increases. Each of the four plots were generated from the average of 30 runs. The precise values of four chosen frequencies were selected so that the energy in the sine wave falls in the centre of a frequency bin in the frequency domain, for the fixed sample rate used in all simulations in this section. This will always be referred to as a 'bin-centred' frequency, and was previously described in more detail in Section 3.3.2.

Figure 3.1 plot a) (the lowest frequency) illustrates the existence of SR in a normalised Langevin system by the presence of a peak in output S/N at noise deviation $\sigma \approx 1.8$. To the left of the peak there is a sharp decrease in the S/N as input noise reduces. To the right of the peak the S/N decreases with increasing input noise, but more slowly. In plot b) the SR peak is still evident but shifted up to an input noise value of $\sigma \approx 2.5$, and the output S/N at SR peak is lower. Note also that the low S/N point that occurs before the SR peak has also increased as frequency has increased.

Once the force frequency f becomes equal to, and then exceeds, half the Kramers rate for the system configuration (plots c and d respectively) then the nature of the output S/N behaviour changes. The SR peak disappears and the variation in output S/N becomes monotonically decreasing with increasing input noise. The absence of a SR peak at the two higher frequency plots (c and d) is as a result of the system being driven at a frequency either at or significantly above half the Kramers rate, which violates the SR Kramers rate condition ($f \leqslant k_r/2$).

The key observation is that the cause of the disappearance of the SR peak is not because the output S/N value at the SR peak position has significantly reduced, but because the output S/N value in the valley to the left of the SR peak dramatically increases as the force frequency approaches $k_r/2$. At higher frequencies the output S/N ceases to change with frequency, even at noise levels corresponding to the position of the 'valley'. At these higher frequencies it stabilises to a monotonic variation with input noise level.

The results in Figure 3.1 also indicate the upper frequency bound on the utility of the Langevin system imposed by half the Kramers rate, assuming any exploitable benefit exists at or near the stochastic resonant peak. At higher frequencies the system exhibits linear behaviour. The impact on detection performance for input S/N values that span the nonlinear and linear behaviours seen in Figure 3.1, is examined in Section 3.6.

The existence of SR in Duffing is well established [70, 43, 83, 19], consequently this system was chosen as the next nonlinear system to be considered in the characterisation of SR for detection, for three reasons. Firstly to provide a comparison with the Langevin system in order to confirm similarities in SR behaviours for a functionally similar system configuration. Secondly to introduce the damping factor as an additional configuration parameter, and demonstrate its impact on SR. Thirdly to complete the final step towards a practical signal conditioning system prior to a detection stage, by investigating the so called large parameter SR. The third reason is investigated fully in Section 3.6.

To compare the SR behaviour of the Duffing system to that of the equivalent normalised Langevin configuration, all configuration controls for the Duffing system were set identically to those used for the Langevin investigation described above. As before the simulated input signal comprises two force terms; a sine wave and a white Gaussian noise term. All data were generated from 30 averages for each of the simulation runs. Also as before the output S/N was measured as described in Section

3.3.2 with the S/N noise bandwidth indicated on all figures. Table 3.1 below summarises the Duffing configuration.

Parameter/variable	Value
Linear coupler α	1
Nonlinear coupler β	1
Sine wave amplitude, A	0.18
Damping factor δ	1
Frequency f	0.01045 and 0.10975
Spectral averages	30
Sample rate	11.11111
Noise	Gaussian white
Half the Kramers rate k_r	≈ 0.11

Table 3.1: Duffing configuration: Sine wave amplitude set as sub-threshold ($A < A_c$). Both frequencies were chosen to be bin-centred in the frequency domain.

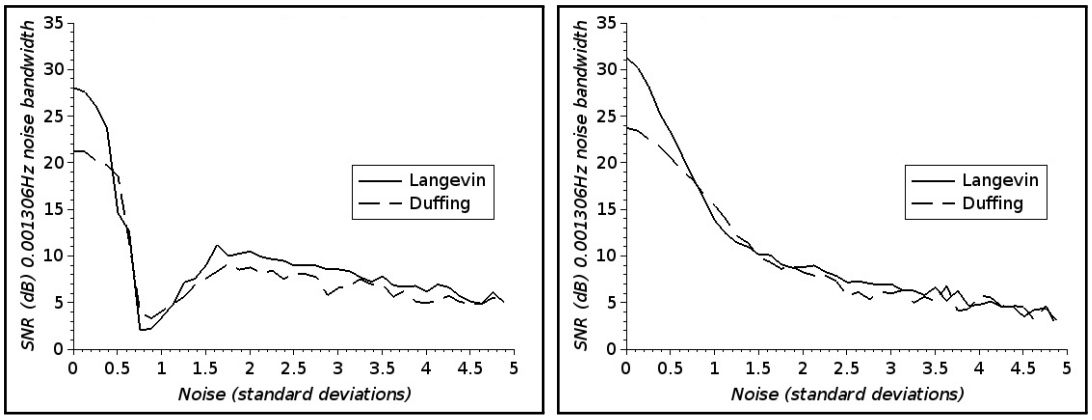

(a) Frequency = 0.01045 Hz. (b) Frequency = 0.10975 Hz.

Figure 3.2: Stochastic resonance observed in the Duffing system and compared to Langevin. Continuous lines (both plots) are re-plots of lower left and lower right plots of Figure 3.1. 30 data averages at each noise deviation value. (a): Frequency is bin-centred $\approx (1/10)\,(k_r/2)$. (b): Frequency $\approx (k_r/2)$, at the onset of linearity.

Figure 3.2 shows results for a configuration of the Duffing system that enables comparison with the Langevin derived data shown previously. The output S/N curves for the Duffing system are plotted at two frequencies along with the corresponding result found previously for the the Langevin system. The corresponding Langevin

data are repeated from Figure 3.1 plots a) and c), above. The behaviours of the Duffing system are broadly similar to that observed for the Langevin system.

The impact of varying the damping factor of the Duffing system can now be examined. The Duffing configuration of Table 3.1 was re-used, with the force frequency set to $f = 0.01045$ which meets with the Kramers rate SR condition so SR is expected. Three output S/N data sets were generated at three different damping factors. The three cases were; a severely over-damped Duffing system $\delta = 1.0$, the near-critical damped case $\delta = 0.5$ and an under-damped case $\delta = 0.2$. The three results are shown in Figure 3.3. The noise deviation value corresponding to the position of the SR peak in S/N value, is different for each of the three damping cases, falling at $\sigma \approx \{1.8, 1.4, 1.0\}$ respectively. However the variation in damping has little effect on the output S/N value at the SR peak.

One approach to designing a practical detector might be to ensure that the onset of SR occurs at the lowest input S/N possible by severely over damping the nonlinear system. Controlling SR by the addition of more noise as a third forcing term therefore becomes attractive as the widest possible range of input S/N values can be accommodated.

3.4.1 Linear and nonlinear regions

Quantitative comparison of the variation in S/N at input to, and output from, a nonlinear system reveals the true nature of the behaviour of the nonlinear system as the input S/N reduces. Similarly, a quantitative comparison of the variation of the power in the periodic component with that of the noise power at the same frequency, when viewed separately, provides an explanation of the SR behaviour.

Two signals with different amplitude sine waves were investigated, both amplitudes were less than the critical amplitude A_c so that both present sub-threshold SR. White Gaussian noise added as before to make a simulated noisy input signal. The

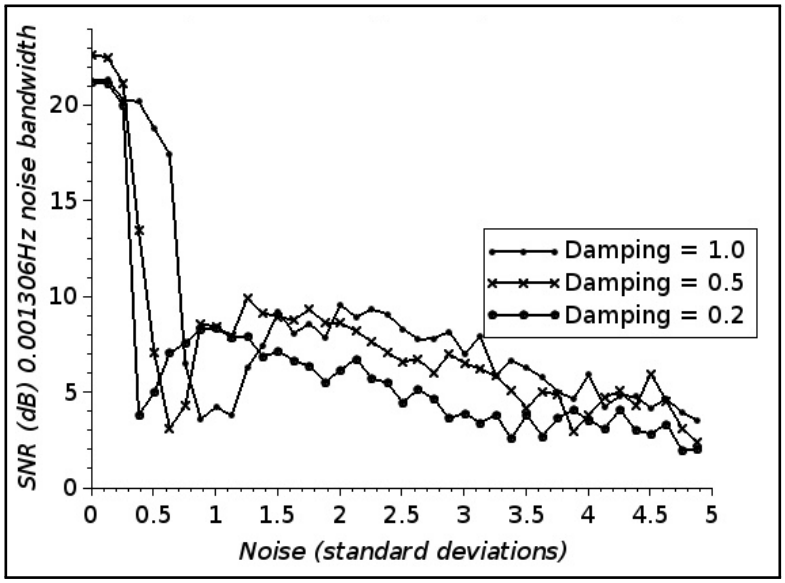

Figure 3.3: Stochastic resonance observed in the normalised Duffing system at three (δ) damping values. 30 data averages at each noise deviation value. Frequency 0.01045 Hz, is bin-centred $\approx (1/10)\,(k_r/2)$. Configuration: $\alpha = \beta = 1$, sine wave amplitude is sub-threshold at $A = 0.18$

normalised Langevin system was used as the pre-processor and the output time-series was transformed to the frequency domain. The input noise deviation was incremented for between simulation runs, with data obtained from 30 averages at each deviation value. Narrowband S/N values were measured as previously described, from the frequency transformed and averaged data. In addition the input S/N's were also measured from frequency transformed input signal data, averaged in the same way. The signal generation sample rate and numerical solver step size were selected to ensure the same noise bandwidth existed for input S/N calculations as for output S/N's.

The input and output data were plotted as S/N versus noise deviation in Figure 3.4, plot a) at sine wave amplitude $A = 0.3$ and plot b) at $A = 0.1$. In both plots, at no point does the output S/N level exceed that of the input S/N, for the sine wave in white Gaussian noise case. The lack of input/output gain in this sub-threshold SR, simulated input signal case is in agreement with previous findings [103, 25]. Figure 3.4 further indicates that no improved detection performance should be expected

when operating at the SR peak. This finding is considered further in Section 3.5, by quantifying the detection performance for different input signal types .

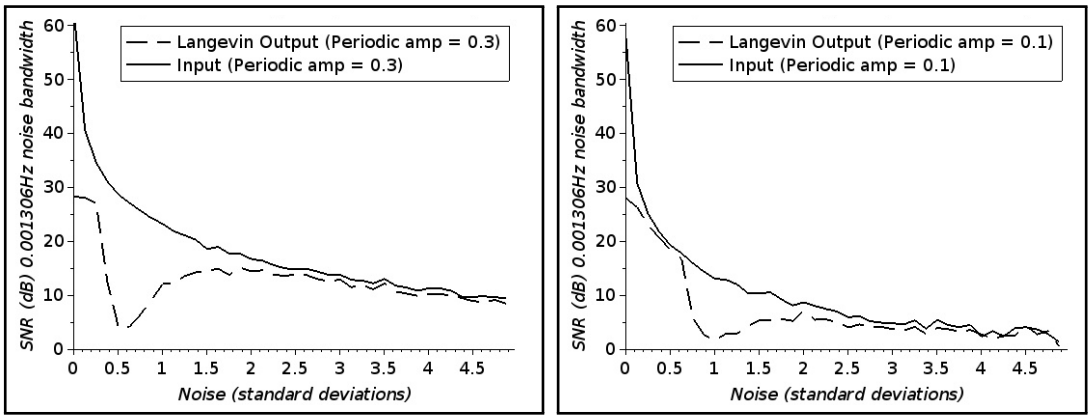

(a) Input amplitude $A = 0.30$ (b) Input amplitude $A = 0.10$

Figure 3.4: Nonlinear regions of output S/N. Stochastic resonance observed in the Langevin system. Frequency = 0.01045 Hz. $\alpha = \beta = \delta = 1$. S/N calculated using 30 realisations at each noise deviation value. Periodic component, critical amplitude $A_c = 0.345$.

The concept that SR is a 'peak' in output S/N that may provide some benefit for weak signal detection can now be challenged. Figure 3.4 supports an alternative view, the case for this proceeds as follows. The output S/N at first follows a gradual monotonic reduction in both plots of Figure 3.4, as the input S/N (noise deviation at a fixed sine wave amplitude) reduces. In plot (a), where $A = 0.3$, the gradual monotonic reduction abruptly changes at a noise deviation $\sigma \approx 0.3$. In plot (b) ($A = 0.1$) the same abrupt change occurs at $\sigma \approx 0.65$. At higher deviation values the abrupt change manifests as a sudden and significant reduction in output S/N. The tentative finding is that the input noise deviation value where this sudden reduction in output S/N occurs, appears to be inversely dependent on the amplitude of the sine wave component of the input simulated signal.

After the large reduction the output S/N then recovers back to close to the linear behaviour (exhibited by the continuous line, input *snr* curves), as the noise deviation increases. The nonlinear behaviour of the output from a Langevin system configured

for SR can now be seen as comprising three regions (near-linear, nonlinear, linear) that occur in a sequence that corresponds to three input S/N regimes (high, medium, low). Therefore, rather than consider SR as a 'peak' in output S/N at specific noise deviation values, it should be more accurately considered as generating a collapse in output S/N at lower, but equally specific noise deviation values corresponding to the 'nonlinear' region described above. For the input signal type and Langevin system configuration used to generate Figure 3.4, the near-linear, nonlinear, linear regions are; plot (a) $\sigma = \{< 0.3, 0.3\text{to} \sim 2.5, > 2.5\}$, and (b) $\sigma = \{< 0.65, 0.65\text{to} \sim 3.0, > 3.0\}$

Examination of the amplitude of the sine wave at the output compared to the noise floor reveals the origin of the collapse in output S/N. The averaged data used above to calculate the output S/N at each noise deviation increment (Figure 3.4) were separated into two sets of power spectrum levels, the measured noise-only power and the sine wave plus noise power. This was carried out for both input sine wave amplitude cases.

The separated power data plotted against noise deviation value are shown in Figure 3.5, plot (a) for the input sine wave amplitude $A = 0.3$ case and plot (b) for $A = 0.1$. Both plots show a variable but always positive, difference between the signal and noise power curves. Note that the S/N dashed lines of Figure 3.4 equate to this difference. The noise power (dashed lines) exhibit an abrupt increase at the same deviation values as the dip in S/N found earlier. At a slightly higher noise deviation there is an equally sudden increase in output sine wave power. At still higher deviation values the difference in the two power curves reaches a second maximum (the first being at extremely low σ). The (second) maxima for the two input amplitude cases occur at $\sigma \approx 1.8$ in plot (a) and $\sigma \approx 2.0$ in plot (b), which agrees with the two corresponding SR peaks shown in Figure 3.4 earlier.

It can now be seen that the primary cause of the collapse in output S/N is shown to be a sudden increase in the noise floor, which occurs at slightly higher input S/N

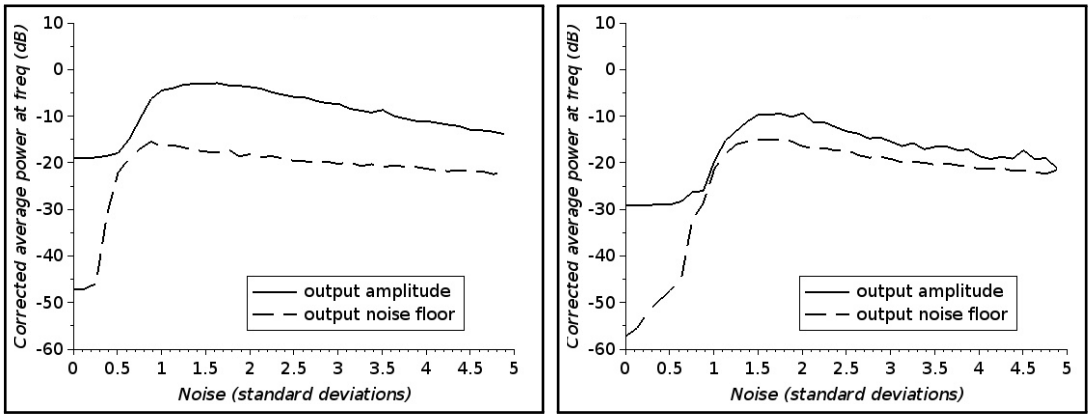

(a) Input amplitude $A = 0.30$ (b) Input amplitude $A = 0.10$

Figure 3.5: Output signal amplitude and noise power spectral levels. Drive frequency $f = 0.01045$ $\alpha = \beta = 1.0$, S/N calculated using 30 realisations at each input noise deviation level.

values (i.e. 'earlier' in terms of noise deviation) than for the increase in sine wave amplitude. As the noise deviation increases the energy in the system also increases to a value sufficient to cause random transition between the two potential energy minima in the bistable system, whether the periodic component is present at the input or not. The result is the sudden 'cliff face' as the noise floor power increases dramatically. The narrowband signal power also exhibits a sudden increase for the same reason, but this increase lags the onset of the noise-only transitions. The S/N is the ratio of the noise power and signal power shown in Figure 3.5, and it is the lag between the increases in these two powers which causes a collapse in output S/N.

3.5 Detection performance: Normalised systems

3.5.1 Simple detection performance

In the preceding sections some key nonlinear system behaviours and underlying causes of the SR effect were established. Some insight into controlling the occurrence of SR by varying some system parameters was also gained. In this section the basic detection performance for an input signal composed of white Gaussian noise and a

sine wave can now be quantified. The two force terms of the Langevin system shown in Equation (3.2) and described in Section 3.3.1 (noise and the periodic component) represent the input signal, where the noise term ($n(t)$) is Gaussian white noise and the periodic term is a sinusoid with; $A = 0.04$ and $\phi = 0$. The sine wave amplitude and additive noise are both sub-threshold. The optimum performance of the detector is expected when the preceding nonlinear stochastic resonant signal conditioning stage achieves its best output S/N. To test this the detection performance is measured using ROC analysis, at three input signal to noise ratios as indicated by the three noise deviation values of Figure 3.7.

Detection is achieved by transforming the time-series output of the nonlinear system into the frequency domain, and selecting a threshold for the frequency bin corresponding to the sine wave frequency. A detection scheme of this type clearly does not represent a real practical detection system because prior knowledge of the frequency bin where the sine wave will occur is used to perform the 'signal present' or 'signal absent' counts that form the basis of the ROC analysis. However the approach adopted here does provide a benchmark ROC comparison method (albeit favourably offset from the expected ROC of a realistic system), where all the factors affecting ROC are controlled. The ROC analysis comprises a pair of simulation runs, one with signal present and one with it absent. A single independent white Gaussian noise realisation is generated for each iteration pair, the same noise is used in both runs. The simulated noise is re-seeded and re-generated between iteration run pairs to produce independent but identically distributed noise.

The assumption that SR enhances detection performance can now be tested. In order to demonstrate the impact on the ROC curves it is necessary to reduce the input S/N compared to that used previously in this chapter, so that the ROC curves are positioned to clearly reveal any differences resulting from different system configurations and detection schemes. ROC curves can be viewed as encapsulating information on how separated the signal-plus-noise amplitude distribution is from the

noise-only amplitude distribution. The S/N metric also encapsulates information from the *same* amplitude distributions. However, it is more analogous to measuring how different the *mean* value of the amplitude distributions of both the signal-only and noise-only cases are. If no averaging is used the S/N metric measures a single snapshot of the separation of the amplitude values of the two cases at one point in time. At high S/N the well separated distributions will generate ROC curves with near maximum true positive rates approaching 1.0 even at almost zero false alarm rates. This type of curve presents on the ROC plot at an extreme position to the left and top of the graph area. In this 'perfect detection performance' state, additional changes to the system intended to separate signal and noise still further may well succeed but the change cannot improve the ROC curve position any further. Similarly, very low input S/N values correspond to ROC curves that form a straight diagonal line from bottom left to top right of the ROC curve plot, and additional system changes detrimental to the detection performance cannot degrade the ROC curve position any further.

It has been shown in previous sections that the occurrence of SR in relation to the input noise deviation can be varied by changing the sine wave amplitude, but remain sub-threshold This provides a useful control to tune the position of the ROC curves on the ROC analysis plot in order that they do not present at either of the two extremes described above. In this way all the resulting ROC curves positions can be tuned to present on a ROC plot in positions that usefully reveal the effect of smaller variations in input S/N. This will not affect the positioning of the ROC curves *relative* to each other, performance comparisons are therefore robust.

The normalised Langevin configuration was used, the drive frequency chosen as $f = 0.01045$. In order to tune the ROC curve positions a good input sine wave amplitude was found by trial and error to be $A = 1.0$, which is sub-threshold and reduced to about 1/4 the critical amplitude. The system energy barrier height is fixed and transition between stable minima requires the same energy as before. Therefore a

consequence of the sine wave amplitude reduction is that larger noise deviations were required to initiate SR, in other words the SR peak occurs at higher noise deviation values and lower input S/N.

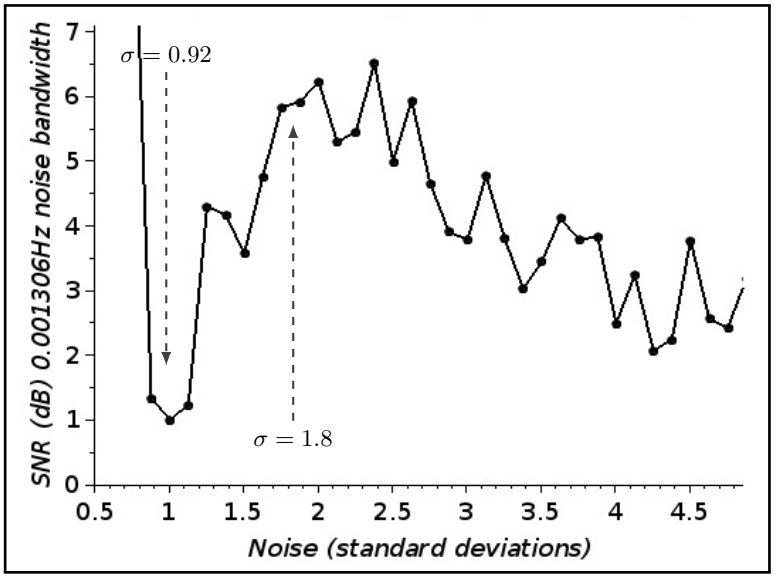

Figure 3.6: Output narrowband S/N variation with noise deviation. Normalised Langevin system $\alpha = \beta = 1.0$, frequency $f = 0.01045$, sine wave amplitude $A = 0.1$. The indicated noise deviation values; ($\sigma = 0.92$ and $\sigma = 1.8$) were used in generating the ROC curves of Figure 3.7.

The output S/N variation as a function of input noise deviation was found first and is plotted in Figure 3.6. Two noise deviation values were selected from Figure 3.6, at the minimum and (SR) maximum output S/N. The minimum in output S/N at $\sigma = 0.92$ corresponds to higher input S/N compared to the SR maximum in output S/N (at $\sigma = 1.80$). ROC analyses using 500 realisations were carried out at the selected deviation levels, with and without the Langevin system pre-processing stage present in the detection processing chain.

The processing chain with the Langevin pre-processing stage removed forms a linear detection scheme. The detection performance of this linear system was obtained by ROC analysis, and the resulting ROC curves are the benchmark representing the performance of a commonly used linear detection approach. Since the input signal is

white Gaussian noise added to a sine wave, near optimal detection performance is expected from the linear detection scheme.

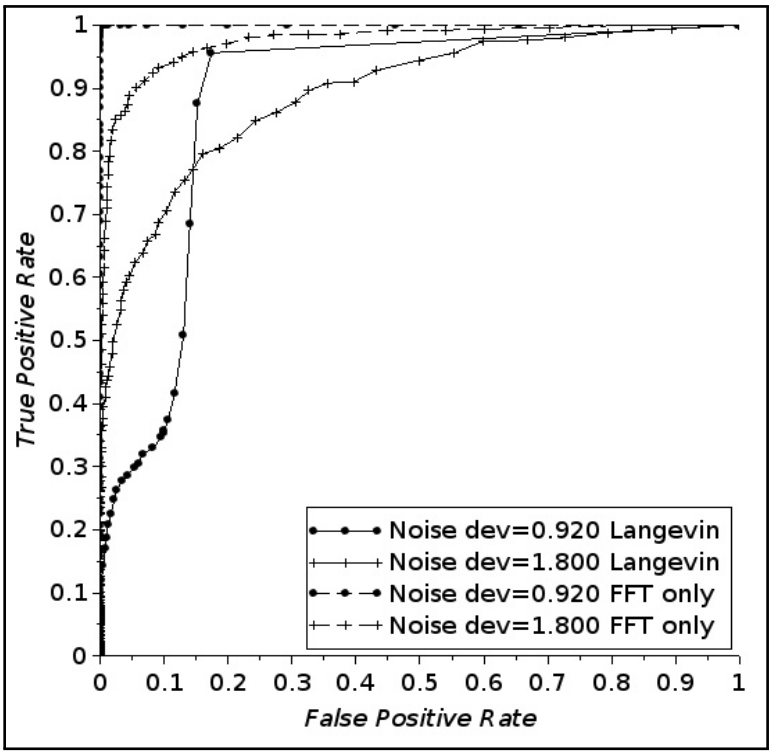

Figure 3.7: ROC Analysis. At two noise deviation values, FFT only (benchmark) ROC curves included for performance comparison. ROC curves generated using 500 realisations. Normalised Langevin system detection performance, and compared to the linear benchmark case (FFT only with no Langevin pre-processing). Low input S/N with sine wave amplitude $A = 0.1 < A_c \approx 0.385$. Frequency of sine wave meets the Kramers rate condition ($f = 0.01045 << (1/2)\, k_r \approx 0.225$).

Figure 3.7 shows two pairs of ROC curves. The first pair measure the detection performance at an input noise deviation of $\sigma = 0.92$ (filled dot marks), and the second pair at an input deviation of $\sigma = 1.8$ ('plus' symbol marks). The lower deviation value corresponds to the extreme collapse in output S/N, in the nonlinear region described in Section 3.4.1. The higher value marks the SR peak, the maximum in output S/N for this system. The two ROC curves for the Langevin pre-processor configuration show very poor performance in general, and always worse than the benchmark detection configuration. At the SR peak point the Langevin ROC curve is nearly

symmetric about anti-diagonal line, and indicates a significantly better performance at low false positive rates than the Langevin ROC measured when the output S/N is low ($\sigma = 0.92$).

The severe asymmetry in the ROC curve measured for an input noise of $\sigma = 0.92$ can be explained as follows. The significant reduction in output S/N occurs over the noise deviation region 0.5 to 1.2 (Figure 3.6), where the nonlinear system exhibits almost no transitions between the two energy minima because the energy of the input signal is too low. The system dynamics are confined to a trajectory that is almost exclusively contained within one energy well. At noise deviation values higher than ~ 1.2 the system begins to transition between wells increasingly more frequently, and at first the timing of the transitions is almost exclusively random.

At deviations between $\sigma \sim 1.2$ and about 1.8 the system spends periods either transitioning with the sine wave frequency, or oscillating at the sine wave frequency within one energy well, or randomly transitioning between wells or even transitioning at rates other than the input sine wave frequency. The length of time the system spends in any of these states is random, and the change to another of the states is also random. However the proportion of the total time spent in the first state begins to increase with increasing input deviation. As the input noise approaches $\sigma = 1.8$ the first state becomes dominant until it is the only state, at SR.

As the system starts to transition the amplitude distributions for both the noise-only (N) and (at a slight lagged time) the signal-plus-noise (S+N) become bimodal. This represents the two distinct amplitudes, one associated with noisy oscillations within a single energy well and the higher amplitude mode associated with transitioning (noisy oscillations between wells). The morphing system states described above manifest as a growing second peak and a reducing first peak, in both bimodal distributions (N and S+N), as the input noise level increases. The original first peak in the two amplitude distributions has largely disappeared at $\sigma = 1.8$ i.e at the SR and the system reverts to a mono-modal distribution.

Incrementing a *single* threshold across bimodal (N and S+N) amplitude distributions to generate the ROC data results in quite large and rapid increases in the number of False Positive counts (FP) at low False Positive Rates (FPR). This leads to a collapse in the ROC curve at low FPR. This effect is clearly seen on the ROC analysis of Figure 3.7 in the curve for the Langevin system at input noise $\sigma = 0.92$, where the collapse occurs at FPR below about 0.15. The asymmetry in that Langevin ROC curve results from an equally sudden recovery of the ROC curve back to an apparently better detection performance, at FPR higher than about 0.15. The FPR value at which the ROC curve transitions from very poor (low detection performance) True Positive Rate (TPR) values to very good TPR's forming the asymmetric 'S' shape, is believed to depend on how well separated the *second* 'N' mode is from the the *first* 'S+N' mode.

While the ROC curves shown in Figure 3.7 is valid as far as a single threshold (binary decision) detector is concerned, it is possible that a more sophisticated detector might generate better detection performance. For example, one option is to add a further processing step at the output of the nonlinear system, to separate transitioning and non-transitioning time-series', treating each to its own binary detector.

3.5.2 Impulsive noise

The input signal used in the simulations of the preceding sections of this chapter have all used the additive combination of Gaussian white noise with a sinusoid, where the Gaussian noise acted as a simulation of real noise. For underwater signal detection it is often the case that the background noise can be made up of many different types of source [104]. Under certain conditions the noise background has been shown to be anything but Gaussian [105]. Rayleigh-mixture, K distribution and log-normal (impulsive) have all be found to be a better fit to the statistics of some types of underwater noise, when compared to the Gaussian model.

The contributors to underwater ambient noise were introduced in Section 3.1. In this section one particular type of underwater background noise is considered. Biological noise can vary in frequency content, loudness and localisation, all depending on the particular sound generating species. One of the loudest sounds is generated by the snapping or pistol shrimp (Family: *Alpheidae*, with more than 1000 species), making a highly impulsive noise. The sound made by dense colonies of snapping shrimp can present some of the most extreme and challenging conditions for detecting an acoustic signal of interest. The sound is generated by a triggered closure of one of the shrimps claws creating a cavitation bubble that collapses to produce the main impulse noise spike [106]. The result is a very loud click or impulsive noise. The sound levels of groups of snapping shrimp have been quantified in order to understand the impact on sonar [107]. Simulating the main impulse noise event, and measuring its impact on the ability to detect a sine wave is the subject of this section.

The simulated signal mixture comprises three additive components; white Gaussian noise, a single tone and simulated impulsive noise. The mixture is artificially generated and input to the Langevin system. Inspection of a typical snapping shrimp impulse time-series shows initial large, finite time length, positive and negative going components with a longer and smaller amplitude noisy decaying oscillating tail. The initial positive and negative components can be modelled using an extremely low variance Gaussian distribution function (Equation (3.4)). The coded implementation of the impulse signal generation runs two Gaussian functions, one positive going and one negative going, with a fixed but very small time (three sample points) gap between them.

The generator then stitches together first the positive spike then the negative spike. The size of any one spike in the whole sequence is controlled by three factors; the noise deviation value that generates the Gaussian white noise (added later), a spike size factor randomly selected from between 0.1 and 8 and a third fixed multiplier of size 6. The last factor ensures the spike levels appear considerably larger than the Gaussian

noise deviation. The inclusion of the Gaussian noise deviation as a factor ensures the impulsive noise power scales linearly as the added Gaussian noise level increases. The time between spike pairs is also uniformly random. The signal generation code allows selection of the density of spike pairs in a given overall time length. The impulsive noise sequence is then added to the sine wave and the white Gaussian noise sequences.

$$I_t = \left(\frac{1}{a\sqrt{\pi}}\right) e^{-(t/a)^2} \tag{3.4}$$

The combined input signal comprising the three parts is shown as a time-series in Figure 3.8, for the noise deviation $\sigma = 1.8$.

The two noise deviation values corresponding to the lowest and the peak output S/N values, were found in the same way described in Section 3.5.1, by generating a plot of output S/N variation as a function of input noise deviation at fixed sine wave amplitude. The impulsive noise controls were fixed throughout but the impulse noise scales as σ increases as described above. The ROC analysis was carried out in the same way as described in Section 3.5.1 and the results presented in Figure 3.10.

The time-series shown in Figure 3.8 qualitatively illustrates the essential feature of impulsive noise, the presence of large excursions in amplitude. The amplitude distribution function of impulsive noise is therefore characterised by longer tails, compared to the normal distribution function. This feature can be quantified by the kurtosis measure. Unfortunately there are a number of ways of defining kurtosis. The measure of *excess* kurtosis is chosen to quantify all the simulated impulsive signals that are used in this thesis. The kurtosis of a normal distribution is 3, term 'excess' kurtosis simply measures the kurtosis value over and above that found for a normal distribution. Consequently a positive excess is more impulsive than a signal having a normal distribution, and a negative value, less impulsive. The definition of kurtosis (and therefore excess kurtosis) used in this thesis is based on the fourth standardised moment y_e (kurtosis), minus 3. The fourth standardised moment is defined as the ratio of the fourth central moment μ_4 to the fourth power of the standard deviation

σ^4. This definition is summarised in Equation (3.5) below, where for n samples of data x_i:

$$y_e = \left(\frac{\mu_4}{\sigma^4}\right) - 3 \tag{3.5}$$

Where the fourth central moment is 'centred' about the mean μ of the data x_i:

$$\mu_4 = \left(\frac{1}{n}\right)\left(\sum_{i=1}^{n}(x_i - \mu)^4\right) \tag{3.6}$$

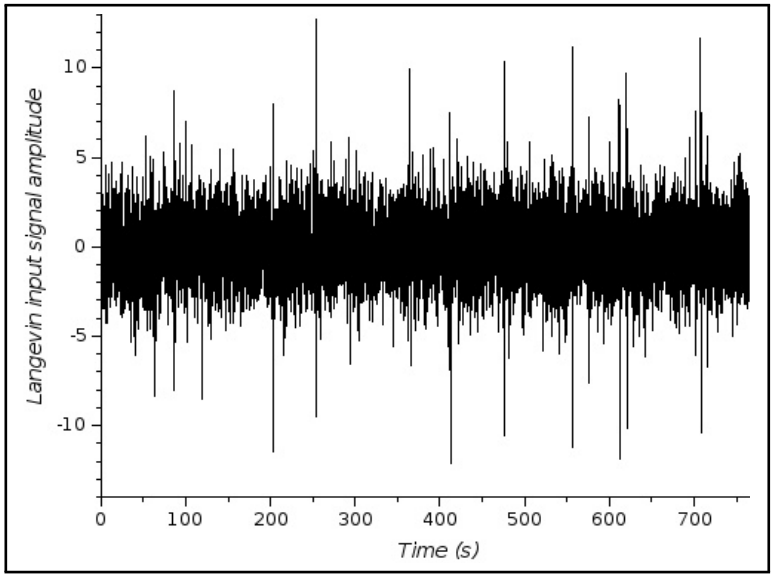

Figure 3.8: Time-series of the input signal. Signal comprises Gaussian noise at $\sigma = 1.8$, sine wave at $f = 0.01045$ and $A = 0.1$, and impulsive noise (arbitrary spike density factor = 65, spike size = $6 \times \sigma \times$ rand(0.1 to 8)). Variance of the combined additive simulated input signal data was measured as $\sigma^2 = 3.88$. Excess kurtosis as defined in Equations (3.5) and (3.6) $y_e = 17.44$.

The detection performance of the detector with Langevin pre-processing is shown by the results in Figure 3.10 to be always worse than the benchmark linear system in both deviation cases, as indicated by their lower ROC curves. The orthogonal

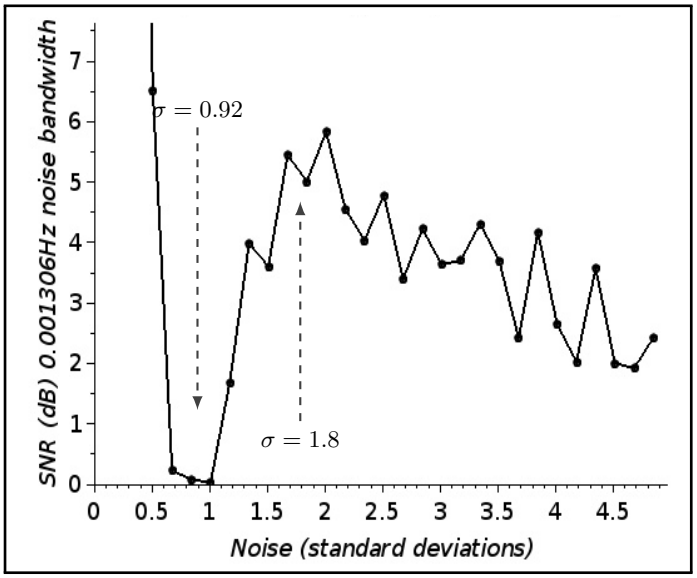

Figure 3.9: Output narrowband S/N variation with noise deviation. Normalised Langevin system $\alpha = \beta = 1.0$, frequency $f = 0.01045$, sine wave amplitude $A = 0.1$. The indicated noise deviation values; ($\sigma = 0.92$ and $\sigma = 1.8$) were used in generating the ROC curves of Figure 3.10.

pairwise comparison of the performance of the linear system at the two deviations shows worse detection performance at the higher input noise deviation $\sigma = 1.8$, which is expected. However the pairwise comparison of the performance with Langevin pre-processing shows the reversed situation. The ROC curve for the higher input noise deviation shows better detection performance over the $\sigma = 0.92$ case. However this counter-intuitive result should be expected from inspection of Figure 3.9 where the output S/N is highest at input $\sigma = 1.8$.

There is some asymmetry in the curve for the Langevin low input deviation case ($\sigma = 0.92$) but less than can be seen for the corresponding curve (Langvin, low input deviation) in the Gaussian-only noise used in the previous section in Figure 3.10. Without further investigation of the distributions at in the nonlinear region it is unsafe to draw any general conclusion linking the use of impulsive noise to a reduction in ROC curve asymmetry.

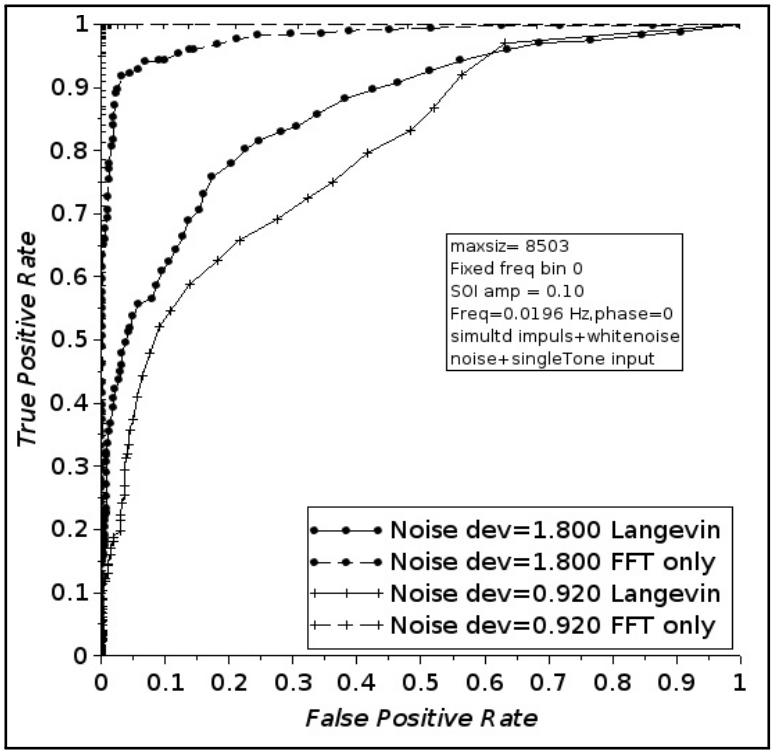

Figure 3.10: ROC Analysis. At two noise deviation values, FFT only (benchmark) ROC curves included for performance comparison. ROC curves generated using 500 realisations. Normalised Langevin system detection performance, and compared to the linear benchmark case (FFT only with no Langevin pre-processing). Low input S/N with sine wave amplitude $A_0 = 0.1 < A_c \approx 0.385$. Frequency of sine wave meets the Kramers rate condition ($f = 0.01045 << (1/2)\, k_r \approx 0.225$).

3.5.3 Harmonic input

By considering a noise free sinusoidal input the harmonic nature of the output from a nonlinear system operating at or near SR can be observed. Figure 3.11 demonstrates the nature of the time-series and spectrum of the output when operating at the SR peak and near the upper bound of the sub-threshold sine wave amplitude case.

Figure 3.11 motivates the possibility that a nonlinear system will respond to a general periodic signal consisting of a tone plus harmonics, i.e by acting as a better time-domain matched filter. A stochastic resonant pre-processor might provide improved detection performance for such harmonic signal mixtures. As a test of this idea a square wave was considered as an example of periodic input signal with a

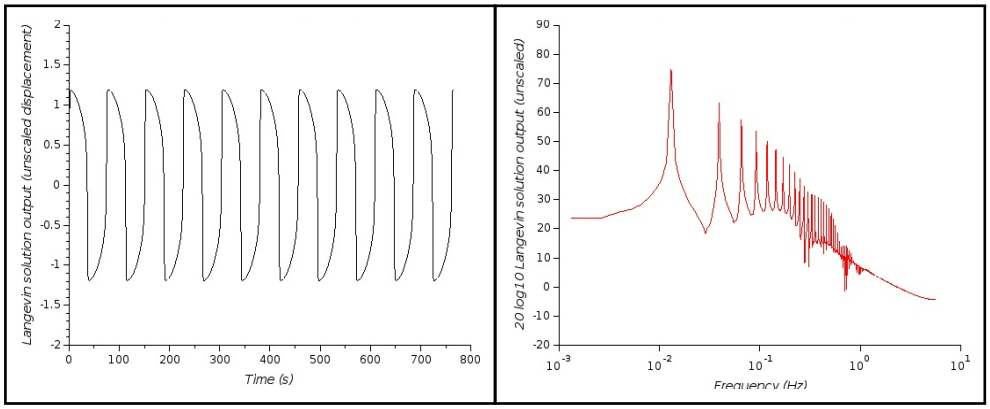

(a) (b)

Figure 3.11: Output from a Langevin system when driven by a sinusoid with no noise. (a) Periodic displacement time-series output from the system. (b) Unscaled power spectrum, the Fourier transform of the displacement time-series. The amplitude of this single forcing term is sub-threshold but large enough to cause periodic transition between energy minima.

harmonic set.

Harmonic input to a nonlinear system in the form of a square wave with additive noise has been investigated in two publications [108, 45]. Their focus was amplification and gain respectively, but not detection performance. Amplification of an input rectangular (square) wave without significant distortion of the waveform at the output has been studied in very restrictive circumstances [108]. In particular a relatively high S/N (high for signal detection problems). That a high S/N input square wave whose fundamental frequency has amplitude that is just sub-threshold, produces periodic transition should not be a surprise. The more relevant finding is that the addition of increasing noise distorts the output so that it no longer resembles a square wave.

Casado et al. [45] found that the inter-well and intra-well dwell time were independently variable and related to the shape of the energy function in the low energy minima, and the strength of both the noise and the signal. They further showed that under certain conditions a Langevin system driven by a square wave of duty cycle one, and white noise in a sub threshold SR configuration, gains greater the unity are possible. This appears to be consistent with previous results [108].

It may not be possible to easily improve detection performance by changing the filter matching prior to the simple binary threshold decision detector. It would be necessary to change from a Fourier transform (effectively this is sine wave replica matching) to a more complex filter using harmonics that adapts depending on the input S/N. However the nonlinear system may exhibit a different mix of harmonic amplitudes at the output if the *input* changes from sinusoidal to harmonic. The aim of this section therefore is to investigate the response of the nonlinear system to harmonic input, rather than consider harmonic filters to match the output of the nonlinear system.

Two sub-threshold amplitude cases are considered in this section; very low amplitude ($A << A_C$) and high input amplitude where $A \approx 0.7A_c$. A sinusoidal and square wave input were generated for both cases so that the behaviour of the system with square wave input could be compared to the sine wave case. A suitable square wave can be generated by using the odd harmonics of a chosen fundamental frequency sine wave. The peak amplitude of the fundamental and all odd harmonics in a square wave are given by Equation (3.7), where k is a positive integer that represents the fundamental and odd harmonics number, such that $k = \{1, 2, 3, ...\}$. The input signals (square or sine) were configured so that their respective peak excursions (overall amplitudes) were *different* in order that the amplitude of the fundamental frequency of the square wave was constrained to be identical to that of the sinusoidal input. This configuration compensates for the difference in amplitudes at the fundamental ($k = 1$) by a factor of $(4/\pi)$ encapsulated in Equation (3.7).

$$A_k = \left(\frac{4}{\pi}\right) . \frac{1}{(2k-1)} \tag{3.7}$$

The sine wave amplitude for the low input signal amplitude ($A << A_c$) was set as $A = 0.1$. The corresponding square wave amplitude required to maintain the same amplitude at the fundamental was therefore calculated and set as $A = 0.0785398$. At

the larger input signal case the two amplitudes were set as $A = 1.8$ and for the square wave as $A = 0.14137$. The frequency was set as $f = 0.0131$ and the normalised Langevin system configured by setting $\alpha = \beta = \delta = 1$. Plots of output S/N as a function of input noise deviation were generated from 30 averaged realisations. The square wave and the sine wave case for the low input are shown in Figure 3.12 and the high input amplitude case is shown in Figure 3.13.

In both amplitude cases it is clear there is no significant difference in the SR behaviour between sine or square wave input. Comparison of the square wave data with the sine wave data in each amplitude cases, shows good alignment of the two curves. The onset of the nonlinear region at $\sigma > 0.7$ is almost identical for pairwise curve comparison in the low amplitude case (Figure 3.12). It is also identical in the high input amplitude case but nonlinearity commences at lower deviation, $\sigma > 0.6$.

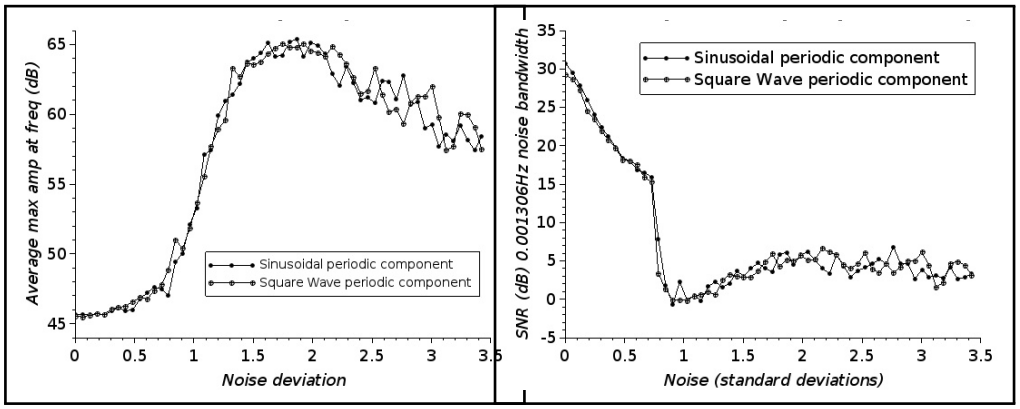

(a) (b)

Figure 3.12: Langevin system SR for two types of input periodic component, single sinusoidal tone and square-wave. Variation with additive noise deviation value, at fixed amplitude periodic component for the low amplitude input case ($A << A_c$). (a): Output amplitude variation with noise. (b): Output S/N variation with noise. Frequency 0.0131. Normalised Langevin system $\alpha = \beta = 1.0, \delta = 1.0$.

Three noise deviation values can be selected based on the configuration for SR shown in Figure 3.12, notably that the amplitude of the periodic component was set at $A = 0.10$ for the sine wave and $A = 0.0785398$ for the square wave. Recall the

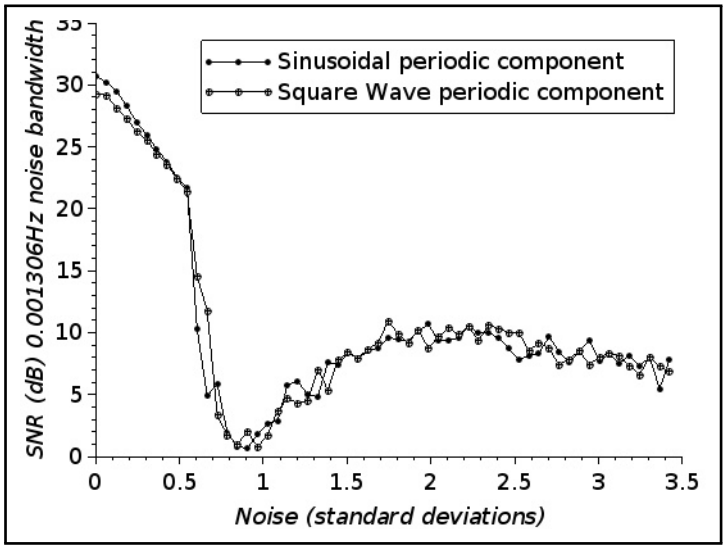

Figure 3.13: Langevin system SR for two types of input periodic component, single sinusoidal tone and square-wave. Variation of output S/N with additive noise deviation value, at fixed amplitude periodic component for the HIGH amplitude input case ($A \approx 0.7A_c$). Peak amplitude sine wave $A = 0.18$, peak amplitude of the square wave signal $A = 0.14137$. $Frequency 0.0131$. Normalised Langevin system $\alpha = \beta = 1.0, \delta = 1.0$.

threshold amplitude for a single (periodic) force term is $A_c = 0.385$ (for the normalised Langevin system used here), as outlined in Section 2.4.3 Equation (2.33). The detection performance is quantified by the calculation of ROC curves, for the case of the square wave this was measured using only the frequency bin corresponding to the fundamental frequency of the square wave. Statistical amplitude count data were not collected at the other harmonic frequencies. For the reasons described in Section 3.5.1 the lower input amplitude case was chosen for the comparison of detection performance by ROC analysis.

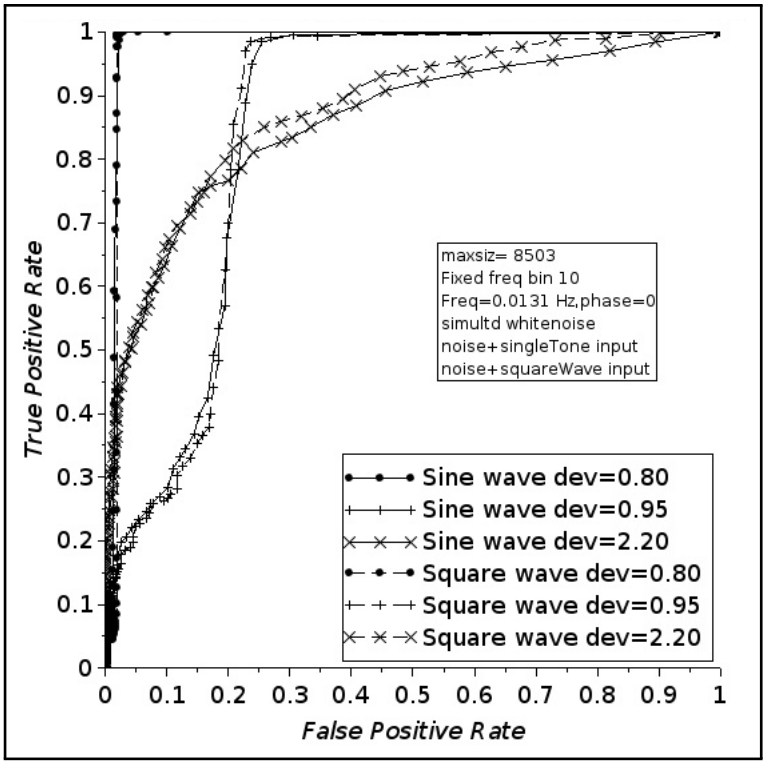

Figure 3.14: ROC curves: Comparing square wave input to sine wave input, both with white Gaussian noise. Analyses at three harmonic signal to additive noise power ratio's, corresponding to the three noise deviation values $\sigma = 0.8, 0.95, 2.2$. Input amplitudes correspond to the low amplitude case of Figure 3.12. Fundamental input frequency $f = 0.0131$, normalised Langevin: $\alpha = \beta = \delta = 1$.

Inspection of the ROC curves of Figure 3.14 shows no obvious difference in the detection performance for a square wave input compared to a sine wave input, at low input amplitude ($A << A_c$). The comparison holds at all three input noise deviation values considered; $\sigma = \{0.8, 0.95, 2.2\}$. In this comparison the amplitude of the square wave *fundamental frequency* is the same as the sine wave amplitude. The results show nothing that was not expected from the nonlinear system output S/N behaviour seen in Figures 3.13 and 3.12 (b).

The ROC curve for the minima in output S/N case ($\sigma = 0.95$), exhibits the same asymmetric form seen in Figure 3.7, suggesting that using a square wave input also results in a bimodal amplitude distribution.

The data presented in this section so far provides some evidence that additional energy input in the form of higher harmonics, does not alter the SR behaviour or detection performance as measured at the fundamental frequency. However, the second and third harmonics of a square wave have amplitudes one third and one fifth that of the fundamental respectively. It is possible the energy supplied by these higher harmonics is insufficient to have an effect. An input signal comprising of six equal amplitude harmonics, identical to the amplitude used in Figure 3.14, was also investigated. The six-harmonic test signal was configured to contain even as well as only the odd harmonics normally present in a square wave.

The ROC's for two input cases, sine wave or six equal amplitude harmonics, were computed at the SR peak corresponding to a noise deviation $\sigma = 2.2$ and are shown in Figure 3.15. The normalised Langevin system was used in both cases, the frequency was set at $f = 0.0131$ and the amplitude of the sine wave and also all six harmonics was set as $A = 0.10$. For the harmonic input the ROC analysis considered the amplitude in only the frequency bin corresponding to the fundamental frequency.

The detection performance measured for the two input signal types are very similar. There is no evidence in the ROC analysis for an effect on the amplitude of the

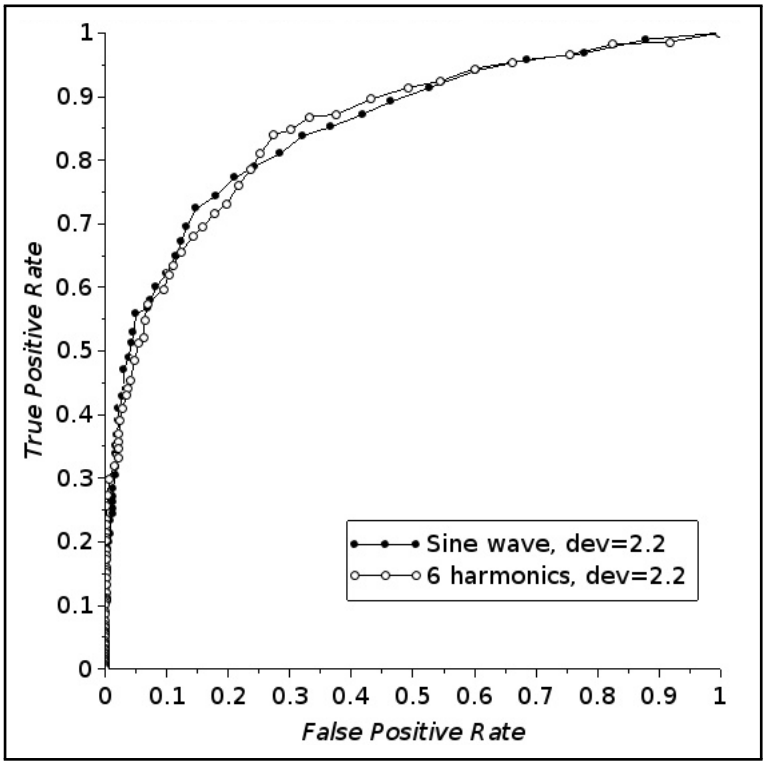

Figure 3.15: ROC curves: Harmonic input (six equi-amplitude harmonics) compared to single tone input. Analysis at SR peak corresponding to the noise deviation values $\sigma = 2.2$. Input amplitudes correspond to the low amplitude case of Figure 3.12, $A = 0.10$. Fundamental and sinusoidal input frequency $f = 0.0131$ Hz.

fundamental output tone at the SR peak, when higher harmonics of that frequency are added to the input tone. The tests presented in this section do not provide sufficient evidence that the nature of the stochastic resonant output at one frequency from a nonlinear system is affected by energy from elsewhere in the frequency spectrum.

3.6 Discussion

The signature increase in output S/N as the input S/N *decreases*, that marks the SR peak, has motivated the suggestion that SR may often provide an exploitable benefit when detecting weak signals. However no evidence was found that using a nonlinear system in this way generates any significant or useful enhancement in detection performance compared to conventional processing by the Fourier transform, for the

range of scenarios and system configurations examined. Even if increased performance had been demonstrated, configuring the nonlinear system to maintain the best level of performance over a usefully large proportion of configuration space (frequency, input S/N, etc) remains a problem because of the large number of inter-dependent system parameters that need configuring.

The chapter investigated some of the nonlinear system behaviours associated with SR. The counter-intuitive increase in output S/N for a decrease in input S/N is mirrored in the ROC analyses. Better detection performance is found at the SR peak where the input S/N is lower, compared to the performance measured at the minimum in output S/N in the nonlinear region, where the input S/N is higher. However, a conventional FFT always performs better in all the test scenarios investigated in this chapter.

The output S/N is never greater than the input S/N (at the identical noise bandwidth) for the sub-threshold configurations investigated. Figure 3.4 compares input and output S/N and highlights that rather than SR occurring as a peak in 'performance' it should more correctly be considered as a recovery back to a state that is very similar to linearity after a nonlinear region of reduced output S/N. When viewed in this way it is no longer surprising that ROC analyses carried out at SR (the peak in output S/N), shows that pre-processing using an SR system does not out-perform the linear detector (one without nonlinear SR pre-processing).

Most of the work in this chapter has used dimensionless nonlinear systems, and re-scaling factors for the system variables and parameters were found. By removing these re-scaling factors it is possible to build a practical a system that uses the mechanism of SR as a pre-processing stage prior to a detection stage, that is not constrained to detecting extremely low frequencies outside most practical use. However the dimensionless version of the system will capture the same behaviours as the same system that was not made dimensionless. Therefore no change in detection performance should be expected from the large parameter nonlinear SR system compared to its dimensionless form.

Harmonic input to a stochastic resonant system was investigated in order to explore whether additional energy in other parts of the frequency spectrum might alter the detection performance at the fundamental frequency of an input. The ROC analyses conducted at the fundamental frequency demonstrated no performance enhancement compared to the single tone input case. The interpretation that energy does not transfer between frequencies in a nonlinear stochastic resonant system is very tentative, given the narrow range of scenarios simulated.

Stochastic resonance can be considered as a recovery back to linearity from a region of extreme nonlinearity. But there are many other nonlinear behaviours that the same models (Duffing and Langevin) can exhibit. In the next chapter a different transition mechanism is considered for its potential to improve detection performance for weak signals. Specifically the transition from chaotic system dynamics to stable dynamics is investigated.

Chapter 4

Stable Limit Cycle Transition

4.1 Introduction, aims and outline

The nonlinear mechanism considered in the previous chapter was stochastic resonance which is initiated by forcing the system with sufficient noise to cause transition between stable potential energy minima separated by a barrier of higher energy. The transitions are made periodic by the presence of a second, periodic forcing term. The Duffing system can achieve another stable state quite distinct from the bistable configuration considered in the last chapter. At higher energy the system becomes chaotic, as input forcing energy becomes higher still the system can transition from chaotic instability to a stable energy state. This stable state is not a stable point but fixed trajectory in the system dynamics known as a limit cycle. This transition from chaos to a limit cycle was introduced in Chapter 2, and is the main focus of the investigation described in this chapter.

The Duffing nonlinear system model is arguably the most frequently investigated system in the context of nonlinear behaviours and also as part of a detector of weak signals. However, much less so in the context of underwater signal detection. The research reported here uses the Duffing model model to investigate the behaviours associated with the transition, and the impact on detection performance. The

transition mechanism has often been described as a 'detector' of weak signals, however the mechanism does not decide the presence of a signal it merely responds to it. Therefore to remain consistent with the terminology used in Chapter 3 the term pre-processor will continue to be used, but in this chapter it is applied to a nonlinear Duffing system configured for chaos-to-stable transition.

Some of the claims for the improvement in detection using nonlinear systems were reviewed in Chapter 2. In many cases the improvement is described only in qualitative terms. In some cases the signal-to-noise (S/N) metric is used as a measure of detection performance. Only in one or two cases is ROC analysis used, and only for the simplest input signal case of a sine wave with added Gaussian noise. The main aim of this chapter is to measure detection performance with the nonlinear pre-processor in place, for a range of input signal cases, using ROC analysis as the most robust metric.

4.2 Methods

The behaviours of a nonlinear system are controlled by the parameters of the system. The parameters of a system model such as the Duffing equation can be a constant multiplier on the individual additive components and variables. More complicated behaviour can be generated by changing the parameters to be time dependent or dependent on the existing variable. Surveying changes of state in parameter space is therefore a useful means of visualising the dependence of behaviour on model configuration. Scaler parameter space does not say anything about how the state of the system varies with time. A common method of visualising the system state variation in time is phase space [90, 84]. Both methods of revealing system behaviours are used in this chapter.

The detection performance of a conventionally optimal detector increases as the data length of a stationary signal in Gaussian noise increases. Prior work [20] has

suggested this is not true for the stochastic resonance detection mechanism in the Duffing system. One of the aims in the current chapter is to discover whether this assertion of constant detection performance is also true for the transition mechanism. Using a nonlinear transition technique to detect signals, and assuming constant detection performance with input data length, suggests the potential for an increasingly favourable comparison with a conventional optimal matched filter for shorter data input lengths.

4.2.1 The Duffing model

The Duffing system will be used throughout this chapter as the basis for investigating the chaos-to-stable transition. Most of the relevant prior work that considers this transition, which was introduced in Chapter 2, uses the Duffing model. The initial definition of the model was also introduced in Chapter 2, with a specific implementation re-defined for use in the SR investigations in the previous chapter (Section 3.3.1). The version used in this chapter differs from that used in the previous chapter because here three driving terms will be used, two periodic and one stochastic. The first periodic drive term is referred to as the internal drive term, the other two terms represent the input signal as an additive combination of noise and periodic terms. The system is described below, with the full definition used in this chapter shown as Equation (4.1).

$$\begin{aligned} \ddot{x} + \delta\dot{x} - \alpha x + \beta x^3 &= \gamma\cos\left(2\pi f_0 t + \phi_0\right) + F_i\left(t\right) \\ \ddot{x} + \delta\dot{x} - \alpha x + \beta x^3 &= \gamma\cos\left(2\pi f_0 t + \phi_0\right) + A\cos\left(2\pi f t + \phi_i\right) + n\left(t\right) \end{aligned} \tag{4.1}$$

where:-

$\gamma\cos\left(2\pi f_0 t + \phi_0\right)$ = Configurable periodic force term, internal to the system

and:-

$$F_i = A\cos\left(2\pi f t + \phi_i\right) + n\left(t\right)$$

$$\left.\begin{array}{ll} A\cos\left(2\pi f t + \phi_i\right) & = \text{Input signal: periodic component} \\ n\left(t\right) & = \text{Input signal: noise component} \end{array}\right\} \tag{4.2}$$

The input periodic force term amplitude A can take any value however there is a minimum value that is just sufficient to cause transition to the limit cycle, A_m. This is discussed in detail in Section 4.2.3 below. Note that the form of the homogeneous part of the Duffing system used here, differs from the original definition, by a change of sign of the linear stiffness force term αx. The original form published by Georg Duffing in 1918 (Original in German, referenced in [91, 37]), and the form used here, are shown together below for ease of comparison (with only one force term for simplicity).

$$\ddot{x} + \delta\dot{x} + \alpha x + \beta x^3 = \gamma\cos\left(2\pi f t\right) \qquad \text{Duffing's original}$$

$$\ddot{x} + \delta\dot{x} - \alpha x + \beta x^3 = \gamma\cos\left(2\pi f t\right)$$

The consensus in published work that considers the original form of the Duffing equation designates it as a 'hardening' system when the linear and nonlinear stiffness scalers are set as $\alpha > 0$ and $\beta > 0$, and as a 'softening' system when $\alpha > 0$ but $\beta < 0$ [39](chapter 5) and [91, 109, 110]. To date no publications considering the form of the Duffing used here where α is negative, have been found describing that form of the system as either hardening ($\alpha < 0\ ,\ \beta > 0$) or softening ($\alpha < 0\ ,\ \beta < 0$)

To make a pre-processor using the Duffing system requires a method of solving the Equation (4.2) over time. However, the solver method chosen must be flexible enough to allow parameter modification and also the input of both real and simulated discrete input data (represented by the F_i forcing terms). This means the implemented numerical solver must manage input sets of discrete real-signal samples,

at the same time as data generated using the signal generation function libraries.

A suitable and comprehensive analytic solution to the Duffing equation is also not available, however restricted scope solutions are possible. Local linearisation techniques based on a Taylor expansion and taking the Jacobian of the system (Lyapunov's First Method; see Chapter 6 [111]) can provide analytic solutions over a very small region about selected fixed points. Other methods based on a Volterra series expansion [112, 110] and the Laplace Decomposition Algorithm [113], have also been studied. The work reported in this chapter therefore uses a specially written numerical solver, which implements the 'classic' or 'original' four stage fixed step Runge-Kutta numerical method (RK4). The RK4 numerical solver algorithm adopted for this thesis is described in Appendix A. The RK4 method is used extensively for solving nonlinear systems such as the Langevin, Lorenz and the Duffing systems. The method implemented in this chapter solves a first order coupled system version of Equation (4.2) producing the state space solution $(x, \dot{x})$. The RK4 method was implemented in Scilab, which is an open source numerical computation tool similar to Matlab, and was used for all the numerical modelling in this thesis. Scilab is designed to operate to a precision of $\eta = 2.22 \times 10^{-16}$, which can be confirmed by evoking a built in Scilab diagnostic function [114]. This generates an error of approximately $\sim \frac{\eta}{h} + h^q$ [115] where $q = 4$ the RK4 order, typically $0.00001 < h < 0.0001$ the time step size. The maximum error is approximately $\sim 2 \times 10^{-11}$. A fixed step fourth order RK4 numerical solver was found to be easy to implement in the flexible form required.

The Duffing system implemented for the work reported here was re-cast in a frequency normalised form, as discussed in Chapter 2 Section 2.3.3, and as derived in Appendix A. Note that this frequency normalisation method does not remove any divergence problems *inherent* to nonlinear systems solved using numerical methods. However, this scheme significantly reduces RK4 numerical solution divergence problems found during validation tests of the RK4 solver implementations of both a non-normalised and a frequency normalised Duffing system. Normalisation fixes the system parameter

values for a given desired state no matter what the force frequency is.

4.2.2 The transition mechanism

To demonstrate the mechanism of transition the system of Equation (4.1) was configured in the same way as previous researchers [4]. The parameter values are summarised in Table 4.1. Wang et al. [4] described the existence of a critical value for the amplitude of the internal force term, denoted γ_c. In the absence of the input force terms F_i in Equation (4.1), the critical internal amplitude value is that nominally maximum internal force amplitude value that places the Duffing system in a state just inside a chaotic regime such that a small additional force will cause the system to transition to a periodic stable state. The additional force is assumed to be provided by the input signal F_i comprising a sine wave and a noise term. The existence of a critical internal force amplitude implies the additional (input) force terms must have an amplitude large enough to cause transition to the limit cycle. The input signal therefore provides the small but finite sized amount of *additional* energy required to attain the limit cycle. Clearly all the parameters of Equation (4.1) are open to variation, however the parameter values shown in Table 4.1 are the baseline set used throughout this chapter except where stated otherwise. The effect of different parameter value choices is discussed later.

Parameter	Symbol	Value
critical internal force term amplitude	γ_c	0.812
damping factor	δ	0.5
linear factor	α	1
nonlinear term factor	β	1
phase difference	ϕ	0
initial conditions	$(x_0, \dot{x}_0)$	$(0, 0)$
sinusoidal input minimum amplitude	A_m	0.0201

Table 4.1: Baseline Duffing parameter values for chaos to stable limit cycle transition. Phase ϕ is the simulated phase difference between the input tone $A\cos(2\pi ft)$ and the internal force term $\gamma\cos(2\pi f_0 t)$. A RK4 constant step size of $h = 0.0000204$ is used, unless otherwise stated.

In order to configure the Duffing system as a pre-processor based on the chaos-to-stable transition it is necessary to first find the critical value γ_c. To do this the Duffing system is configured with only the internal force term, the input amplitude is set to zero $F_i = 0$. The internal force term amplitude value γ is then selected on the basis of a series of trial numerical solution runs to find the lowest value to three decimal places that causes a stable transition to the limit cycle (as observed in a phase space plot). The internal force amplitude is then reduced slightly and set at this lower amplitude (typically 0.002 lower). The resulting amplitude value is termed the critical amplitude value γ_c and has a value broadly in agreement with the value reported in Wang et al. [4] (where the value was set as $\gamma_c = 0.815$ for an RK4 step size of $h = 0.004$). This procedure need only be performed once prior to any type of data collection run carried out and described in this thesis. The Duffing system is now considered poised in a chaotic state close to a transition to stability. More sophisticated methods of selecting γ_c have been sought by others [89], however the trial run method described above is considered sufficiently rigorous and is used throughout this thesis. The selection of γ_c is discussed in more detail in Section 4.2.3.

Once the static value for the critical internal force amplitude γ_c has been found by the procedure outlined above, the same method can be used to establish the existence of a minimum periodic input force term amplitude A_m that causes transition. This approach established the value of A_m in Table 4.1.

The phases of the controllable internal periodic force and the input signal is represented in Equation (4.1) by the two terms ϕ_0 and ϕ_i. It is sufficient to consider only the difference between the two phases. The phase difference is represented as simply $\phi = \phi_0 - \phi_i$. The phase difference is set to $\phi = 0$ by setting $\phi_i = \phi_0 = 0$, for all the investigations in this chapter, unless otherwise stated. During investigations later in this thesis, where real input signals are used and where the phase is not known, the internal force phase value (ϕ_0) is set to zero. The impact of an unknown but finite phase difference where real data is involved, is discussed and investigated throughout

Selecting the system parameter values that are the most appropriate for each pre-processing task, based on a more formal approach, would be a line of further research, however the development of methods and algorithms for this purpose is not the focus of this chapter. Suitable values are here found by trial and error. This method was found to be sufficient because it results in stable parameter values.

Figure 4.1 illustrates the system performance obtained when selecting the frequency of the input and the internal forcing terms to be the same, ($f_0 = f$) with zero phase difference ($\phi_0 - \phi_i$), signal amplitude set to the minimum $A = A_m = 0.0201$, no added noise ($n(t) = 0$) and a RK4 step size $h = 0.00004$. The sample rate was set to 2000 Hz, and 4000 simulation input points were used to generate the data.

The RK4 solution of Equation (4.1) generates time-series output for both the displacement (x) and its derivative (velocity). These are used to plot phase space, which visualises the time evolution of the system state defined by its displacement and velocity. The time evolving state is a connected (continuous) trajectory of state points and not simply an incoherent random scatter plot of system states. The main features and behaviours are seen in the four plots of Figure 4.1. Plot (b) shows the system transitioned to the stable limit cycle. The short initial trajectory that smoothly connects the initial point $(0, 0)$ to the limit cycle is the initial or start-up transient. The fundamental frequency and four additional harmonics are visible in both spectra (c) and (d) however the noise energy at all other frequencies significantly reduces when the system has stabilised. At the same time the energy in the sine wave component of the input drive has increase by approximately 3.4dB. This increase is far greater than the simple addition of a second sine wave drive at the same phase and frequency, of amplitude $A = 0.0201$.

The main features shown shown in Figure 4.1 such as stable and chaotic motion in phase space, nature of the spectrum and importantly the amplitude change at the 80

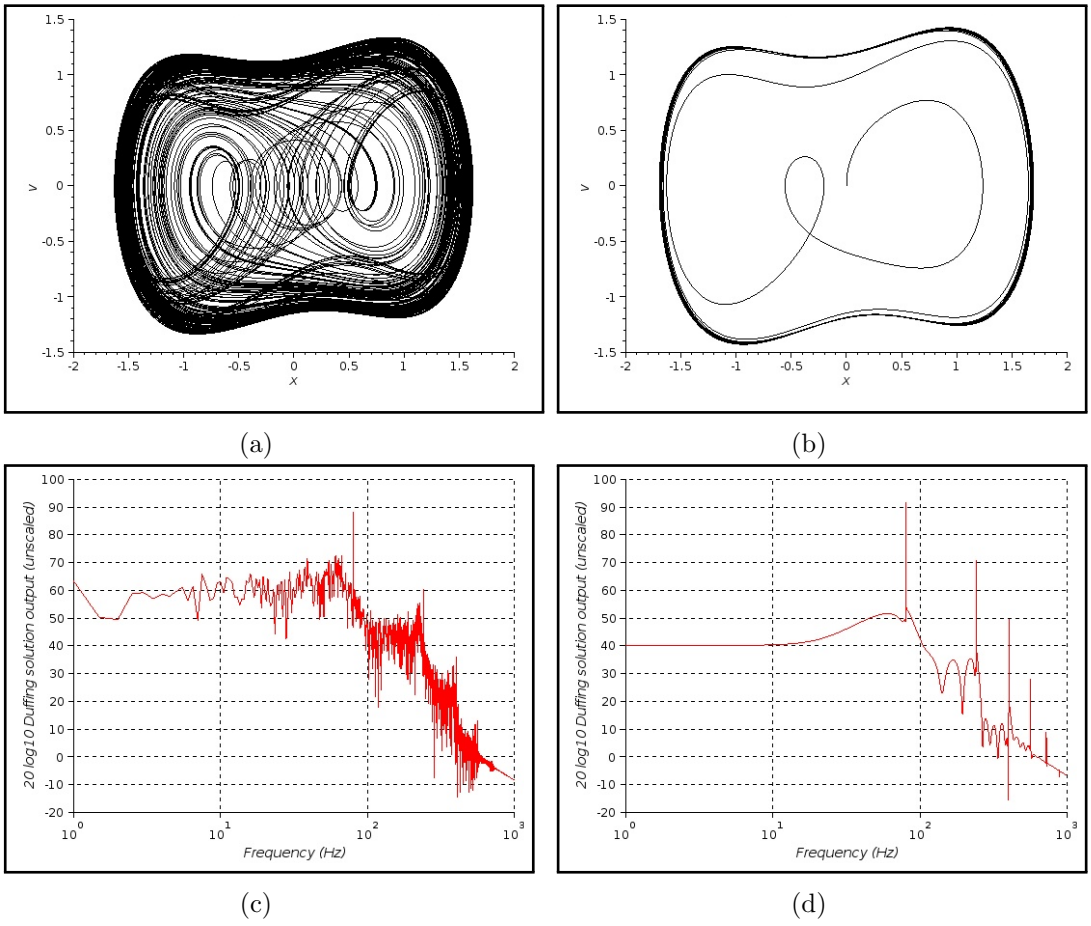

Figure 4.1: The Duffing pre-processor output illustrating transition. (a): Phase space with internal drive only. System in chaos. Drive amplitude at critical value, $\gamma_c = 0.812$. (b): Phase space after transition. Two drives, $\gamma_c = 0.812$ and $A = A_m = 0.0201$. (c): Non-normalised and non-corrected power spectrum of Duffing displacement (x) output for one (internal) drive. System in chaotic state prior to transition, drive amplitude $\gamma_c = 0.812$ and $A = 0$. (d): Output power spectrum with two drives, system is in a stable state. $\gamma_c = 0.812$ and $A = A_m = 0.0201$. Frequency is set to 80 Hz. All other configuration as shown in Table 4.1.

Hz peak, will be discussed and re-visited repeatedly in the rest of this chapter. The first feature discussed in some detail in Section 4.6 is the short start-up transient trajectory seen in the phase space plot. The initiating state for the Duffing numerical solver was $(x_0 = 0, \dot{x}_0 = 0)$, from this point the trajectory clearly takes a finite time to converge to the stable limit cycle.

4.2.3 Minimum signal to trigger transition

The existence of an 'internal' periodic force of critical amplitude γ_c, that places the system in the chaos regime so that an additive finite sized amplitude input force causes transition, directly implies the existence of a minimum detectable input force amplitude. Several of the publications referenced in Chapter 2 use a single value for γ_c in their work [4, 5, 8], but it would be incorrect to suppose there is only one correct value and none of the other 'nearby' amplitude values can be considered as critical. The situation can be clarified by a simple input/output nonlinearity test using the Duffing model of Equation (4.1). The model was configured without the additive noise $n(t)$ or sine wave $(A\cos(2\pi ft))$, leaving only the 'internal' drive term $\gamma\cos(2\pi f_0 t)$ input terms.

To find the critical drive amplitude the amplitude of the output displacement x with varying drive amplitude γ was investigated, the results are presented in Figure 4.2. The variation is clearly nonlinear, the plateau region at drive amplitudes greater than 0.825 corresponds to the stable limit cycle (as indicated in phase space, for example see Figure 4.1 (b)). The 'cliff face' at drive amplitudes $0.800 \leqslant \gamma \leqslant 0.825$ represents the *range* of critical drive amplitude values suitable for setting to system to be close to stability. The upper bound on the range of suitable values is determined by the need to keep the system chaotic. The lower bound on the range of values is arbitrary, but that the larger the value of γ_c chosen, the smaller the amplitude of the sine wave component of the input signal can be and still cause a transition.

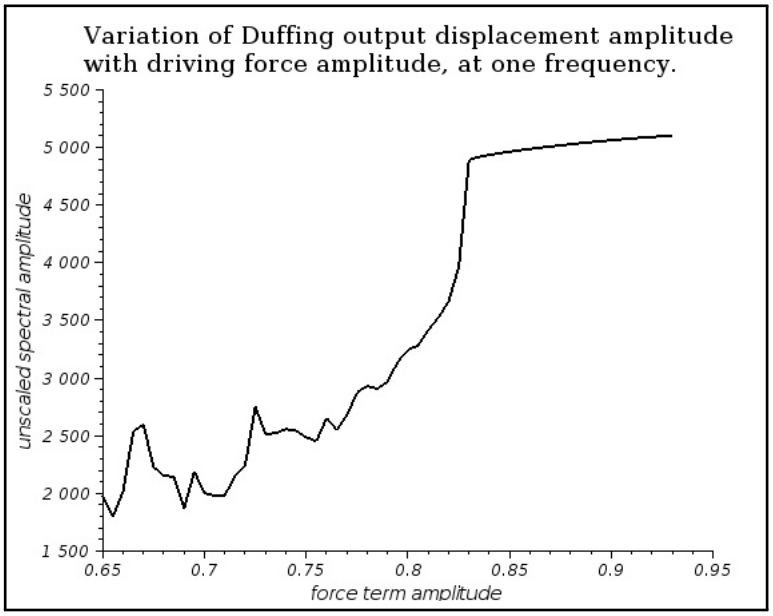

Figure 4.2: Finding an appropriate value for the critical drive amplitude, γ_c. Drive frequency is arbitrarily chosen but tuned to be centred in a frequency bin in the FFT spectrum, frequency = 501.17 Hz. No noise and only one sinusoidal drive term (A set to zero)

Figure 4.2 shows there is a minimum value for the internal drive amplitude (or equivalently; internal amplitude combined with input drive amplitude) that will cause the transition. Previous research ([4, 96, 7]) describes the internal system force term amplitude γ_c as a *critical* amplitude to indicate the system is poised just prior to transition to stability. However it is the total additive amplitudes of all in phase forcing terms that can be considered a threshold or critical amplitude, above which the system is fully stable (and this occurs at a value of $\gamma = 0.831$ in Figure 4.2). The value of internal force amplitude γ that holds the system near stability but still in chaos, could be selected from any value between approximately $\gamma_c \approx 0.81$ to 0.83. In this thesis γ_c will continue to be used as to indicate the system poised in this state, and for consistency it with previous research γ_c will continue to be called the critical (internal force) amplitude.

The results of Figure 4.2 were obtained using a single periodic force term with variable amplitude γ. It is trivial to demonstrate that the coherent addition of two

force terms of the same period would generate the same result, where the the stable plateau region once again occurs when the amplitude exceeds about 0.823. However in this case it is when the summed force amplitudes exceed the value such that $\gamma + A > 0.82$. Selecting a critical value for the internal force amplitude $\gamma_c \approx 0.81$ to 0.83 will therefore require a small but finite minimum amplitude A_m to trigger full transition to the stable limit cycle. Further increases in the value of A will generate increased output. However the changes are small compared to the nonlinear change in output amplitude over the transition region (which is the region where force term amplitudes range from ~ 0.81 to ~ 0.83 in Figure 4.2). Configuring the Duffing system to respond by transitioning to stability in the presence of an input sine wave of the right frequency and of sufficient minimum amplitude A_m will form the basis of a pre-processing stage aimed at improving detection performance.

4.3 Additional system behaviours

In order to fully control the Duffing system and its impact as a pre-processor in detection performance it is necessary to describe and understand two distinct behaviours common to many nonlinear systems. The first behaviour is associated with the chaos-to-stable limit cycle transition. With the drive amplitude of a sine wave forcing term fixed at a value sufficiently high for stable limit cycle dynamics, the system output will nearly always start with a short transient period of unstable motion before settling at the limit cycle. The second behaviour is associated with the form of the nonlinear system used in this investigation where two of the three force terms are periodic, one representing an 'internal' configuration force ($\gamma_c \cos(2\pi f_0 t + \phi_0)$) and the second representing an input sine wave ($A \cos(2\pi f t + \phi_i)$). The two periodic terms must necessarily be close in phase and frequency in order that the system will transition fully.

4.3.1 Transients and initial conditions

The numerical solver used in the work reported here is initiated with two starting values for the paired first order system, $(x_0, \dot{x}_0)$. Selecting the optimal initial conditions is driven by consideration of numerical solution stability and accuracy, managing potentially unwanted behaviour and improving detection performance. The Duffing system forced periodically with sufficient amplitude to cause transition will generally first exhibit chaotic behaviour that persists for a short time before the system converges to the stable limit cycle. The right side phase space plot of Figure 4.1 shows an example of an initial transient initiating from $(x_0 = 0, \dot{x}_0 = 0)$, in this case a chaotic transient. A method of predicting the lifetime of the initial chaotic transient was developed in the mid 1980's [116], specifically for two dimensional flows. The authors assert the same methods can also be applied to three-dimensional time-continuous systems such as Duffing, and their method centres on predicting the value of the *critical exponent* ζ of Equation (4.3).

$$\tau \sim (p - p_c)^{-\zeta}, \quad \text{subject to } p > p_c \tag{4.3}$$

τ is the transient time, p is a parameter of the system (typically, forcing amplitude), p_c is a threshold value at which the strange attractor disappears. The system remains in chaos while $p > p_c$ and until the trajectory becomes captured by another attractor.

The specific transition from chaos to stable motion at the limit cycle motion exhibited in Duffing caused by a sufficiently large force amplitude can be interpreted in the same way. For a fixed input sine wave amplitude ($A + \gamma_c$ for in-phase periodic forces) the system output amplitude does not instantaneously achieve the maximum expected while in stable motion. The output amplitude begins to grow, form the initial starting condition of $(x_0 = 0, \dot{x_0} = 0)$. During this initial period the system is in a state of chaos even though the input amplitude is sufficient to cause stable motion. Eventually the trajectory touches a second unstable fixed point (in Duffing at

$(\dot{x}, x) = (0, 0)$). This event is termed *crisis* (specifically, one type of crisis) and at this point the chaotic attractor is destroyed [117, 116]. However, the trajectory *will continue to move chaotically while it is very close to the original site of the now destroyed chaotic attractor.* At some (average) finite time τ later the trajectory has moved away from the old chaotic attractor site and becomes captured by the stable (limit cycle) attractor. The trajectory remains within the basin of the new stable attractor. In the absence of any further system parameter changes, the subsequent motion constitutes the periodic stable long term behaviour of the Duffing system because the strange attractor no longer exists to revert it to chaos. The short period of chaotic motion before full capture by the limit cycle and in the *absence of the original strange attractor* of average time length τ, is termed *transient chaos.*

The dependence of transient time on the combined amplitudes of the input for the system of Equation (4.1) but without the noise term $n(t)$, was investigated as follows. The investigation is comprised of a series of measurements over 80 realisations of the configuration, varying the initial start point between realisations. At completion the transient times for all 80 iterations are averaged, then the sine wave amplitude is incremented and the measurement process repeated. The Duffing system was configured at critical drive amplitude $\gamma_c = 0.812$ with the sine wave amplitude set to an initial value of $A = A_m = 0.02$. Initial conditions selected randomly from anywhere on or within the area enclosed by the stable limit cycle, or if from outside the limit cycle very close to it (see Figure 4.1 for an example of a stable limit cycle). The random selection of initial conditions was uniformly distributed. The result is shown in Figure 4.3.

The Duffing system results shown in Figure 4.3 are qualitatively consistent with earlier results found for the Henon map [116]. As the overall forcing amplitude $(\gamma + A)$ is increased the average time length of the initial chaotic transient reduces.

Each time the transition is triggered by the appropriate input, a chaotic transient will

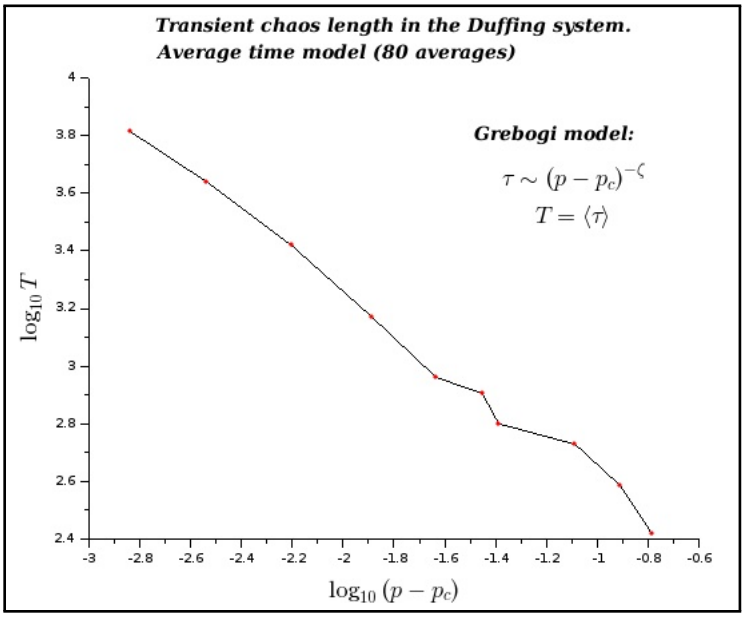

Figure 4.3: Measured transient time in the single Duffing system (according to the Grebogi model [116]). System forced periodically with increasing amplitude (the parameter p) over the critical amplitude for stable dynamics, $p_c = \gamma_c$. Average transient time length T_τ at each p increment is here measured as the number of unscaled points in the initial transient, for random initial conditions.

nearly always be present, and its length remains fixed even if the input signal length (and therefore the Duffing output) is shortened. The performance of a binary detection based on a simple threshold applied to the chosen variable (for example, spectral component or correlation value) will degrade as the incoherent and reduced average amplitude chaotic transient length increases as a proportion of the total Duffing output data length. It was therefore desirable to find strategies to ether keep the chaotic transient as short as possible, or eliminate it altogether.

It is important to note that τ is an average time, and the results shown above were obtained using randomised initial conditions. It is possible to reduce the transient time to zero by selecting initial conditions that lay on the stable limit cycle very close to the point $x_0 = 0$ and $\dot{x_0}$ positive. This initial condition is stable in the sense that transient time is always zero when the system is configured with these initial conditions. The result is not as attractive as it may seem because the required (positive) value of $\dot{x_0}$ in a practical detection scheme with Duffing transition

pre-processing, may not always be easy to determine. In order to maintain consistency most of the investigations in the rest of this chapter will use initial conditions of $(x_0 = 0, \dot{x_0} = 0)$ unless otherwise stated. In cases where the transient impacts or potentially degrades measurements the transient section is discarded.

4.3.2 Intermittent chaos

The frequency of a real (but unknown) input signal will not necessarily match the internal drive frequency of the Duffing system, these are f and f_0 of Equation (4.1) respectively. The output of the Duffing system, where there is a difference in frequency between the two force terms (ignoring the noise term for now) is characterised by cycling between a period of stable oscillations followed by a period of chaos. The regularity of the behaviour is illustrated in Figure 4.4 (a), however this was only achieved by using zero noise input and the sinusoidal input having an amplitude at least double the minimum necessary to trigger transition. Intermittency rapidly becomes irregular as the signal amplitude is decreased, plot (b) illustrates the behaviour with input amplitude set to the minimum necessary to cause transition. The regularity deteriorates further as noise is introduced into the input.

Intermittent chaos serves to reduce the proportion of time spent in a stable configuration. However if the period of intermittency is very low (i.e. the two frequencies are very close) the required length of data output from a practical Duffing pre-processor sufficient to make a detection may be shorter than half of one intermittent chaos cycle. In other words the next period of chaos is beyond the useful data length and therefore cannot degrade detection performance. By shortening the Duffing output (or equivalently the input) it is therefore possible to widen the *effective* bandwidth of a single Duffing pre-processor, without the need for prior knowledge of the input signal. In some applications and Duffing configurations the effective bandwidth may be wider than has been previously reported [4]. It is noted here, but not investigated, that detecting the *difference* frequency may provide a

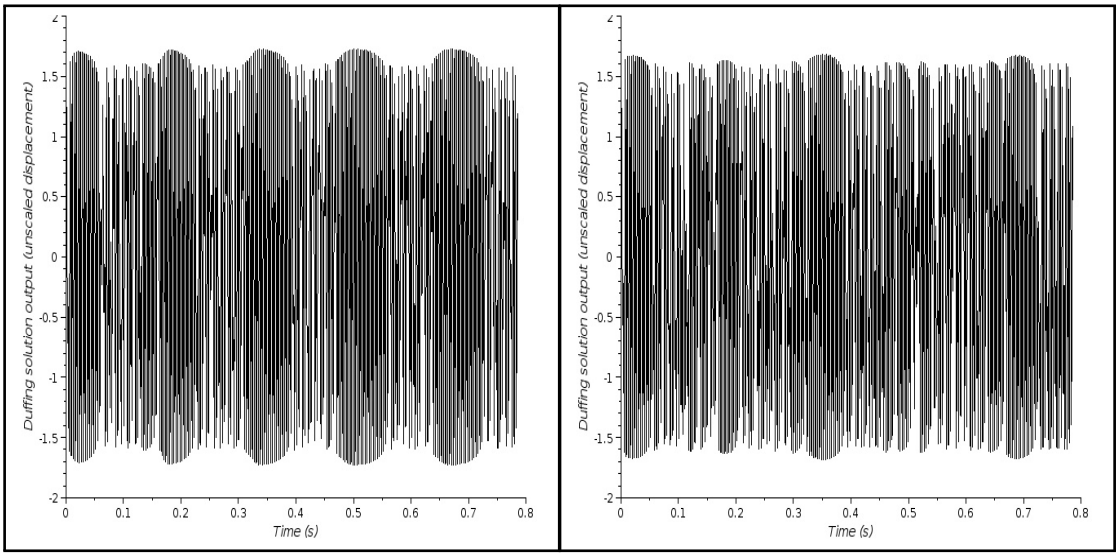

(a) (b)

Figure 4.4: Intermittent chaos at high, and minimum, input amplitude. In this example $f_0 = 280$ Hz and $f = 286$ Hz. Duffing configured with the baseline values of Table 4.1 with the following changes. (a) input sine wave amplitude fixed at $A = 2A_m = 0.0402$. (b) uses $A_m = 0.0201$. Noise deviation is zero and the internal drive amplitude set to critical as $\gamma_c = 0.812$.

means of adaptive tuning or frequency locking for a single Duffing pre-processor.

4.3.3 Bandwidth

The presence of intermittent chaos within the time window of data output from the nonlinear system is illustrated in Figure 4.4. The time-series data plotted in the figure reveals the amplitude of the periodic components to be larger than the interleaved unstable chaotic sections. The difference is not large but the figure does illustrate some apparent dependence on how the input sine wave amplitude impacts the size of the beat-frequency envelope. If nothing were known of the input signal, observing the presence of intermittency would indicate the probable presence of a sine wave at the input, that had an amplitude at least $A \geqslant A_m$ and that was close in frequency to the internal force term. It can be observed from the figure, that if the input time length were, for example, about 0.12 seconds in length then one whole periodic section and one whole chaotic section would be passed to the detection stage.

The overall amplitude seen by the detector would be less than if the whole 0.12 seconds had been fully periodic. It would depend on the detector type to know by how much the detected amplitude is degraded by the section of lower amplitude chaos. It is safe to assert therefore that if two whole sections of periodic behaviour and one of chaos, were present in the time window of data passed to the detector, then the amplitude would now be higher. However it would not attain the same overall amplitude seen for a continuous periodic output for the whole time window. As the difference between internal drive frequency and the input sine wave frequency grows larger more and more of each type of intermittent chaos packs into the time window, analogous to the closing of a concertina bellows. We can therefore hypothesise that as the difference frequency grow, the overall amplitude cycles up and down converging to some value lower than the maximum that would be observed for full periodic motion within the time window. The measured value of the output from a detector, which could be amplitude or some other related parameter, can be used to measure the bandwidth of a single Duffing system. This analysis is carried out in the next chapter in Section 5.5.

4.4 Varying the Duffing parameters

The basic transition mechanism and the main conditions required to initiate it have been introduced in the previous section. This section describes some additional behaviours that contribute to an understanding of why the mechanism occurs and what are the potentially exploitable properties that can be used to enable an improvement in the performance of the detector stage. The behaviours are revealed by simplifying the Duffing system to use a single internal periodic drive force of amplitude γ, and then performing a limited pairwise parameter space examination of the parameters; damping δ, linear coupler α, nonlinear coupler β and drive amplitude γ.

4.4.1 Parameter space configurations

The Duffing system defined in Equation (4.1) is configured by a linear scaling parameter applied to each term, (the two terms representing an additive input signal $A\cos(2\pi ft)$ and $n(t)$, have been ignored in the investigation of parameter space discussed in this section). All of the previously published work referenced in this thesis (see for example: [4]), that investigates specifically the Duffing system as a detector of weak signals, use system configuration values at or very close to those shown as the baseline set in Table 4.1. It is useful to investigate a range of values for all of these configuration parameters to find a set that enables a better detection performance compared to the baseline values.

Four of the scaling parameters are key in configuring the system to exhibit chaotic, nonlinear or stable behaviours and some have been discussed earlier. The investigation in this section will concentrate on the following four parameters;

- The damping factor applied to the velocity term, δ
- The factor applied to the linear displacement term x, α
- The factor applied to the nonlinear displacement term x^3, β
- The amplitude factor applied to the internal drive term, γ

The parameter space investigation was carried out by fixing two parameters at their baseline values (see Table 4.1), and varying the other two. The investigation was limited to following four combinations from this basic scheme;

a) Vary drive amplitude and damping (γ and δ), fix linear and nonlinear couplers (α and β)

b) Vary γ and β, fix α and δ

c) Vary γ and α, fix β and δ

d) Vary β and α, fix γ and δ

In each combination the numerical solver was nest-iterated typically 80 times for the two varying parameters. The displacement x from the Duffing system was

transformed using an FFT to enable easier peak value picking at the test frequency, which was fixed at $f = 489.92$Hz for all simulations. All the Duffing configuration values for the parameter space investigation are summarised in Table 4.2. The results are plotted as greyscale plots with the two independently varying parameters on the first two axes and the output amplitude as the dependent variable forming the greyscale surface. The results are discussed in separate sections below; Section 4.4.2 discusses combinations a) and b), and Section 4.4.3 discusses c) and d).

Parameter or other system constant	Symbol or name	Fixed value	As a variable range	figure
Critical forcing term amplitude	γ_c	0.812	$0.3 \leqslant \gamma_c \leqslant 1.3$	4.5, 4.6, 4.7
Damping factor	δ	0.5	$0.25 \leqslant \delta \leqslant 1.05$	4.5
linear coupling factor	α	1	$0.4 \leqslant \alpha \leqslant 1.2$	4.7, 4.8
nonlinear term coupling factor	β	1	$0.4 \leqslant \beta \leqslant 1.2$	4.6, 4.8
phase difference	ϕ	0		
number of data points	*maxsiz*	2000		
Force frequency	$2\pi f_0$	489.92		
Input tone amplitude	A	0		
RK4 constant step size	h	0.00002		
Noise $n(t)$ variance	σ	0		

Table 4.2: Duffing parameter values used in the model, for the damping/force amplitude parameter space investigation. The force frequency is chosen to be frequency bin centred in the spectral transform of the output displacement data.

4.4.2 Varying the drive/damping and drive/nonlinear coupler

Figure 4.5 shows the results of the drive amplitude/damping parameter space investigation. The main features align diagonally from lower left to upper right, with the high output amplitude regions towards the upper left. There are two distinct high amplitude regions separated by clear line from $(\delta = 0.25, \gamma = 0.8)$ to $(\delta = 0.72, \gamma = 1.28)$. Both regions represent a Duffing system that has transitioned to a stable state. The isolated elongated high amplitude islands are the result of other

stable trajectories in the system dynamics. However they are distinct from the main limit cycle considered in this chapter because they generate a more complex set of frequencies. Their pathways in phase space exhibit a variety of *crossing* trajectories which result in additional frequencies higher and lower than the drive frequency and its harmonics. The original benchmark values of damping and critical internal drive amplitude ($\delta = 0.5$ and $\gamma_c = 0.812$) for configuring the Duffing system to in chaos but just before transition, can now be seen in context.

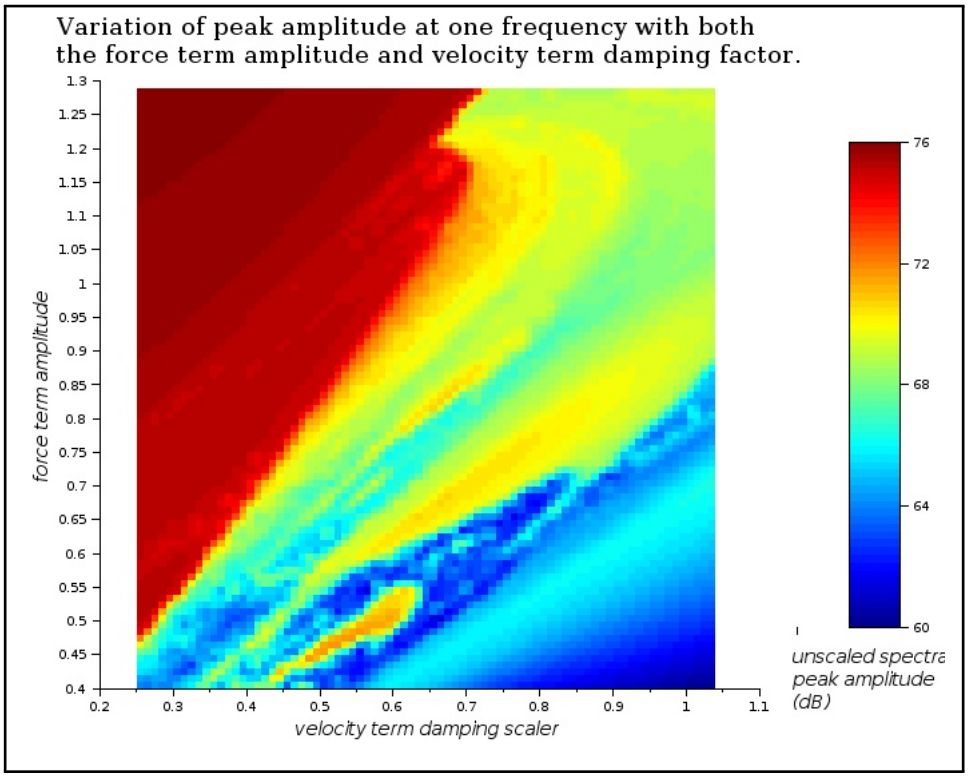

Figure 4.5: Two dimensional parameter space. Variation of Duffing output amplitude as a function of two independently varying parameters; damping δ and drive amplitude γ. Linear coupler α and nonlinear coupler β values fixed at 1 and 1 respectively. All other configuration values as in Table 4.2. (Benchmark values for damping and drive amplitude were $\delta = 0.5, \gamma = \gamma_c = 0.812$).

Figure 4.6 shows the results of the drive amplitude/nonlinear coupler parameter space investigation. The main features align in a slow curving diagonal from right to upper left, with the stable region of the limit cycle (high output amplitude) towards the upper and right third of the plotted parameter space. The isolated high amplitude

islands in this view also represent regions of near-stable dynamics but as the influence of the nonlinear displacement term x^3 is reduced as β reduces, these isolated regions produce higher output amplitudes. As before there is a clear demarcation between the lower amplitude chaotic regions and the stable limit cycle (high output amplitude) region. The small relatively flat region of lowest output amplitude at bottom right in Figure 4.6 is a stable trajectory within one energy minimum well of the bistable system. The baseline values of critical drive $\gamma_c = 0.812$ and nonlinear coupler $\beta = 1$ lie at the demarcation line but just within the chaos region.

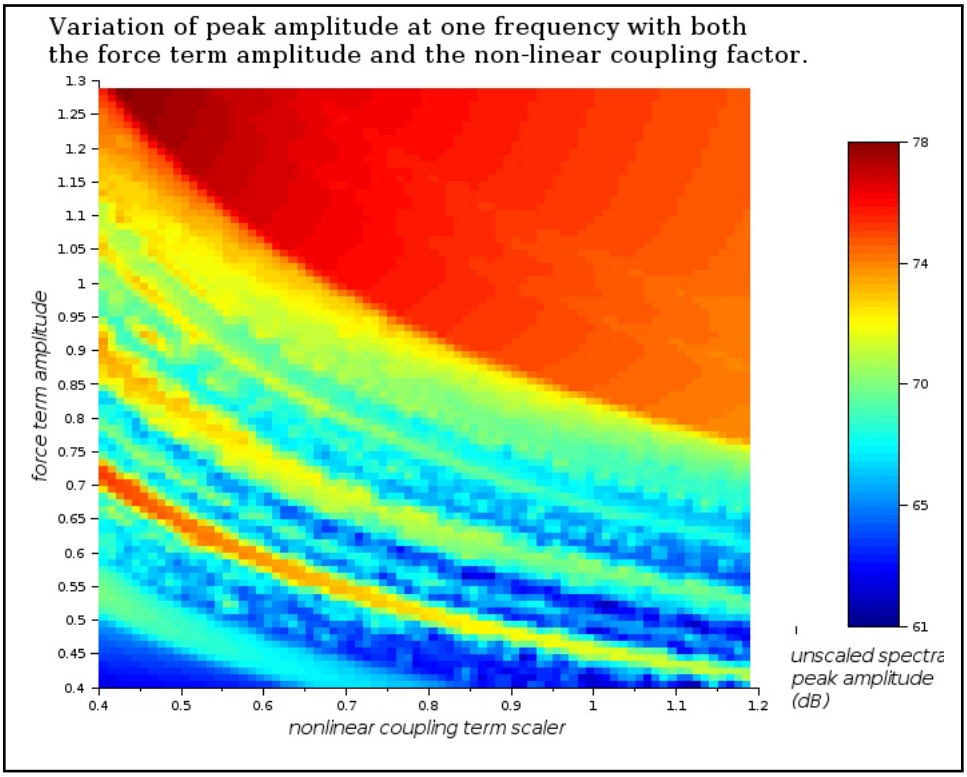

Figure 4.6: Two dimensional parameter space. Variation of Duffing output amplitude as a function of two independently varying parameters; nonlinear coupler β and drive amplitude γ. Linear coupler α and damping δ values fixed at 1 and 0.5 respectively. All other configuration values as in Table 4.2. (Benchmark values for nonlinear coupler and drive amplitude were $\beta = 1, \gamma = \gamma_c = 0.812$).

4.4.3 Varying the drive/linear coupler and nonlinear/linear couplers

Figure 4.7 shows the results of varying drive amplitude γ and the linear coupling term α. The range of features is the same as was seen in Figures 4.5 and 4.6, these are as follows. High output amplitude regions where the system has transitioned to the limit cycle. Medium amplitude regions that generally correspond to chaotic behaviour. Isolated islands of stability and high output amplitude but with crossing-trajectories. Finally, a relatively flat region at the lowest output amplitude in the bottom right corner.

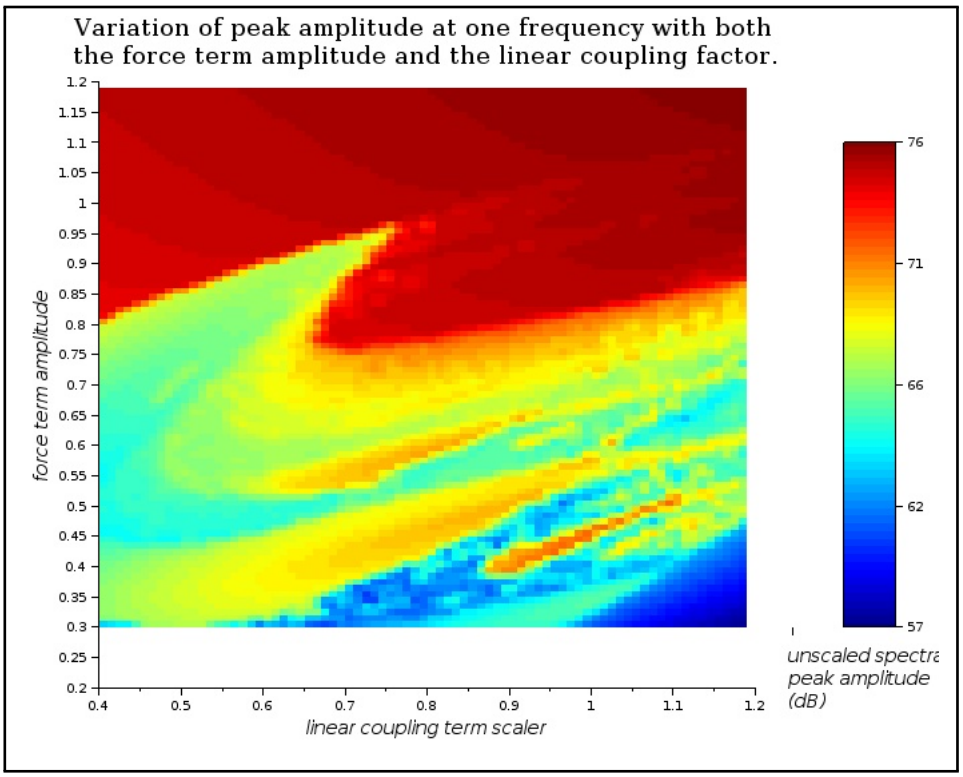

Figure 4.7: Two dimensional parameter space. Variation of Duffing output amplitude as a function of two independently varying parameters; linear coupler α and drive amplitude γ. Nonlinear coupler β and damping δ values fixed at 1 and 0.5 respectively. All other configuration values as in Table 4.2. (Benchmark values for linear coupler and drive amplitude were $\alpha = 1, \gamma = \gamma_c = 0.812$).

The final parameter space plot shown in Figure 4.8 shows the output amplitude as a function of the variation of linear and nonlinear coupling factors, α and β

respectively. As before the same set of four main features are all present; stable high output, chaos, isolated high points and low stable single well trajectories. In addition however, there is a fifth region of a distinct nature, that is flat and generates the lowest output amplitude (≈ -65dB) which is not single energy well trajectory. This region forms a 'fat finger' shape running diagonally from the left and thinning in width up to the centre top of the plotted area. This region represents a series of semi-stable trajectories in phase space that are non-crossing, almost circular and centred on the system unstable saddle point ($x = 0, \dot{x} = 0$). Importantly there are no generated frequencies additional to the drive frequency f and its harmonics, and it is adjacent to two regions of high (transitioned) output amplitude by a sharp 'cliff face' demarcation boundary.

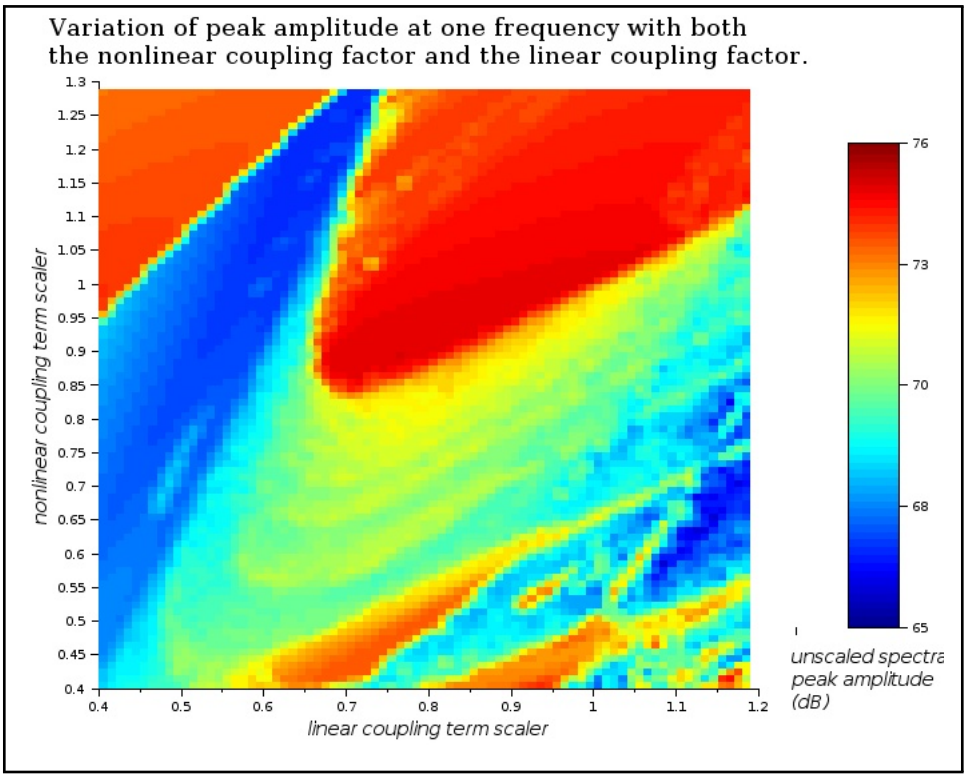

Figure 4.8: Two dimensional parameter space. Variation of Duffing output amplitude as a function of two independently varying parameters; nonlinear coupler β and linear coupler α. Drive amplitude γ and damping δ values fixed at 0.812 and 0.5 respectively. All other configuration values as in Table 4.2. (Benchmark values for linear coupler and drive amplitude were $\beta = 1, \alpha = 1$).

4.4.4 Selecting configurations

The Duffing system will operate as a pre-processor when suitable parameters are selected to place the system in a chaotic state just before transition to the stable limit cycle. The addition of extra energy at the right frequency, deriving from an input signal, will cause a transition and increase the output signal amplitude. The ideal requirement for the correct type of transition is; the high output region is the limit cycle, no extra frequencies additional to the drive/input frequency and its harmonics and the transition is sharp.

Suitable locations for parameter selections that meet the transition requirements can been seen on all four plots (Figures 4.5, 4.6, 4.7 and 4.8). These are marked by a clear and sharp change from low Duffing output displacement amplitude to high (and generally flat) output amplitude regions. For example, a sharp cliff face line between suitable low and high regions is shown as an obvious linear feature running from $(\delta = 0.25, \gamma_c = 0.45)$ to about $(\delta = 0.65, \gamma_c = 1.1)$ Figure 4.5. The demarcation between the two regions (red-high and light blue or yellow-lower) becomes progressively less distinct along this particular linear feature, as the transition becomes less abrupt. It is also noticeable that the difference between the high and low regions is greater (about 7 or 8 dB) near the $(\delta = 0.25, \gamma_c = 0.45)$ end compared to about 2 to 4 dB at the $(\delta = 0.65, \gamma_c = 1.1)$ end. In Figure 4.8 another curving and reasonably abrupt transition edge, with similar properties, is found between points $(\alpha = 0.4, \beta = 0.95)$ and $(\alpha = 0.7, \beta = 1.28)$.

Clearly there is more than one parameter set, that could satisfy the 'transition' system configuration requirement. However, it is possible to pick a small number of parameter configuration sets as alternatives that are different to the baseline set in Table 4.1, solely on the information gained from the limited parameter space survey and associated analysis carried out here. In addition to meeting the requirement outlined above parameters are also selected where they maximise the amplitude

difference at abrupt transition locations. It is assumed these conditions will provide the maximum detection performance.

In addition to the baseline configuration five further configurations were selected, these and the baseline configuration for the four parameters are summarised in Table 4.3. Configuration sets A and B were selected from Figure 4.5 and sets C and D from Figure 4.7. Set E is selected from Figure 4.8 and will be used to investigate the transition from the stable saddle point trajectory to the limit cycle. This transition was described above, and is clearly a different type of transition with a larger amplitude change.

Parameter	Baseline	Set A	Set B	Set C	Set D	Set E
Critical amplitude γ_c	0.812	0.51	1.25	0.812	0.93	0.812
Damping factor δ	0.5	0.3	0.7	0.5	0.5	0.5
Linear coupling α	1	1	1	0.45	0.72	0.7
Nonlinear coupling β	1	1	1	1	1	1.15

Table 4.3: Alternative Duffing parameter configuration values. Also included in the last line, is the corresponding minimum input signal amplitude required to cause transition, for the given critical force amplitude γ_c.

4.5 Basic detection performance

The first Receiver Operating Characteristics (ROC) analyses will be carried out in this section. The aim is to quantify the impact on detection performance of the chaos-to-stable transition pre-processing. The calculation of ROC curves were introduced in Chapter 2 Section 2.2.4. This will be carried out for all the transition configurations shown in Table 4.3 using the simplest input signal and basic binary decision (single threshold) detection in the frequency domain.

Six analyses were completed for the baseline configuration and the five new parameter combinations. The frequency of both the internal drive f_0 and the input sine wave f,

was fixed at 489.92 Hz for all analyses. The initial conditions for the RK4 solver were fixed at $(x_0 = 0, \dot{x_0} = 0)$, and the phase difference between the two periodic force components was fixed at $\phi = 0$. The third forcing term was white Gaussian noise. Three ROC curves were generated for each of the six configurations, using 500 realisations each of the two periodic terms and identical but independently distributed noise at each realisation. The three curves were comprised of one measurement using the FFT only (no Duffing pre-processing), and two with Duffing pre-processing as well as the FFT of their outputs. The two Duffing ROC curves were obtained using the same input S/N but different input signal power levels. The first power level was dictated by the minimum input sine wave amplitude needed to trigger transition (A_m), the second by increasing the sine wave amplitude until a stable maximum in detection performance (highest ROC curve position) was found. To maintain the same input S/N the Gaussian noise deviation was also increased. The first FFT only ROC curve represents conventional detection processing and forms the comparator common across all six ROC analyses.

To generate the ROC data the first step in all six cases was to check that the critical internal drive γ_c values read from the parameter space investigation plots, configure the Duffing system as chaotic but near to stability. This was carried out by a series of trial and error small increments of γ until the system transitioned and the stable limit cycle was observed in phase space. The critical internal drive was then selected as the last value not causing transition. During this process the other two force terms (sine wave and noise) were excluded. Next, in each case the internal drive term was configured with the critical amplitude γ_c value found for that case, then the minimum input sine wave amplitude A_m causing transition to the limit cycle was found by a similar trial and error method. The minimum sine wave amplitude varies across the six configurations because the size and abruptness of the transition region varies.

Finally the Gaussian noise deviation value was selected so that the input signal power

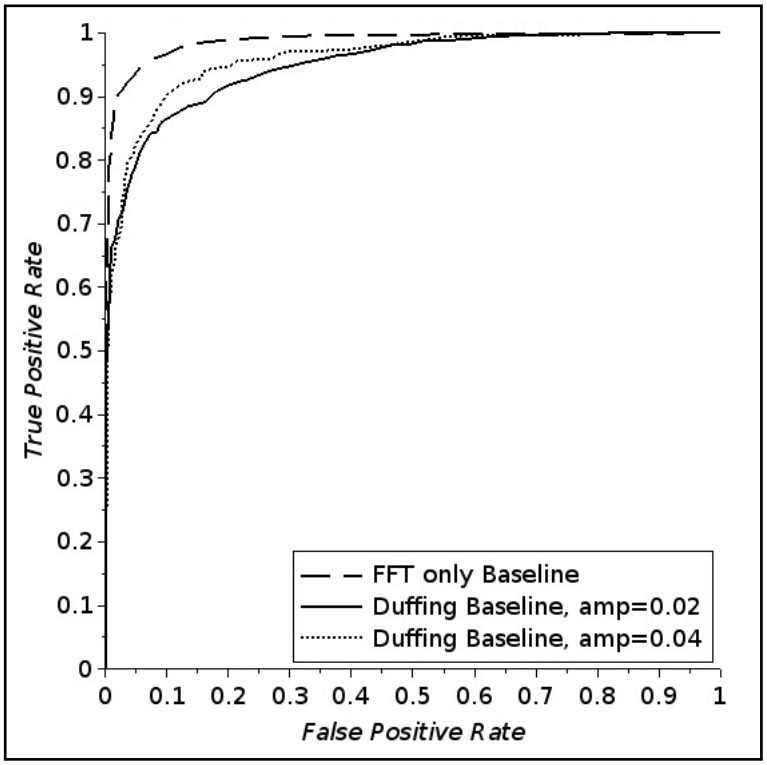

Figure 4.9: Basic detection performance ROC curves, configuration SET 'BASELINE': Single tone in white Gaussian noise. Parameter configuration: Coupling $\alpha = \beta = 1$, critical internal drive amplitude $\gamma_c = 0.812$ and damping factor $\delta = 0.5$. Input S/N is the same for all ROC curves. Minimum input sine wave amplitude to trigger transition is $A_m = 0.02$, with input noise deviation $\sigma = 0.23$. Input sine wave amplitude for maximum detection performance is $A = 0.04$ with noise $\sigma = 0.46$. Frequency $f_0 = f =$ 489.92Hz, phase difference $\phi = 0$, solver initial conditions $(x_0 = 0, \dot{x_0} = 0)$.

ratio's (${A_m}^2/\sigma^2$ and A^2/σ^2) were identical across all ROC curves in all six configurations in this section, even though the total input power varies. To generate the third ROC curve it was necessary to select an additional input sine wave amplitude A. In this case the ROC analysis was repeated for each small increment in input sine wave amplitude, until the ROC curve position converged to a stable (maximum detection performance) point. At this point further increases in input amplitude do not improve detection performance and in some cases begin to degrade performance. As before, at each increment of A the input S/N was maintained by incrementing noise deviation too.

The results of the first three ROC analyses with Duffing configured using the baseline

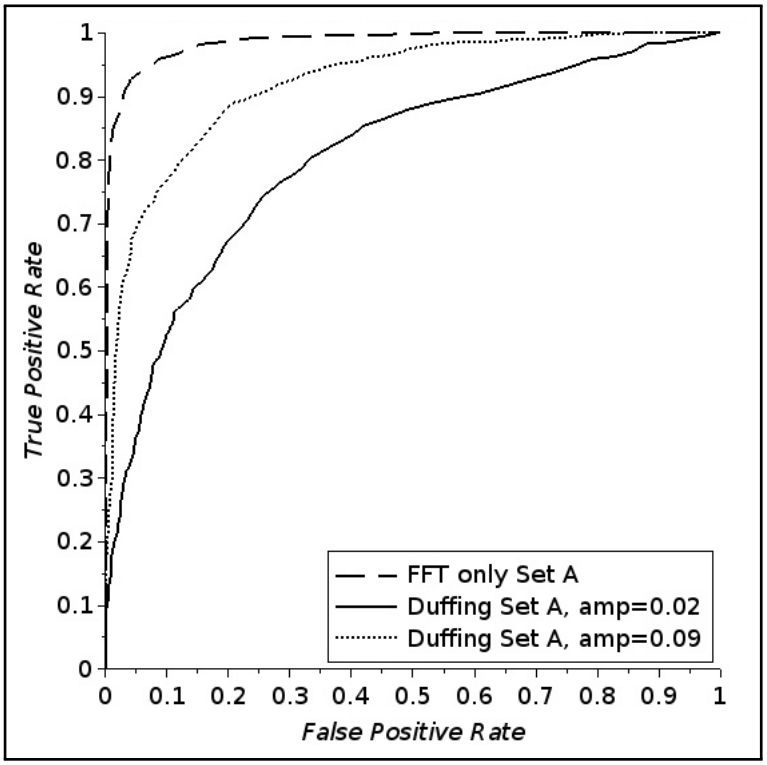

Figure 4.10: Basic detection performance ROC curves, configuration SET 'A': Single tone in white Gaussian noise. Parameter configuration: Coupling $\alpha = \beta = 1$, critical internal drive amplitude $\gamma_c = 0.51$ and damping factor $\delta = 0.3$. Input S/N is the same for all ROC curves. Minimum input sine wave amplitude to trigger transition is $A_m = 0.02$, with input noise deviation $\sigma = 0.23$. Input sine wave amplitude for maximum detection performance is $A = 0.09$ with noise $\sigma = 1.035$. Frequency $f_0 = f = 489.92$Hz, phase difference $\phi = 0$, solver initial conditions $(x_0 = 0, \dot{x_0} = 0)$.

parameter set from Table 4.3, are shown in Figure 4.9. The two ROC curves that use Duffing pre-processing are lower than the FFT-only curve, the detection performance is worse for all Duffing pre-processing in this baseline configuration. The maximum detection performance using pre-processing occurs when the input sine wave amplitude is $A = 0.04$, twice the minimum amplitude value ($A_m = 0.02$) that triggers transition. The True Positive Rate (TPR) of three curves (FFT-only, 'Duffing minimum' and 'Duffing best') can be compared at a fixed False Positive Rate (FPR). A low FPR is usually desirable in detection problems, so a FPR = 0.1 is selected arbitrarily. At this FPR the TPR values for the three ROC curves are ~ 0.97, ~ 0.9 and ~ 0.86 respectively.

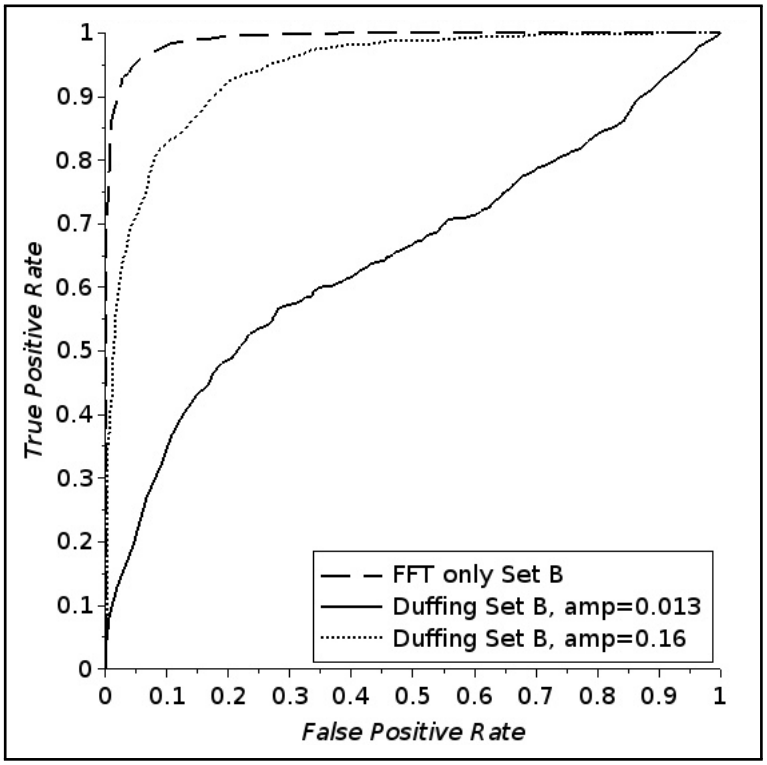

Figure 4.11: Basic detection performance ROC curves, configuration SET 'B': Single tone in white Gaussian noise. Parameter configuration: Coupling $\alpha = \beta = 1$, critical internal drive amplitude $\gamma_c = 1.25$ and damping factor $\delta = 0.7$. Input S/N is the same for all ROC curves. Minimum input sine wave amplitude to trigger transition is $A_m = 0.013$, with input noise deviation $\sigma = 0.1495$. Input sine wave amplitude for maximum detection performance is $A = 0.16$ with noise $\sigma = 1.84$. Frequency $f_0 = f = 489.92$Hz, phase difference $\phi = 0$, solver initial conditions $(x_0 = 0, \dot{x_0} = 0)$.

The results for configuration sets 'A' and 'B' are shown in Figures 4.10 and 4.11 respectively. The detection performance is worse than the FFT-only case for both configurations. The TPR values for 'Duffing best' and 'Duffing minimum', at FPR = 0.1 are; for configuration set 'A', ~ 0.77 and ~ 0.54. For set 'B', ~ 0.82 and ~ 0.37. All four Duffing pre-processing ROC curves are worse when individually compared to their corresponding curves obtained for the baseline configuration, (Figure 4.9). Comparing configurations 'A' and 'B' the best detection performance is obtained from set 'B'.

The results for configuration sets 'C' and 'D' are shown in Figures 4.12 and 4.13 respectively. The detection performance is again worse than the FFT-only case for

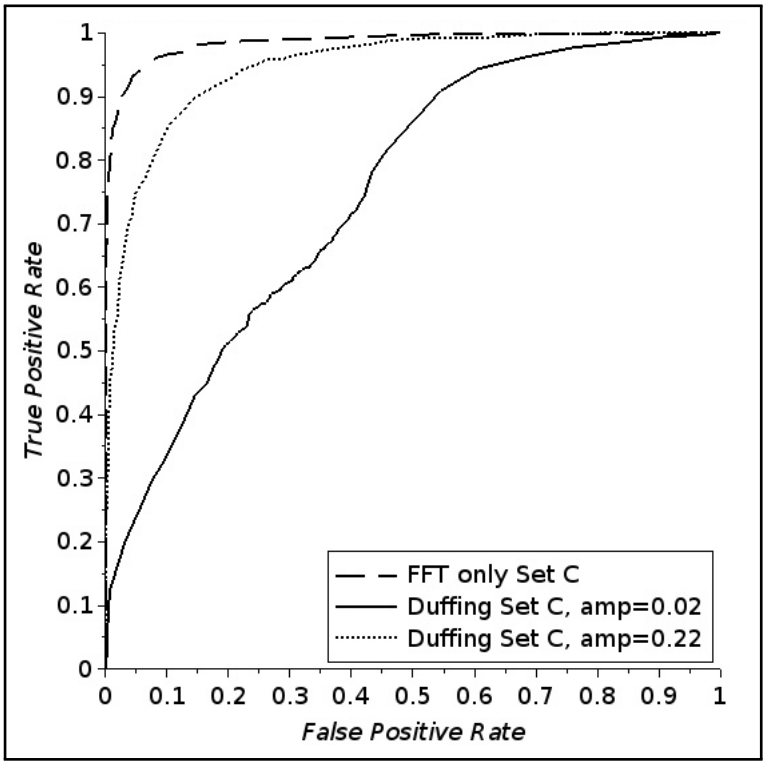

Figure 4.12: Basic detection performance ROC curves, configuration SET 'C': Single tone in white Gaussian noise. Parameter configuration: Coupling $\alpha = 0.45$ and $\beta = 1$, critical internal drive amplitude $\gamma_c = 0.812$ and damping factor $\delta = 0.5$. Input S/N is the same for all ROC curves. Minimum input sine wave amplitude to trigger transition is $A_m = 0.02$, with input noise deviation $\sigma = 0.23$. Input sine wave amplitude for maximum detection performance is $A = 0.22$ with noise $\sigma = 2.53$. Frequency $f_0 = f = 489.92$Hz, phase difference $\phi = 0$, solver initial conditions $(x_0 = 0, \dot{x_0} = 0)$.

both configurations. The TPR values for the Duffing 'best' and 'minimum' ROC curves at FPR = 0.1 are; for configuration set 'C', ~ 0.85 and ~ 0.33 and for set 'D', ~ 0.85 and ~ 0.31. The 'best' ROC curves for configuration sets 'B', 'C' and 'D' show very similar detection performance. The Duffing 'minimum' curves also show very similar performance at low FPR.

The large difference between Duffing 'best' and 'minimum' ROC curves that exists for the three configurations 'B', 'C' and 'D' is caused by a large change in the distribution of the output amplitudes at the frequency of the sine wave. At the minimum input sine wave amplitude the output distribution is asymmetric with negative skewness and a large variance (long tail). At Duffing 'best' performance the

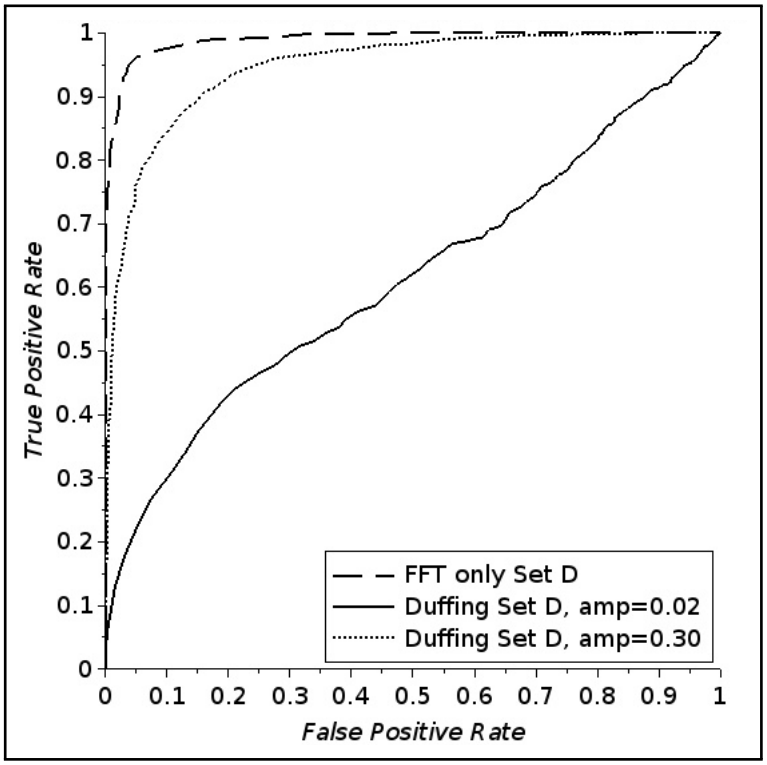

Figure 4.13: Basic detection performance ROC curves, configuration SET 'D': Single tone in white Gaussian noise. Parameter configuration: Coupling $\alpha = 0.72$ and $\beta = 1$, critical internal drive amplitude $\gamma_c = 0.93$ and damping factor $\delta = 0.5$. Input S/N is the same for all ROC curves. Minimum input sine wave amplitude to trigger transition is $A_m = 0.02$, with input noise deviation $\sigma = 0.30$. Input sine wave amplitude for maximum detection performance is $A = 0.04$ with noise $\sigma = 3.45$. Frequency $f_0 = f = 489.92$Hz, phase difference $\phi = 0$, solver initial conditions $(x_0 = 0, \dot{x_0} = 0)$.

distribution has become almost symmetrical and Gaussian like, with a smaller variance. The mean is approximately the same for both distribution types.

The ROC analyses for the final configuration set 'E' are shown in Figure 4.14. The Duffing 'best' and 'minimum' ROC curves are better than their corresponding curves found for configurations 'B', 'C' and 'D'. They are also better than set 'A' but not as good as the baseline configuration.

The strategy of selecting a better parameter configuration for the Duffing pre-processor based on a more abrupt transition between states as seen in the parameter space investigations, is shown by these results to be flawed. The baseline configuration generated the best detection performance results but even those do not

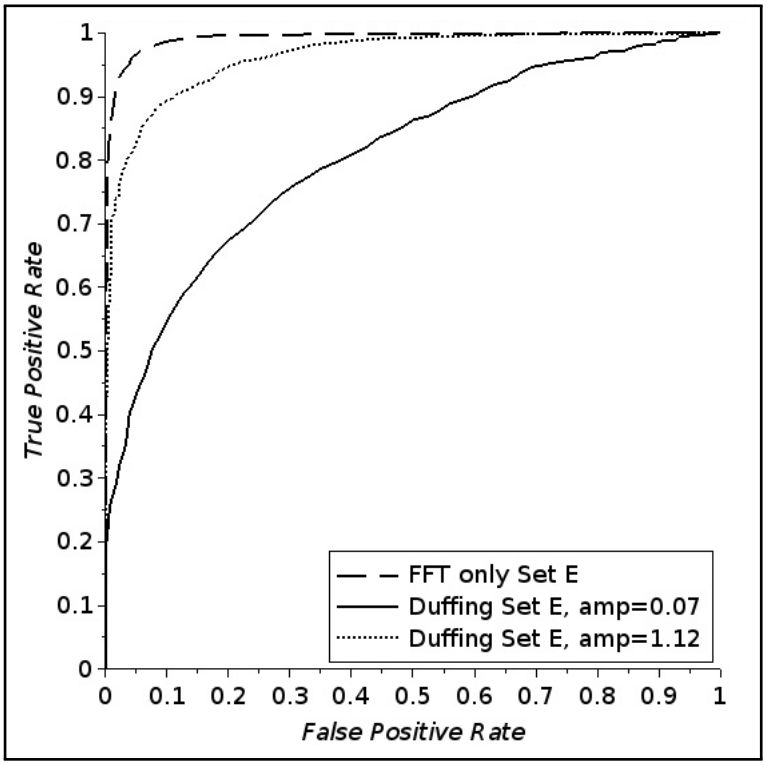

Figure 4.14: Basic detection performance ROC curves, configuration SET 'E': Single tone in white Gaussian noise. Parameter configuration: Coupling $\alpha = 0.7$ and $\beta = 1.15$, critical internal drive amplitude $\gamma_c = 0.812$ and damping factor $\delta = 0.5$. Input S/N is the same for all ROC curves. Minimum input sine wave amplitude to trigger transition is $A_m = 0.07$, with input noise deviation $\sigma = 0.80$. Input sine wave amplitude for maximum detection performance is $A = 0.04$ with noise $\sigma = 0.46$. Frequency $f_0 = f = 489.92$Hz, phase difference $\phi = 0$, solver initial conditions $(x_0 = 0, \dot{x_0} = 0)$.

outperform the conventional processing using FFT-only detection.

4.6 Impulsive noise input

The aim in this section is to understand the impact on detection performance with the Duffing pre-processing stage, when the input signal contains impulsive noise. The performance of the Duffing limit cycle mechanism is assessed using simulated input noise that is more representative of a type of underwater noise, specifically impulsive noise is considered. The motivation for investigating impulsive noise remains the same as was described in the previous chapter in Section 3.5.2. The Duffing model of Equation (4.1) is modified with an additional forcing term. The 'internal' periodic

force term is retained $\gamma \cos(2\pi f t)$, as before, however in this section the input signal is now simulated by three further additive terms; a sine wave $A \cos(2\pi f t)$, impulsive noise and Gaussian noise. These three terms represent; the signal to be detected, an impulsive background noise source in the sea such as snapping shrimp and the background ambient sea noise modelled as Gaussian white noise. As before the internal periodic force term continues to act as part of the Duffing pre-processor configuration.

Two axes of investigation are considered; different configurations of the Duffing system (as used in previous sections), and different variance ratios for the Gaussian to impulsive input noise mixture. The detection performance is measured using ROC analysis, and all measured ROC curves are also compared to the performance without the Duffing system. ROC analysis in all cases is achieved by fast Fourier transforming into the frequency domain and then by collecting amplitude statistics only from the fixed bin of the input sine wave frequency, with and without the sine wave component present at the input.

Parameter	Baseline	Set A	Set B
High S/N noise deviation σ_g	0.0716308	0.1611694	0.2865234
Low S/N noise deviation σ_g	0.1432616	0.3223388	0.5730468
Sine wave amplitude A	0.04	0.09	0.16

Table 4.4: Summary of the input signal amplitude and noise deviation settings for the three Duffing configurations used to generate Figures 4.16, 4.17 and 4.18. The three Duffing configuration settings are summarised in Table 4.3. In all cases the initial conditions were $x = \dot{x} = 0$ and phase $\phi = 0$. The high input SNR is -21.25dB and the low SNR is -27.25 dB, in all cases.

The impulsive noise used here was generated in the same way as described in Section 3.5.2 of the previous chapter. The position of the impulsive noise excursions (spikes) and the variation in spike peak amplitude, were randomised using a uniform distribution. The spike density in the input signal time series was fixed at 165, and the fixed overall spike amplitude multiplier fixed at 56. These values were held the same for all tests in this section, as was the simulated input signal time length. The

noise deviation value was used to control the overall variance of the impulsive noise component by acting as a second multiplier on its overall amplitude. The same deviation value was also used to generate the zero mean Gaussian noise component as well, but there are no other multipliers on Gaussian noise amplitude. The impulsive noise excursions followed the same form as before, one positive going spike closely followed by a negative going spike. The two noise components and the sine wave were added together to form the simulated input signal. Figure 4.15 shows a) a typical impulsive input signal, and b) one of the impulsive noise spikes.

In the first sequence of three tests, ROC analyses were conducted with the normalised Duffing configured according to three of the parameter value sets shown in Table 4.3 (Baseline, 'A' and 'B'). The aim was to investigate the detection performance at two different input S/N for each of the three configurations, using highly impulsive noise noise in all setup cases. In order to make the input noise 'highly impulsive' the variance of the impulsive component was set to be approximately 40 times larger than the variance of the Gaussian white noise component. This was achieved by setting the spike density, noise deviation and multiplier. Here the input snr value was calculated from the peak-to-peak input sine wave amplitude A and the total of the two input noise variances $\sigma_T^2 = \sigma_i^2 + \sigma_g^2$ so that $snr = A^2/\sigma_T^2$. The ratio of the variances of the two input noise components σ_g^2/σ_i^2, and the sine wave amplitude A, were both held constant for the two input S/N regimes and for all three Duffing configurations.

The internal periodic force frequency was set to be bin-centred in the frequency domain, and set the same as the simulated input sine wave, at $f = f_0 = 324.5614$ and the input sine wave amplitude was set for each configuration as; baseline $A = 0.04$, 'A' $A = 0.09$ and 'B' $A = 0.16$. These values were chosen to be the same as was used in Section 4.5 and for the same reasons. The noise deviation σ_g used also had to vary, in order to maintain the required input S/N. A summary of these setup values is given in Table 4.4, for each Duffing configuration.

The input (calculated) SNR values achieved were ≈ -21.25 dB and ≈ -27.25 dB for

the low and high values used in all three Duffing setups. There was a maximum variation of approximately 0.15dB on these values caused by the randomisation of the spike size in the finite length input signal time-series, affecting the overall noise variance value $\sigma_T^2 = \sigma_i^2 + \sigma_g^2$ used in the snr calculation (A^2/σ_T^2).

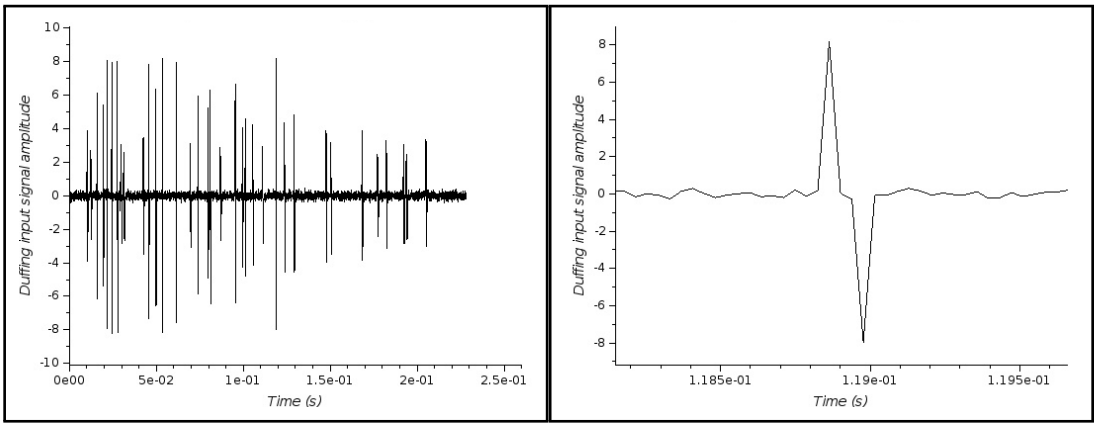

(a) (b)

Figure 4.15: Typical simulated 'highly impulsive' input signal. The three additive components combined (two noise and the sine wave). (a): Input signal. Excess kurtosis as defined in Equations (3.5) and (3.6) $y_e = 21.75$. (b): An example of one impulse spike.

The ROC analysis results using the baseline Duffing system configuration are shown in Figure 4.16. Two pairs of ROC curves are show, one pair at high S/N and the other at low S/N. Within each pair one curve was generated using the Duffing pre-processor (solid line labelled as 'Duff') and the second curve without (dotted line labelled as 'FFT'). For the high S/N the detection performances with and without the Duffing pre-processor are almost identical. For the low input S/N case the detection performance with Duffing pre-processing is much better than the measured performance without.

The ROC analyses results for Duffing configurations 'A' and 'B' are shown in Figures 4.17 and 4.18. The detection performance at low input S/N, using the Duffing pre-processor is better than without in both configuration cases. At high input S/N the performance with and without Duffing system are no longer close. The Duffing

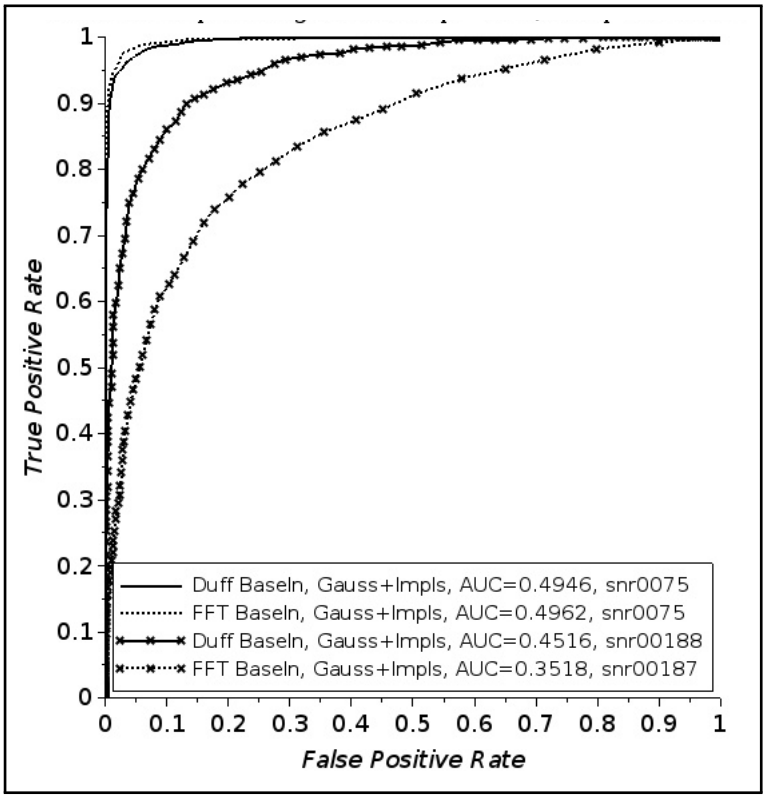

Figure 4.16: Duffing configuration type 'Baseline'. ROC curves at two S/N regimes, with ('Duff') and without ('FFT') Duffing pre-processing. Sine wave in impulsive noise. Amplitude statistics collected from 1400 realisations. Excess kurtosis $y_e = 19.80$ at lower S/N, and $y_e = 2.73$ at the higher S/N

case is now comparatively worse than without pre-processing and also worse than the equivalent situation in the baseline configuration.

The area-under-curve (AUC) values given on Figures 4.16, 4.17 and 4.18 quantify the variation in detection performance. AUC is calculated here, by integrating the ROC curve between 0 and 1.0 false positive rates, and dividing by 2. The AUC values for symmetric ROC curves generated from unimodal distributions, calculated in this way always fall in the range $0.0 \leqslant \text{AUC} \leqslant 0.5$. The AUC values calculated from the results shown in Figures 4.16, 4.17 and 4.18 are summarised in Table 4.5 below.

The AUC data clearly indicate that the baseline Duffing configuration generates the

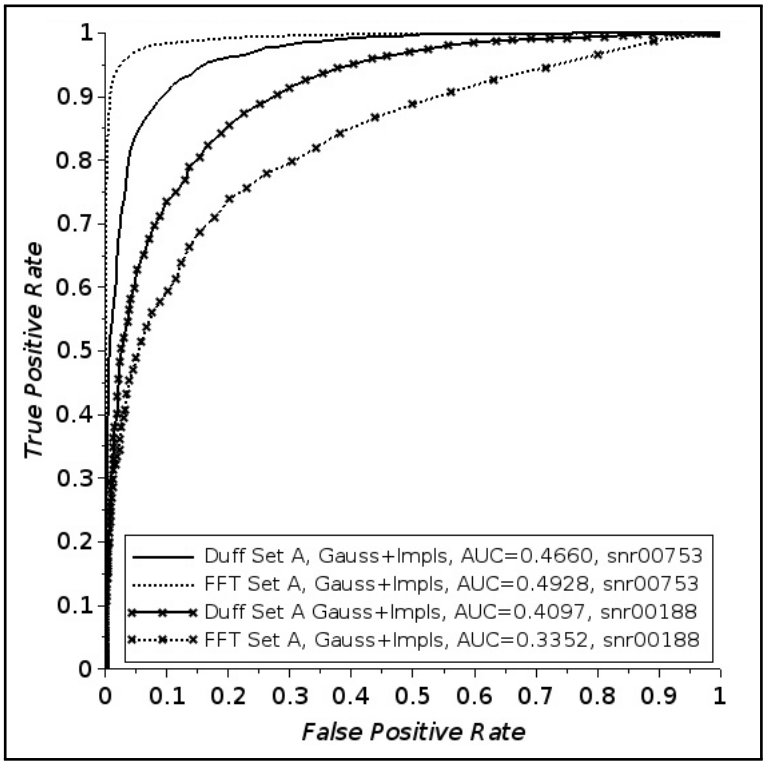

Figure 4.17: Duffing configuration type 'A'. ROC curves at two S/N regimes, with ('Duff') and without ('FFT') Duffing pre-processing. Sine wave in impulsive noise. Amplitude statistics collected from 1400 realisations. Excess kurtosis $y_e = 117.93$ at lower S/N, and $y_e = 34.22$ at the higher S/N.

Input S/N	Baseline	Set A	Set B
High (≈ -21.25dB)	0.4946	0.4660	0.4646
Low (≈ -27.25dB)	0.4516	0.4097	0.4027

Table 4.5: Summary of the AUC results for the Duffing pre-processor ROC curves only, for the three configuration cases; 'baseline', 'A' and 'B'.

best detection performance compared to configurations 'A' and 'B', for both S/N cases investigated.

The impact of impulsive noise on detection performance was investigated in the previous chapter on Stochastic Resonance, Section 3.5.2. Exploiting the SR mechanism provided no improvement in performance, in fact the performance was degraded. The findings shown in this chapter show that the chaos-to-stable transition mechanism does show detection performance improvement for the conditions investigated. The results show that performance using the Duffing chaos-to-stable

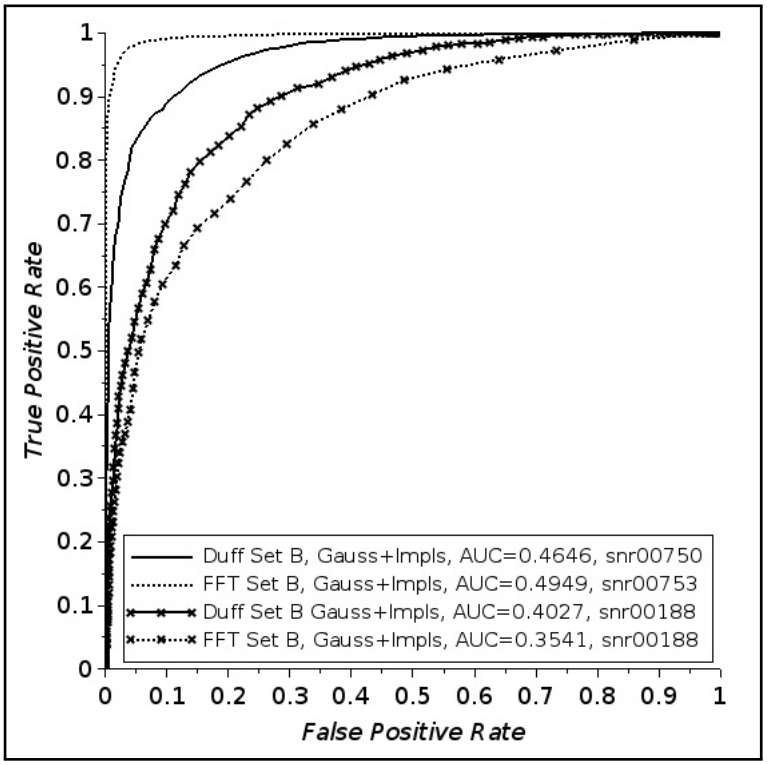

Figure 4.18: Duffing configuration type 'B'. ROC curves at two S/N regimes, with ('Duff') and without ('FFT') Duffing pre-processing. Sine wave in impulsive noise. Amplitude statistics collected from 1400 realisations. Excess kurtosis $y_e = 421.39$ at lower S/N, and $y_e = 88.30$ at the higher S/N.

transition mechanism is better than a representative 'conventional' detection processing scheme, at low input S/N when the noise component is highly impulsive. At the higher input S/N the performance increases as expected, both with and without Duffing pre-processing. However, the increase is less marked with the Duffing system than without. For the configurations tested, the 'Baseline' configuration provides the best detection performance, matching the 'conventional' detector (no Duffing pre-processing) at high input S/N and significantly outperforming the 'conventional' detector by the largest margin, at low S/N.

4.7 Discussion

Configuring a nonlinear system using an internal periodic force to place the system close to transition to a stable state may impose a narrow bandwidth on the system. Only input signals having a frequency close to the 'internal' drive frequency will initiate transition. This is not a feature of the nonlinear system but is simply the linear combination of two periodic forces. The notion that a Duffing pre-processor may have narrow bandwidth has significance in the development of a wideband detection system based on Duffing oscillators. This is explored in the next chapter.

A Duffing system parameter space investigation was carried out by varying selected pairs of Duffing configuration control parameters. Strategies to select parameter pairs with the potential to improve the detection performance were examined. These included increasing the abruptness and size of the transition to stable behaviour, and selecting a very large transition from very low amplitude to the higher amplitude limit cycle (periodic to periodic). ROC analysis has shown that the baseline configuration outperforms the other Duffing system configurations examined. However, none of the configurations were observed to outperform a simple benchmark linear detection scheme based on amplitude thresholding in the frequency domain without nonlinear pre-processing.

Increasing the amplitude of the simulated input sine wav signal of interest by a small amount over an above A_m results in marginally improved ROC curves, and therefore improved detection performance. All the ROC analyses in Section 4.5 exhibit this small change, which is in agreement with the results shown in Figure 4.2. A single periodic force term was used to generate that figure, however a linear addition of two in-phase and identical frequency force terms, which is the case for the ROC analyses, would generate the same result as Figure 4.2. The marginal improvement converges to a point where no further detection performance can be had.

The baseline Duffing configuration appears to perform almost as well, at high S/N, as

the benchmark linear detector, when the input signal contains a dominant component of simulated highly impulsive noise. The simulated noise was constructed to mimic the time domain form of a single percussive snap made by many species of snapping shrimp. Colonies of these shrimp can produce extremely loud impulsive noise that linear detectors usually fail to penetrate to detect the SoI. The ROC analysis at low S/N shows the Duffing system clearly outperforming a linear detector. This result is very significant, snapping shrimp are a common problem for underwater detection of acoustic signals. However, this single result for a simulated case would need further close examination before it can be regarded as a robust outcome that might be exploited. Impulsive noise is re-examined in the next chapter.

Chapter 5

Further Development, and Applications

5.1 Introduction

Two mechanisms found in many nonlinear system models, stochastic resonance (SR) and a particular chaos-to-stable transition mechanism were introduced and explored in Chapters 3 and 4 respectively. No improvement to detection performance was found when using SR as a pre-processing stage, for the scenarios were considered. Similar scenarios were investigated using the Duffing chaos-to-stable transition mechanism as a pre-detection processor. Several different Duffing configurations considered. Significant improvement in detection performance was only found for a small group of configurations and only when the noise components of the input signal were dominated by highly impulsive noise.

A common theme in this thesis of the SR investigation and the transition mechanism investigations is the use of simulated data. The purpose was to ensure all aspects affecting performance were fully controllable, including the content of the simulated input signal and the quantities that defined it. The step taken in this chapter is to focus on real data by developing the transition mechanism into a form that can be

used on real input signals.

The goal of this chapter is to demonstrate the application of nonlinear pre-processing before detection, including a wideband implementation that presents output in the form of a time-frequency visualisation. First it is necessary to investigate some nonlinear system behaviours further, building on the the initial behaviours work described in Chapter 4. The outcome of this is then used to develop some modifications to the processing, that enable detection of real signals wideband and narrowband.

5.2 Methods

5.2.1 The model

It was shown in Chapter 4 that the transition to stable motion mechanism had some potential to improve detection performance in highly impulsive noise. The positive result provides the motivation to discard SR and continue using the Duffing transition in this chapter. Therefore the same model used in Chapter 4 will be used in all the investigations discussed in this chapter. The majority of the investigations in this chapter will use the frequency normalised version of the Duffing system set up as the baseline configuration, unless otherwise stated. The model was defined in detail, in Section 4.2.1 and Section 2.3.3 of the previous chapter and the full baseline configuration is given in Table 4.3.

The output from the Duffing nonlinear systems used in this chapter are found in the same way as was used in Chapter 4. The fixed step size four stage Runge-Kutta solver was introduced in Section 4.2.1 and the method is described in Appendix A.

5.2.2 Performance measures

As in previous chapters Receiver Operating Characteristic (ROC) analyses will be the sole measure of detection performance used throughout this chapter. ROC analysis normally requires the detector to be a binary classifier, in other words the detector can have only two outcomes or 'classes'. It will be shown in this chapter that the output from the Duffing filter can present three regions in its probability density and so the most common form of ROC analysis cannot be used unless this issue is managed. It is worth noting at this point that research into developing ROC analysis methods for three or more decision classes is ongoing, see for example [32, 33], multi-class ROC analysis will not be used in this thesis. It will be shown later in this section that the multi-class issue manifests in some cases as bi-modal output probability distributions. The problem of establishing meaningful binary decision ROC analyes on bi-modal pdf's is solved in two ways in this chapter, as a fortunate bi-product of the new processing introduced in the following sections, four-phase processing and correlation detection.

The range of testable scenarios generated by; different input data types, performance improvement measures and other configuration changes, is too large for a full pair-wise comparative ROC analysis to be carried out. The scale of the assessment task is further compounded by the selected approach of comparing each scenario with a conventional detection scheme. In fact there are two benchmark detection schemes used in this chapter. The first is the same as has been used in all previous chapters, which is to fast Fourier transform (FFT) the time-series data output from the nonlinear pre-processing stage and detect using amplitude thresholding, either in a fixed frequency bin or by maximum spectral peak picking. The second benchmark is a variant of this and used for the first time in this chapter, the four-phase processing (described in detail in Section 5.2.5 and Section 5.2.6) is applied, and the amplitude of the largest peak of the four resulting spectra is selected as the detection statistic.

It is necessary to define the comparison metric by which one ROC curve is quantified to be better or worse than another. The region bounded by the ROC curve and the equal probability line (true positive rate (TPR) = false positive rate (FPR)) is known as the half-area under curve (AUC). As a general measure the largest value for AUC is used as the comparison quantity, the larger the value the better the detection performance. However, if the curves are not symmetrical this single measure may no longer be suitable as a comparator even though the calculated value of AUC will still be accurate. This is because different areas within the area AUC may have different impact on detection performance. Often the lower false alarm rate regions are of more interest than the higher false alarm rate areas, a situation which can generate misleading comparison outcomes when only considering the AUC value without viewing the shape of the ROC curves. Fortunately most of the ROC curves generated in this chapter are visually symmetric, apart from a few significant examples where AUC is not used.

Most analyses presented in this chapter use simulated data as the input signal, comprised of a single periodic tone and additive Gaussian distributed noise. The ROC analysis models used were configured as a two-pass process. On each iteration the first pass used the noise alone and the second pass used the noise and tone. For each such two-pass iteration identical Gaussian noise data were used, but each subsequent two-pass iteration used a completely fresh noise data set, pseudo-randomly re-seeded from the computer clock second value.

5.2.3 Initial transient

The Duffing system will almost never transition to the stable limit cycle at the same time the periodic force term is applied. There is almost always a time lag marked by an initial non-periodic or chaotic motion sequence. A model for the time length of this initial transient was introduced in the previous chapter in Section 4.3.1.

It is not possible to discriminate between the system dynamics during an initial

transient, and the chaotic motion of the system in the absence of a periodic signal. The low amplitude of this transient can form from 3% to 15% of the total time-series output from the Duffing system, for the investigations and tests described in this chapter. Therefore a FFT of the output will exhibit reduced S/N as a result of the reduced apparent output signal power over the time length of the output time-series. This is mitigated by discarding the initial transient before any further signal processing is carried out.

A series of tests were carried investigating how many points of the initial transient need to be discarded given the narrow range of sample rates and input time-series lengths used. It was found that discarding the first 200 points of Duffing output was a suitable compromise, the size of the discard was therefore fixed at 200 points for all runs in this chapter, unless otherwise stated.

5.2.4 Replica correlation detection

The investigations carried out in Chapter 3 and Chapter 4 used the same simple detection scheme in all cases, and where detection formed part of the analyses. The output of the nonlinear system was fast Fourier transformed and detection (measurement) performed on the fixed frequency bin corresponding to the known input sine wave used to simulate an input signal. Observation of the phase space dynamics or the time-series output from the Duffing system in limit cycle stable motion shows that the periodic output is not sinusoidal, it has some harmonic content. A single binary decision threshold detection scheme operating in the frequency domain will not take account the information contained in the harmonics of the output signal. Given that the Duffing system is configured to improve detection performance, ignoring harmonic content that only appears in response to the input sine wave may be producing sub-optimal detection performance. Since the aim of this chapter is to move towards the demonstration of a practical detector using real data, a different detector that exploits the harmonics may offer improved performance in a

real system.

To exploit the harmonic content in the output a matched filter detection approach is used through out this chapter instead of frequency domain threshold detection. Matched filtering here is achieved by generating a noise free replica of the stable limit cycle and using this to perform replica correlation on the output of the Duffing system. Detection is still a binary decision scheme however the detection threshold is set on the output of the correlation process. The viability of matched filtering as a detection scheme at the Duffing output depends on two properties of the Duffing system, these are described below.

One of the properties of the Duffing system in stable (limit cycle) motion is that provided the input signal amplitude is at or very near the minimum detectable amplitude A_m, the position of the the limit cycle is almost constant. This is illustrated in Figure 4.2 of Chapter 4. The stable motion corresponds to the plateau region from 0.9 to 0.94 periodic drive term amplitude, where the variation in output amplitude is about 2%. The displacement variable x of limit cycle trajectory as seen in phase space will therefore vary by approximately 2% or 3% for the range of Duffing configurations and input signal amplitudes considered in this chapter.

A second useful property of the normalised Duffing system is that the position of the trajectory of the limit cycle for the frequency normalised Duffing system does not vary in size with frequency. The generation of a pre-formed replica limit cycle viable across all frequencies is therefore trivial. This is achieved by numerically solving a separate *replica generating* Duffing system without the additive noise or input force terms (noise variance and input amplitude both set to zero). The remaining internal force term is configured with a fixed amplitude value large enough to cause transition to stability. The amplitude of the force term used to generate the stable replica limit cycle is always the same no matter what the internal force frequency (ω_0) is set to. Therefore the generation of the replica limit cycle is fully controllable and requires no prior knowledge of the input to the system. The output of the *detection* Duffing

system with an unknown and noisy input is correlated with the output of the *replica generating* Duffing system. In fact, a replica is generated for both the displacement and velocity components output (x_r and $\dot{x}_r$).

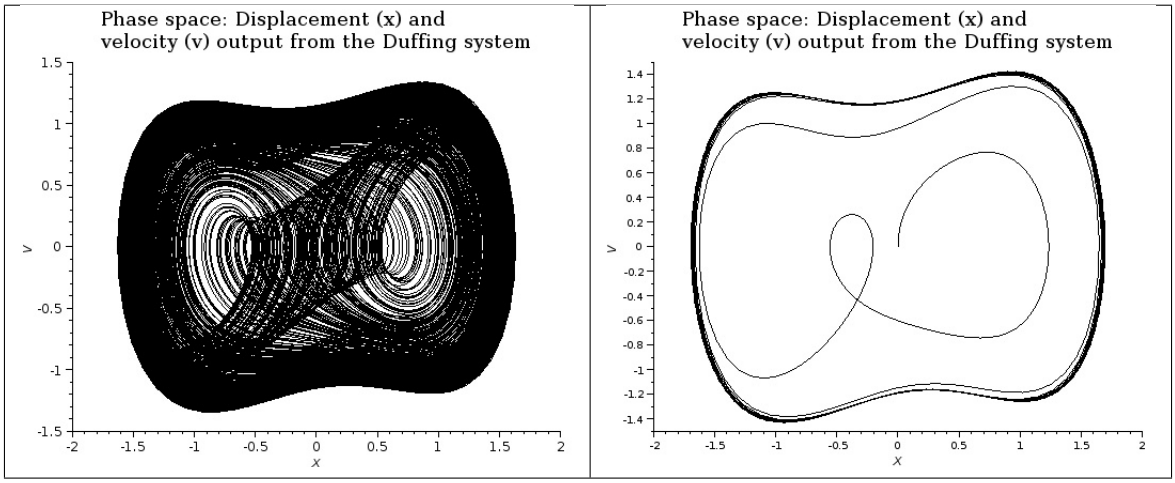

Figure 5.1: The two phase space states for the Duffing system; LEFT: with no periodic input, the system is in chaos. RIGHT: with a periodic input of sufficient (minimal) amplitude to cause transition to stability.

It is noted here that matched filtering is not the only approach to improving detection performance at the Duffing output. An alternative explored by some researchers is to use Lyapunov exponents as the detector stage [93, 97, 99]. The first or largest Lyapunov exponent is a widely accepted indicator of the onset of chaos (noting that noisy systems can generate ambiguous values). The Lyapunov exponent is a measure of the average rate of divergence between two adjacent trajectories in phase space. The assumption is that a large rate is associated with quickly diverging paths and therefore indicative of chaos (see for example Figure 4.1), and a slow or negative divergence indicates a probable stable trajectory or limit cycle, or at least the absence of chaos. The known susceptibility of Lyapunov exponents to noise is the main reason for rejecting the use of this approach in the analyses described in this thesis. However, a comparison of detection performance for the Lyapunov and matched filter methods is noted as potential future work.

5.2.5 Phase behaviour

The discussions in Chapter 4 only considered simulated input where the periodic component of the input was fully controllable and the phase difference between the input sine wave and the Duffing 'internal' sine wave was always set to zero. The impact of the unknown phase difference between an unknown input signal and the internal periodic control is investigated in this section. A modification to the nonlinear pre-processing was developed and implemented prior to detection processing, into the analyses models, to mitigate the unknown phase difference problem.

The Duffing system will only transition to the stable state when the total periodic forcing amplitude A_T equals or exceeds the minimum necessary. Considering a trivial case where the phase difference ϕ has a constant fixed value and there is no noise. The total amplitude is found from the two periodic forcing terms of equal frequency as follows:

$$A_T = \gamma_c \cos(\omega t) + A \cos(\omega t + \phi)$$

When $\phi = 0$ the two forces are in phase the system will transition, in accordance with the definitions of critical internal amplitude γ_c and provided $A \geqslant A_m$ discussed in Section 4.2.3. When the phase difference $\phi = \pi$ no transition can occur. As ϕ increases from zero to π, the precise value at which transition fails and the system remains in chaotic motion, is weakly dependent on how much A exceeds A_m. With no transition the probability of detection reduces to that of the toss of a fair coin. The problem is further complicated by the fact that for a real signal the phase difference may not be constant over time.

When the frequencies of the two sinusoidal terms are different then the behaviour of intermittent chaos emerges, which results in a small finite bandwidth associated with the Duffing pre-processor. Bandwidth and intermittent chaos were first introduced in Sections 4.3.3 and 4.3.2. However, the impact of the bandwidth of an individual pre-processor stage will be an important consideration during the construction of an

array of Duffing pre-processors, which is demonstrated in Section 5.6. Consequently bandwidth is re-visited in Section 5.5 below where an appropriate definition is developed followed by a measurement of its size for the Duffing system.

To enable detection of real signals for a wide range of possible phase differences a simple mitigation was implemented consisting of four uncoupled paralleled Duffing systems, each with one of the following starting phases for the internal periodic force term $\left\{\phi : 0, \frac{\pi}{2}, \pi, \frac{3\pi}{2}\right\}$. The four-phase approach is clearly a crude solution to the problem of unknown and possibly, varying input phase. Finding a more elegant strategy, robust to computational load, accuracy and type of input signal, is left to future research.

5.2.6 The complete processing chain

The complete detection system based on four Duffing nonlinear pre-filters each of different phase, and the separate replica correlation generating Duffing, can now be summarised as shown in Figure 5.2.

Some additional explanation of Figure 5.2 is required including aspects of the coded implementation used in the analyses described later in in this chapter. The strategy is to find the maximum value from the convolution of the input signal time-series with a time-series replica of the noise free sine wave required to be detected. Convolution of two time-series signals in the time domain is equivalent to multiplying the FFT of one signal with the complex conjugate of the second and finding the inverse fast Fourier transform of the result. It is that equivalent calculation, that is referred to as correlation in the frequency domain, in this chapter.

Five parallel branches to the processing chain are shown in Figure 5.2. Four represent the equi-spaced four-phase processing and the fifth (at the bottom of the diagram) represents the noise free replica generating function. The amplitude of the single periodic forcing term used in the replica generator becomes a system configuration

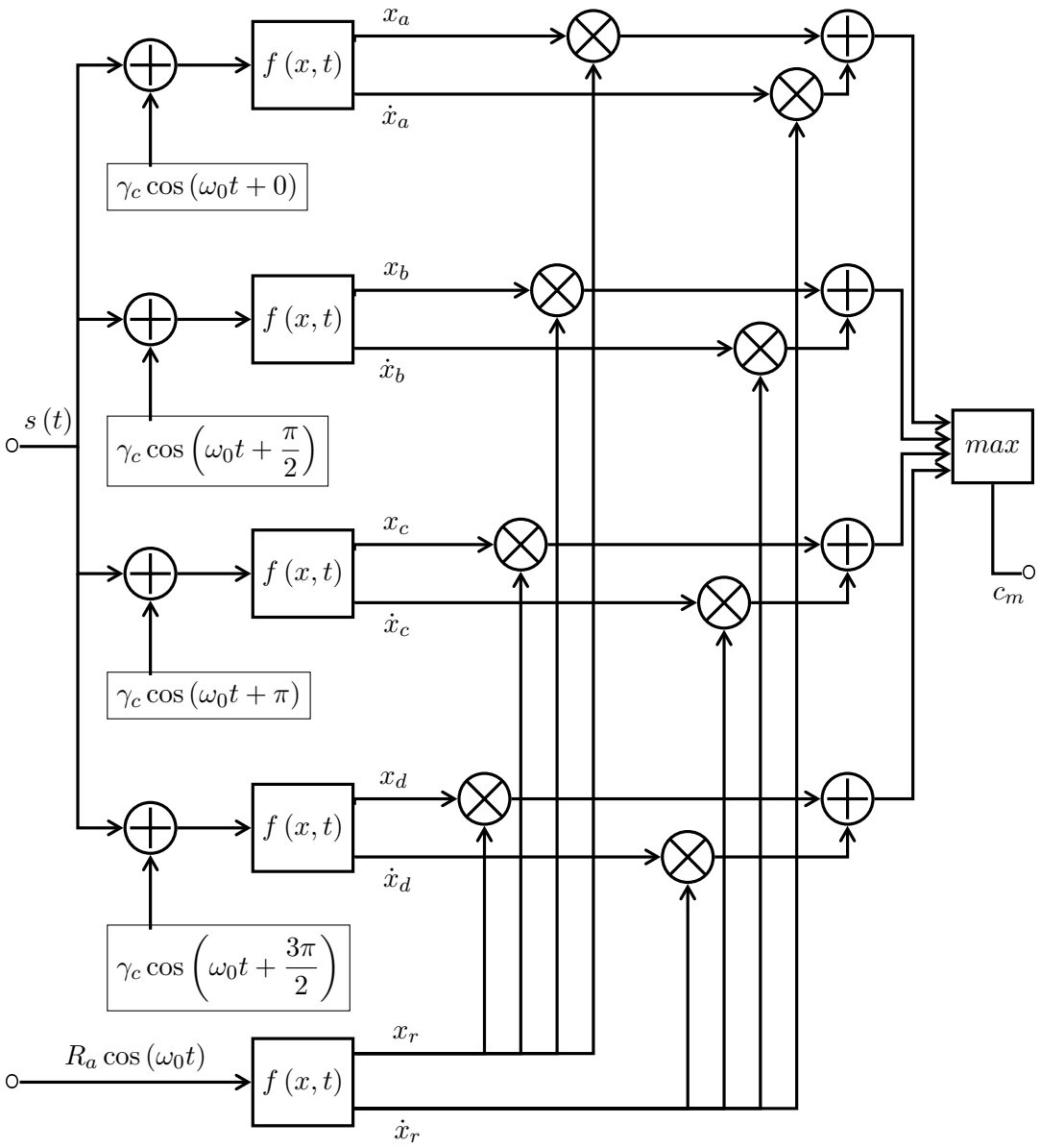

Figure 5.2: Signal processing path: Note that all outputs $\{x_a, x_b, x_c, x_d\}$ and $\{\dot{x}_a, \dot{x}_b, \dot{x}_c, \dot{x}_d\}$ are zero padded. The $\bigotimes$ symbol represents cross correlation in the frequency domain. The input data is represented by $s(t)$ where $s(n) = A\cos(\omega t) + n(t)$ (wanted signal component plus a noise term).

parameter, and is set to any fixed value guaranteed to cause transition to the limit cycle. In most cases examined in this chapter the replica amplitude is set to $A = 1.0$ unless otherwise stated. Note this approach is valid for the normalised version of the Duffing oscillator, used throughout this chapter. The displacement and velocity time-series replicas are both generated (and shown in the figure).

The input signal is represented by $s(t)$ and is assumed to be an additive combination of one or more noise terms plus a periodic component for real input signals. $s(t)$ corresponds to a short-hand representation of the input forcing components shown in Equation (4.2). Another short-hand is used to represent the Duffing system, $f(x, t)$, which is numerically solved in all examples in this chapter using the standard (canonical) RK4. The solution produces two time-series' outputs corresponding to displacement (x) and velocity ($\dot{x}$).

The replica generating function incorporated into the coded analyses models is implemented to allow user selection of the whole number of replica cycles to be used in the correlation. The strategy is select a low number of cycles so that the replica is always significantly shorter (in the time domain) than the signal. Correlation occurs in the frequency domain in the following steps:

- Truncate both replicas to the pre-set number of required replica periodic cycles
- Zero-pad all eight solutions (four velocity and four displacement).
  Zero-padding is used both at the front and the back of each solution time series, both to the same length as the original data length. The resulting eight time series' are now each about three times their original length
- Zero-pad both replicas to the same overall length as the zero-padded Duffing output data lengths. The replica should also be padded front and back.
- Fast Fourier transform eight solutions and two replicas
- Find complex conjugates of both FFT'd replicas

- Find the element-wise product of each transformed displacement solution vector, with the transformed conjugated single displacement replica vector
- Similarly, find the element-wise product of each transformed velocity solution vector, with the transformed conjugated single velocity replica vector
- Find absolute of the Inverse FFT of the four displacement element wise product data vectors
- Find absolute of the Inverse FFT of the four velocity element-wise product data vectors
- Normalise all the resulting correlation functions' coefficients, by the length (number of points) of the truncated replica *without* the additional zero padding
- Find the maximum single scalar value from the eight resulting correlation functions' coefficients

Zero-padding is required to reduce the likelihood of errors in the correlation output. Correlation is a shift-multiply-and-sum process producing one coefficient at each shift. The process wraps the end sample back to the beginning to complete the shift sequence. Zero-padding ensures the basic resolution of any signal is revealed so that the calculated correlation coefficient is accurate.

The frequency bandwidth of a single Duffing was discussed in the previous chapter in Section 4.3.3, where the qualitative discussion hinted at the possibility that a single Duffing oscillator used as a transition pre-processor may have a relatively narrow bandwidth. A method of performing detection over a very wide bandwidth using a bank or array of Duffing oscillators is investigated later in this chapter in Section 5.6. In fact the entire structure shown in Figure 5.2 will be used as a single pre-processing element in the array, where each element is configured for a different (incremental) frequency. It is more convenient to use a label for the complicated array element

structure, in the rest of this thesis it will be referred to as a Duffing Array Element (DAE). Before the array of DAE's is demonstrated however, it is necessary to understand the impact on detection performance, and this is briefly investigated in the next section.

5.3 Performance of the modified detector

There are two broad concepts that have been introduced in this chapter so far; improving the detection stage by exploiting behaviours specific to the nonlinear system, and the walk towards a system that can detect real signals. Both aspects introduce a number of new parameters, each of which could affect detection performance. The overall aim of this section is to isolate and compare the impact of these parameters. A brief summary of each assessment step is given below:

The four-phase mitigation was developed for a detector of real signals where no prior knowledge of the phase behaviour would be known. Four-phase processing will be used in conjunction with the replica correlation process, and its performance will be compared in two ways; four-phase to one-phase, and DAE with four-phase to the conventional fixed frequency bin FFT and threshold detector with no phase processing. The phase difference was randomised in this analysis, the investigation is described in Section 5.3.1.

The comparative performance at different input S/N's was shown to vary for the impulsive noise case, in the previous chapter. Some of the comparisons investigated here will also be carried out at different S/N regimes. The main place this analysis occur is in Section 5.3.2.

The correlation part of the detection stage will be isolated from the four-phase stage, and its performance compared to the same benchmark detection process that has been used in previous chapters, the FFT with amplitude detection threshold. Four-phase processing will still be used, but it will also be applied to the linear FFT

with amplitude detection scheme. In other words the 'isolation' of the correlation process is not achieved by removing the four-phase component from the DAE, but by adding a four-phase stage to the comparator detection scheme. This analysis is carried out in Section 5.3.3.

5.3.1 Benchmarking a single DAE

A method of detecting sine wave signals suitable for a realistic situation was developed in the preceding sections, however before applying it to real data some assessment of the behaviour of a DAE is required. The DAE method incorporates additional signal processing designed to improve detection performance as much as possible, by exploiting the output harmonic content as well as the fundamental and by managing the problem of unknown input signal phase. The expected improvement in detection performance, resulting from these changes, can now be quantified using ROC analysis.

The essential variable in the analysis in this section is that the phase difference between the input sine wave and internal drive is randomised between ROC iterations. The approach is to compare the ROC curves derived from the DAE system configured with and without, the four-phase scheme. Replica correlation was used in both these cases. ROC analysis was carried out on the output from one DAE. The statistics were collected in the same way as in previous ROC analyses, except here the maximum correlation coefficient is collected instead of the amplitude of the output displacement. The final step in the DAE processing is to select the maximum correlation coefficient from the four phase branches of the process. The second case, with replica correlation but without four-phase, is configured by forcing the collection of the coefficient from the same phase branch at each ROC iteration.

The input signal is simulated Gaussian white noise with an additive single tone sine wave of fixed amplitude. The sine wave part of the input signal is generated using fixed phase. The simulation of a signal with unknown phase is simulated by randomly varying the phase of the internal forcing term instead. This method was adopted

because it was easier to vary the internal drive phase, than the input sine wave phase in the coded implementation of the DAE and RK4 solver model used here. This is safe to do because the important parameter is the relative phase between the two linearly additive periodic force terms. Fixing the phase of one and varying the other is identical to the converse. In addition to the baseline configuration, the extra set up values used here for the DAE are shown in Table 5.1. Simulating randomised phase in the input data is one step towards a more stressing test of nonlinear detection algorithms, by approximating the assumed behaviour of real signals with unknown starting phase

An additional comparison was also made by collecting ROC statistics on the conventional detection scheme that uses the amplitude data in a fixed frequency bin, which is the same method used in all ROC analyses of all previous chapters. The output from a single Duffing oscillator is Fourier transformed, and the same input data used as described above. Also as earlier, the essential variable is that the phase difference was randomised over the ROC iterations. It is recognised this is not strictly a like for like comparison because the detection performance resulting from using the *a priori* knowledge of the correct frequency is artificially high. However, if the replica correlation method provides a detection performance better than this fixed bin detection threshold method, then it will also therefore be better than a more representative amplitude threshold detection method. The single Duffing system used here was also in baseline configuration. All three ROC curves; four-phase, one-phase and amplitude threshold, are shown in Figure 5.3. All three data sets were collected using the same input S/N, quoted in the figure as a calculated value (rather than measured) using $10\log_{10}\left(A_m^2/\sigma^2\right)$.

Figure 5.3 shows the ROC curve for the replica correlation with four-phase detection scheme, is both symmetrical and in a higher position than the other curves. Both of the other two cases fail to manage the randomised phase variation, the four-phase

Parameter	Symbol	Value
phase difference	ϕ	**randomised**
Runge-Kutta step	h	0.000093
Drive frequency		617.7
Input frequency		617.7
Sample rate		6000
Number of initial points		1000
ROC iterations		1600
Noise deviation	σ	0.1131648
Sine wave amplitude (minimum)	A_m	0.0201
Replica: Number of cycles		15
Replica: Internal force amplitude	γ	1.0

Table 5.1: Duffing oscillator and DAE configured with the benchmark set up. Some additional configuration values are shown here.

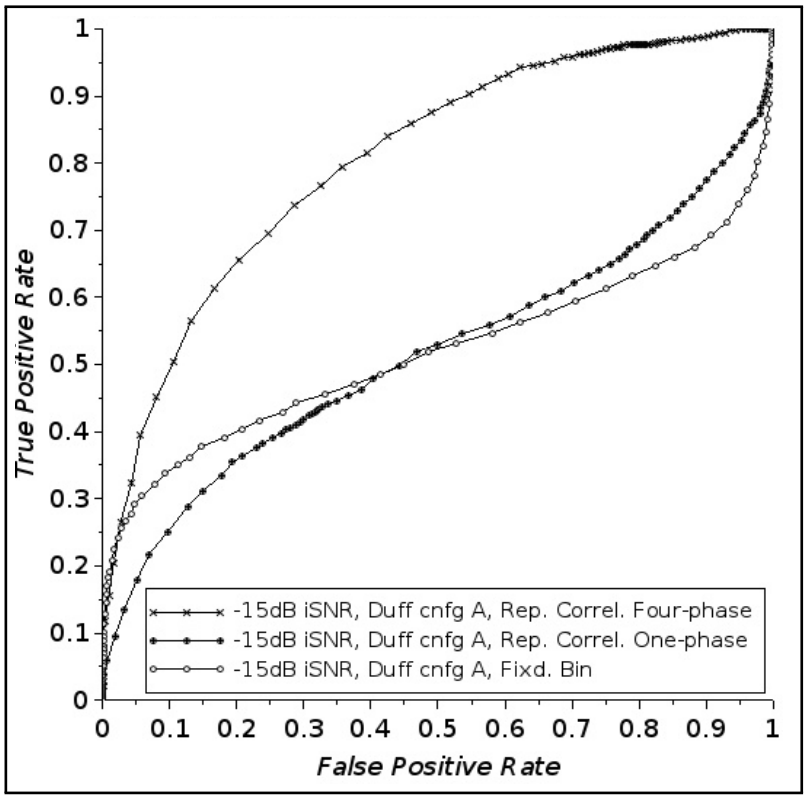

Figure 5.3: ROC curves comparing the four-phase replica correlation approach to one-phase replica correlation, and the fixed frequency bin amplitude threshold method. Duffing baseline configuration used with additional set up values shown in Table 5.1. Phase difference was randomised.

approach shows some success. The asymmetry of the ROC curves results from the bimodal distribution of the output from the detector with Duffing (or DAE) pre-processing. The two peak positions occur either side of the noise-only mean position. With one-phase processing the two peaks are of similar size, with four-phase processing the lower peak is greatly reduced. The 'S' shaped ROC curves are generated by applying a binary decision threshold to bimodal distribution functions. As the bimodal structure becomes dominated by the signal-plus-noise higher peak, as in the four-phase case, the ROC asymmetry disappears.

5.3.2 Variation with S/N

It was shown in the previous chapter that the performance of a detector using Duffing pre-processing relative to a conventional benchmark detection scheme, can vary for different input S/N. Although the evidence was collected during the investigation of impulsive noise, it is sufficient motivation to establish whether such a variation might exist under different conditions. Following on from the previous section, a second investigation of the replica correlation process using simulated input data comprising of a sine wave and Gaussian white noise was carried out. However, in this test the phase difference between the input sine wave and the internal drive was not randomised but fixed at zero. The comparison was made between one DAE pre-processor with replica correlation, and amplitude threshold detection on the output of a single Duffing oscillator. This comparison was carried out at two input SNR values -13dB and -17dB (using SNR $= 10\log_{10}\left(A_m^2/\sigma^2\right)$).

All configurations were as for the baseline set up, with the additional configurations shown in Table 5.1, with the exception that the two input SNR values were obtained by setting the input Gaussian noise deviation value to $\sigma = 0.2536449$ and 0.5060880 respectively. Importantly, the phase difference was not as shown in Table 5.1 randomised but fixed at zero. The four-phase processing was dropped and one-phase processing used instead, for both the DAE and the single Duffing oscillator. The aim

here is not to measure the performance under the conditions of 'realism', but to control the parameters and test variations with input S/N. The resulting four ROC curves are shown in Figure 5.4.

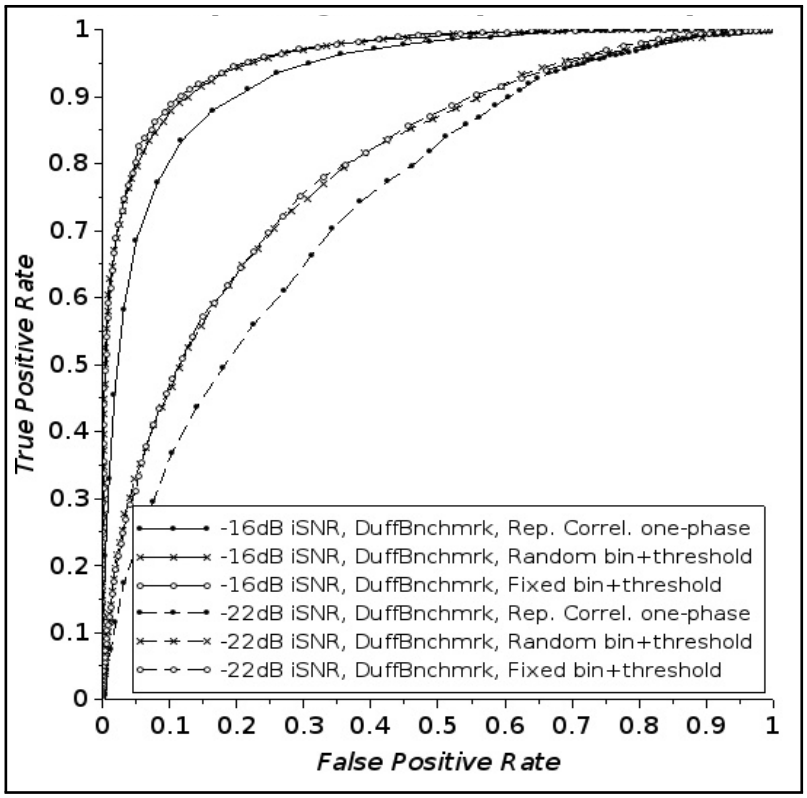

Figure 5.4: ROC curves comparing the replica correlation detection, to the amplitude threshold detection scheme. Comparison carried out at two input SNR values; −16dB and −22dB. Three curves sets at each S/N: Correlation detection with one-phase fixed, amplitude detection with fixed frequency bin and maximum amplitude detection. Phase difference ϕ fixed at zero, 2600 iterations for each ROC curve, frequency of input sine wave and internal force sine wave are both $f = 625.6$Hz, 0.075 seconds of input data at a sample rate of 1600 samples per second.

5.3.3 Benchmarking the correlation process

The aim of the final performance assessment section is to make a partial return to 'realism' by configuring the input with randomised phase difference but retain the fixed bin in the FFT with threshold detection scheme. In other words no prior knowledge of the phase of an input sine wave is assumed, but prior knowledge of the

frequency is known. The essential change in this section is to add four-phase precessing to the FFT and threshold detection scheme, by constructing four parallel single Duffing oscillators with equi-spaced phases. A comparison is made between this set up and the DAE set up. Since both use four-phase processing this is effectively an investigation of the isolated correlation process alone.

The approach is to use ROC analysis at the output of the detection stage as before. A simulated single tone (with and without Gaussian noise) is used as the input to the Duffing system, followed by the detector stage applied to the output from the Duffing system. ROC measurements were collected for four separate runs each with a different input signal to noise ratio. The four runs were repeated for the two detection configurations, the measured parameters being amplitude (in the frequency domain) in one set of runs and correlation coefficient for the other set. In both cases the phase of the input tone was randomly varied with a uniform distribution, relative to that of the 'internal' periodic force tone.

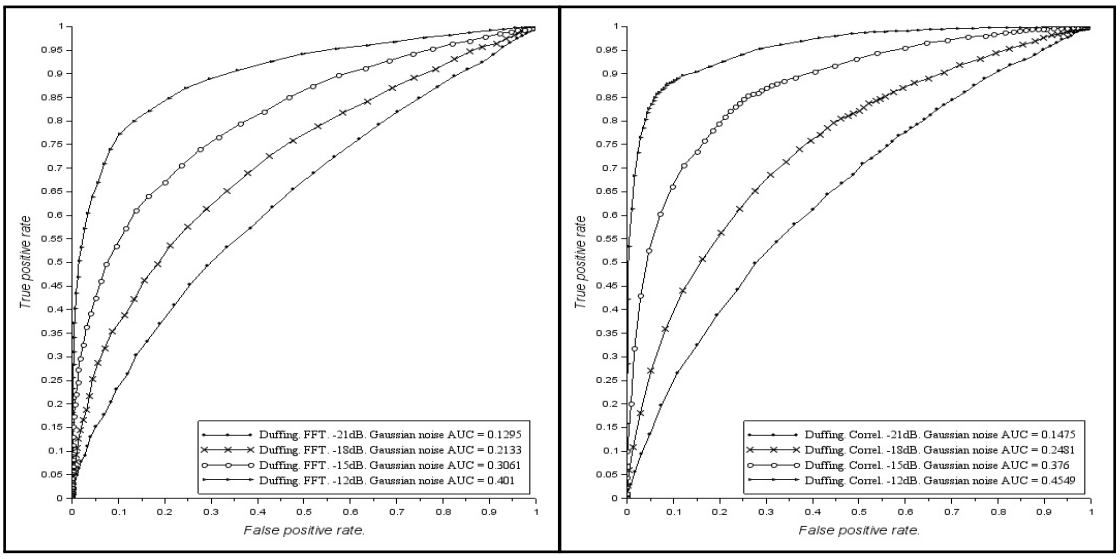

(a) (b)

Figure 5.5: Duffing ROC analysis at four S/N's and two detection schemes: (a): FFT with threshold, and four-phase processing. (b): Replica correlation, and four-phase processing.

It is immediately apparent the ROC analysis comparing frequency domain amplitude thresholding to maximal correlation coefficient detection, at the output of the Duffing system, that the replica correlation detection method provides a better detection performance. This is based on the calculated half area under ROC curve values shown in Figure 5.5. As stated earlier, note that a single measure such as area under ROC curve should be used with caution, because the performance region of most significance is often the very low false positive rates (FPR) and the ROC curves themselves may not necessarily be symmetrical. However, most of the remaining analyses presented in this chapter will be on the basis that replica correlation is used as the detector at the output of the nonlinear system.

5.4 Short input data lengths

If a practical implementation of a Duffing detector uses buffered data segments at both input and output then it is reasonable to ask how short can the data section input be and what is the relation between buffer length and detection performance. The assertion that the detection performance of a Duffing system does not reduce with reducing input data length but that of a conventional matched filter does [20], was mentioned earlier in Section 4.2. The behaviour of the Duffing as a detector of very short input data lengths is briefly investigated here, simply by providing a sequence of output time series and phase space plot pairs as the input signal $A\cos(2\pi ft + \phi)$ data length is shortened.

The sequence of phase space plots shown in Figure 5.6 indicate that in this simple demonstration at least, the transition to the stable limit cycle is unaffected by the shortening input data length until it becomes shorter than the initial transient length inherent in the Duffing system.

The output displacement solution from a Duffing system almost always starts with an initial chaotic transient sequence before attaining the limit cycle and stable periodic

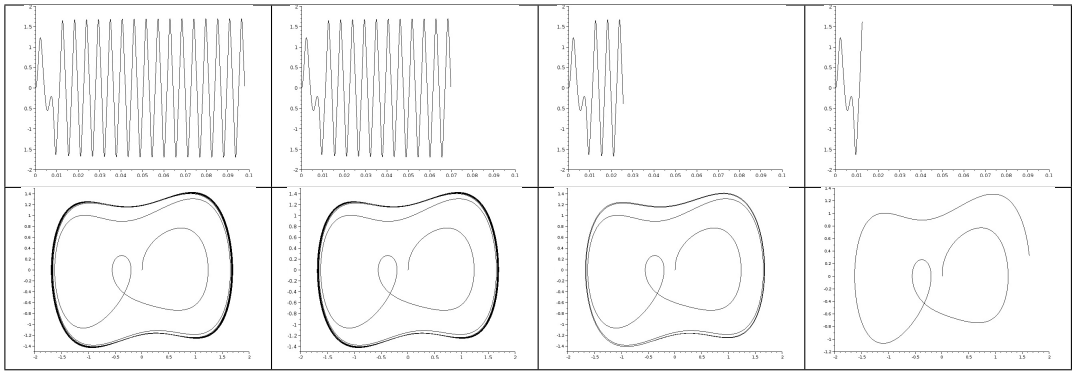

Figure 5.6: The evolution of Duffing output; phase space (BOTTOM ROW) and time series (TOP), with shortening input sinusoid signal data length (zero noise). All Duffing configuration values are as the baseline in Table 4.1 except the following: The input signal and internal drive frequency were both 179 Hz, the input data lengths (number of points) took one of four values $[704, 503, 184, 90]$ corresponding to the four plot pairs shown. The sample rate was set at 7200 Hz.

dynamics. For a given configuration and initial conditions the length of the transient does not change significantly between repeated simulations. As the output data length shortens, the proportion of the output time-series solution that is periodic becomes smaller, with the consequence that detection performance must degrade because effectively there is no stable signal. The problem can be solved by discarding the initial transient. It was shown in Chapter 4 that the transient length is predictable. A practical detection scheme can therefore exploit this to discard an optimal length of the initial transient without requiring prior knowledge of the input signal.

Parameter	Symbol	Value (short input)	Value (long input)
Runge-Kutta step	h	0.00004	0.00004
Drive frequency		647.03741	647.03741
Input frequency		647.03741	647.03741
Sample rate		18533	18533
Number of initial points		300	800
Noise deviation	σ	0.0799247	0.0799247
Initial transient points discarded		80	120
FFT only ROC: peak track or fixed bin		fixed	fixed

Table 5.2: Duffing parameter configuration values used in the ROC analysis in this section.

The impact of transient discard can be assessed using ROC analysis. A single DAE was configured as a baseline system, with some additional set up parameters as shown in Table 5.2. Two input data lengths were considered, each with a different amount of the initial transient discarded. ROC curve data were collected to form a comparison between correlation detection using four-phase processing in one DAE with a short input, with and without discard. A third curve representing the FFT and threshold detection scheme was also generated. The same method was then repeated to create a second set of three ROC curves, this time using a longer input data length. The results are shown in Figure 5.7.

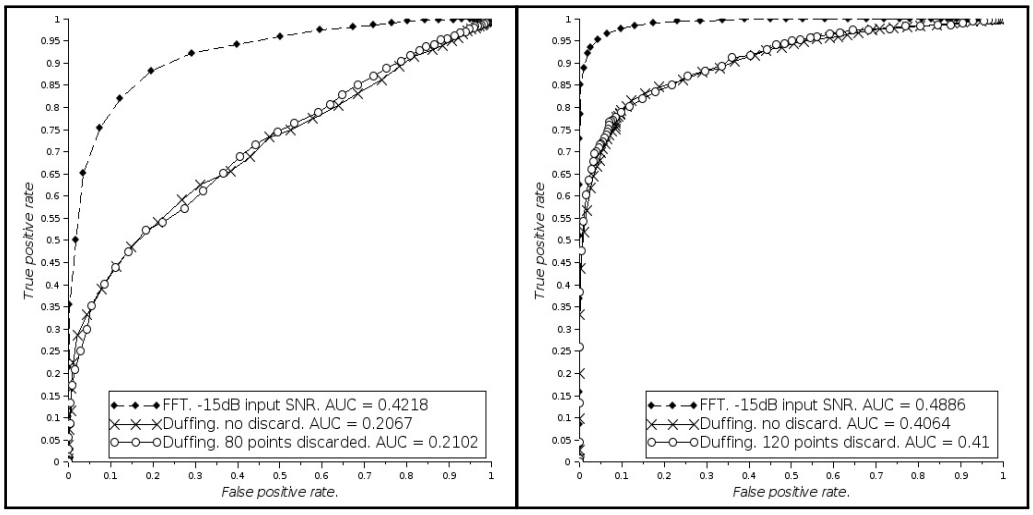

(a) (b)

Figure 5.7: ROC analysis for one DAE: With and without initial transient discard, replica correlation detection using maximal output, compared to FFT and threshold detection. Using either very short input length (300 data points of single tone and additive Gaussian noise), or long input (800 points). All curves at -15 dB input SNR. The ROC curves for FFT detection use the same input data length and S/N. (a): Maximal correlation with and without discard compared to FFT. Short input. (b): Maximal correlation with and without discard compared to FFT. Long input.

The conclusion that can be drawn from the results shown in Figure 5.7 is that the effect on detection performance of discarding the initial transient is almost insignificant, under the conditions of the investigation carried out in this section. However, if the ratio of transient length to input data total length were to be larger

than the $\sim 1/3$ used here, the outcome may be different.

5.5 Quantifying bandwidth

The bandwidth of the Duffing pre-processor can be measured, both for a single Duffing oscillator and for an array of DAE's. It is important to emphasise here that the objective of this section is not to fully characterise all aspects of the behaviours of a nonlinear pre-processing scheme that affect bandwidth. The main purpose is to find a reasonable estimate of the bandwidth in order to understand some of the issues associated with an array of Duffing pre-processing units, that will be discussed later in Sections 5.6 to 5.6.2.

The bandwidth of a single Duffing oscillator, and one DAE, forced by one internal periodic component and two external components that represent the input signal model of noise and sine wave, is primarily determined by two factors. These are the behaviour of intermittent chaos as the frequencies of the two periodic force terms become further apart, and the length of the time-series input discrete data segment. Two sets of bandwidth measurement data were collected, one for a 'short' input signal length and one for a 'long' input.

A single Duffing oscillator was set up with the baseline configuration. The input signal was configured with an arbitrarily high S/N, the noise deviation set constant for all runs, at $\ll 0.00003$. The strategy was to apply positive increments of the input sine wave frequency, in steps of 0.1Hz, starting at the same frequency as the internal drive. The corrected output power spectral density was found and the peak power value collected at the internal drive frequency bin, for each frequency increment of the input signal frequency. Internal drive frequency, critical internal amplitude and input sine wave amplitude were all held constant, at $f_0 = 305.1265$Hz, $\gamma_c = 0.812$ and $A = 0.04$. Phase difference between input and internal sine waves was fixed constant at zero. The sample rate for these tests was set very high at 26613, so that there were

more than 70 samples per cycle at the highest input frequency increment, to eliminate any possibility of output amplitude 'roll off' as the aliasing, or Nyquist, frequency is approached. The results are shown in Figure 5.8 (a).

A second bandwidth set of measurements were then made, replacing the single Duffing oscillator with one DAE. The DAE was configured in the same way as the single oscillator, with the additional set up values of; number of replica cycles 15, fixed replica amplitude 0.84. The input signal was the same as before. The variation of output correlation coefficient with difference frequency was measured, at two different input data lengths. The first data length corresponds to the short length of 0.75 seconds used in the previous test. The length of the second data set was set even shorter at 0.057 seconds. The results are shown in Figure 5.8 (b).

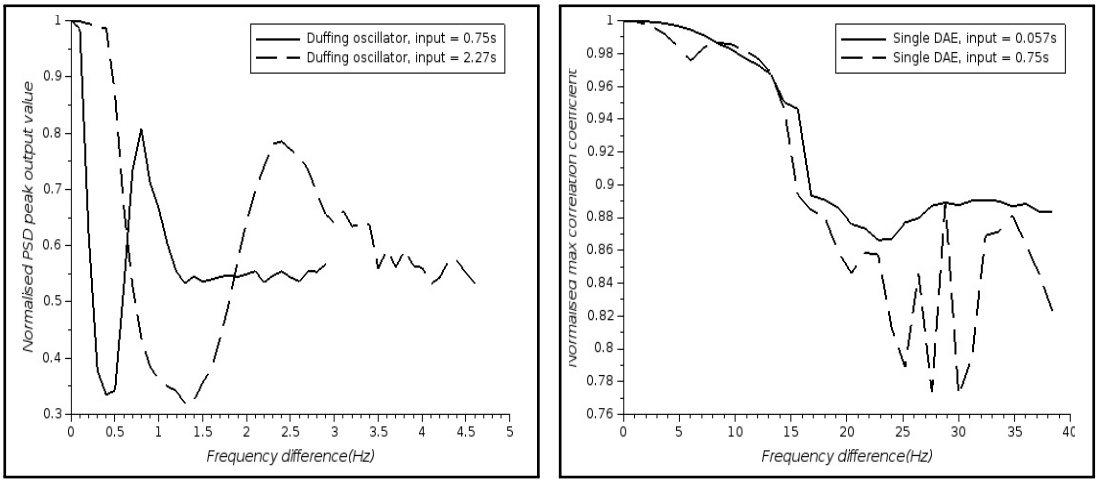

(a) (b)

Figure 5.8: Half sided bandwidth estimation. (a) A single Duffing oscillator, maximal PSD peak power variation with frequency difference, at two input data lengths: 2.27 seconds and 0.75 seconds. (b) A single DAE, maximal replica correlation coefficient from DAE four-phase processing, at two input data lengths: 0.75 seconds and 0.057 seconds.

Figure 5.8 shows that the output detection (measured) parameter, which is either maximum PSD value or maximal correlation coefficient value, reduces as the difference frequency increases from zero. The reduction has cyclic structure in all

cases, similar to an under-damped sine wave, however the cyclic structure is much more marked for the single Duffing oscillator. The reduction appears to eventually reach a semi-stable plateau; at an approximate factor of 0.55 of the peak in plot (a) the single Duffing oscillator, and approximately 0.86 of the peak for the DAE. Bandwidth is traditionally measured at the half power (or half amplitude) points, however Figure 5.8 (a) and (b) show this metric is not meaningful because the half power points are not reached. An alternative bandwidth definition point is selected here, such that all plots achieve the level, and it is higher than any side-peak values in all cases. The arbitrary factor of 0.9 of the main peak is chosen as the bandwidth definition point for the estimates used in this thesis.

Two important observations from Figure 5.8 are noted here. Firstly, the bandwidth does not appear to change significantly with input data length for a single DAE, however for a basic Duffing oscillator bandwidth increases with increasing input data length. Secondly, the bandwidth, for a given input data length, is much larger for a DAE compared to that of a single Duffing. For 0.75 seconds of input data, the DAE has a bandwidth at the 0.9 point of ~ 34 Hz compared to one basic oscillator, which has a bandwidth of ~ 0.4 Hz.

The nature of intermittent chaos in terms of its characterising metrics such as amplitude and intermittent period, is not affected by the subsequent detection processing. The choice of the subsequent detection scheme, such as replica correlation or amplitude thresholding, can not have any effect on the nature of the time-series passed into it. Such a time-series, exhibiting intermittent chaos, will do so irrespective of the detection scheme. Therefore the different bandwidths for identical length and S/N input data, measured using the two detection methods, must be partly determined by the detection processing itself.

5.6 An array of nonlinear detectors

A practical detection system will need to cover a wide frequency spectrum, however it has been shown that a single Duffing oscillator system using the transition mechanism has a very narrow bandwidth. It is possible to make a time-frequency like spectrogram visualisation of an output signal from an array of Duffing oscillator detectors, each with a fixed internal force frequency that is incremental across the desired spectrum. The idea was first proposed in 1999 [4], and then implemented by Bermudez-Gomez *et al.* in 2012 [118]. Bermudez-Gomez *et al.* demonstrate the technique and make a comparison to other conventional spectrographic techniques such as the short time Fourier transform. However no comprehensive characterisation or performance measure was made. In this section the technique is extended to realistic and stressing signals and some of the behaviours of an array are investigated and discussed. The concept is further extended by constructing the array using multiple DAE's rather than basic Duffing oscillators. Significantly fewer elements are needed, which reduces the computation time.

The effective bandwidth of a single Duffing oscillator is governed by the difference in frequency between the internal force term and the input. The onset of intermittent chaos, and the pre-selected and fixed input data length can combined to vary the bandwidth significantly. However, even though a shortened fixed length time-series could potentially hide intermittent behaviour by having a stable periodicity shorter than the onset time, as the difference frequency increases intermittency will occur earlier and re-appear within the same data length. However it is possible this advantage may not manifest if there is a variable and unknown phase difference between any input sine wave and the internal drive.

Even if an attempt were made to exploit the difference frequency (beat frequency) itself by developing difference frequency ('demodulation') detection processing to fine-tune the classification of the actual frequency of the unknown input signal, a

single ‘wider-band’ Duffing oscillator will eventually fail. As the difference frequency grows still larger the periods of stability become shorter and eventually degrade altogether, often well before their time length becomes similar to the inverse of the internal drive frequency. The conclusion is that an array comprised of basic Duffing oscillator systems is unlikely to perform well as a wide band detector across the range of frequencies that would be required in a practical detection system.

It was shown earlier that the bandwidth of the DAE appears to be constant with input data length, and generally much wider than the bandwidth of a single Duffing oscillator. The replica correlation with four-phase processing has a bandwidth at its output of about 34 Hz as compared to about 0.4 Hz measured for the same input data length. The computational load of Duffing pre-processing and detection is estimated to be about one fifth that of one DAE, because the Duffing solver forms the majority of the load and there are five solvers operating in one DAE processing scheme. However, a factor of about 85 times the number of single oscillators would be required to cover the same given bandwidth as an array using DAE’s. An estimated computational load approximately $10 - 17$ times faster should be expected using DAE’s, compared to single oscillators.

Based on the preceding arguments an array of normalised Duffing DAE’s was constructed, with the internal periodic force term in each DAE incrementing in constant frequency steps. So far the discussion has concentrated on the frequency bandwidth of each element, along the frequency axis of the time-frequency visualisation. It was shown in Section 5.4 that very short input data lengths still successfully trigger a Duffing oscillator to transition to the stable limit cycle. Consequently very short input data lengths can be used as an investigation tool in an array of DAE, therefore two further processing steps were added, placed before the input to each DAE in the array. The length of the the input time-series data was shortened and overlapped, which enables an understanding of the time axis resolution that may be attainable, without introducing ‘edge‘ artefacts between time step cells

in the final time-frequency visualisation.

Shorten-and-overlap was implemented in the coded model by cutting a long input time-series data vector into several shorter sections, where each short section contained a repeat of a proportion of the tail end of the previous section. A data matrix was then built using the sections, with each row representing one time-series section. The overlap proportion therefore became a control within the array overall configuration. The time-frequency visualisation is therefore derived from a great many time and frequency 'cells', where the cell width along the time axis is controlled by the shortened data length and the RK4 step size. The number of time cells is controlled by the number of shortened data vector rows in the data matrix. Along the frequency axis the number of frequency cells is set as a control in the array set up, and the frequency increment is implemented as frequency step parameter added to the internal drive frequency at each iteration. These two therefore combine to define the total bandwidth of the array. A copy of the same re-shaped input data matrix for the same long time period, is passed to to each DAE in the array.

Two demonstrations of the array of DAE's are presented in Figures 5.9 and 5.10, and briefly described in Sections 5.6.1 and 5.6.2 respectively. The approach taken was to perform a series of trial-and error array modelling runs where several controls were varied to generate a qualitative understanding of how the visualisation generated by the models and the array output, behaves. The amount of overlap at the input was varied from zero to about 0.8, but in general a good compromise was to use a factor of 0.66 as the proportion of overlap. The frequency step size was also investigated and found to generate clearest output for a value from 1Hz to about 40 Hz. Model run time was a major factor, and largely dictated the number of samples to be used at the input prior to re-shaping and overlap.

5.6.1 Frequency modulated chirp input

The first results shown in Figure 5.9 were generated using a simulated linear frequency modulated 'chirp', with no added simulated noise. The output across all time and frequency cells was normalised to a range of zero to unity.

Figure 5.9 demonstrates that the principle that a spectrogram style visualisation of the time-frequency behaviour of an array of Duffing based pre-processors is viable. The results in Figure 5.9 plots (b) and (d) demonstrate that the resolution in both frequency and time, cannot be increased simply by using finer frequency steps or shorter re-shaped input data chunks. The earlier bandwidth investigation showed an apparent bandwidth for one DAE, constant with input data length, of about 34Hz. Plots (b) and (d) agree well with the earlier result. Both show an apparent bandwidth of between 25 and 30Hz. Plot (a) differs from (b) and (d) in that only one-phase processing was used, an artefact pattern is clearly visible. The four-phase processing appears to destroy this pattern. The precise cause of the pattern is left to future work, however it appears to be closely linked with the phase mitigation processing and the bandwidth of the correlation detection process.

5.6.2 The *'hello'* voice data

A further more stressing demonstration of the DAE array is described in this section. The input data in this case uses a recording of a few seconds of voice data of the spoken word *'hello'*. The recording was made in a small well furnished room with little background noise and no noticeable reverberation. The recording was made using the built in sound card on a low specification laptop computer, using a very inexpensive microphone. The time series recording has not been analysed for noise content, type or S/N, however it is speculated that the noise that is present is most likely to be electrical rather than room noise, because of the inexpensive recording equipment used. Observation of the time-series showed there to be some clipping for

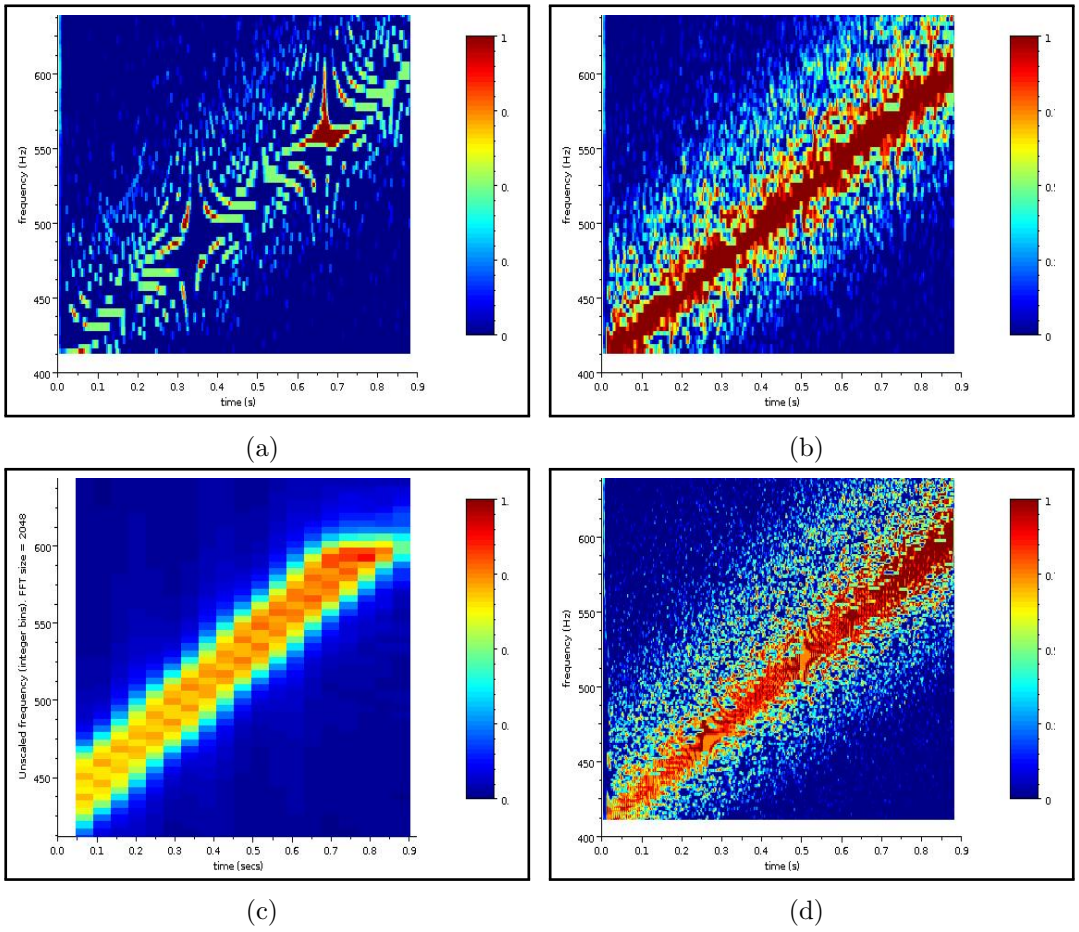

Figure 5.9: Detection of a simulated up-sweep linear chirp signal using an array of DAE's. Configuration common to all plots: Individual Duffing systems use baseline configuration, DAE shortened data length re-shaping with no overlap. Input sine wave amplitude $A = 0.026$, RK4 step 0.00008, linear chirp start frequency 406Hz. Input sample rate 9091 samples per second, input data original length 8000 samples. Plots (a), (b) and (d) use DAE array, maximal output correlation coefficient detection. (a): Without four-phase processing (one-phase). Re-shaped input chunk length 40 samples, frequency cells 80, frequency step 3Hz. (b): With four-phase processing. Re-shaped input chunk length 40 samples, frequency cells 80, frequency step 3Hz. (c): Conventional FFT time frequency spectrogram for comparison. (d): Finer frequency and time steps, with four-phase processing. Number of frequency cells 240, frequency step 1Hz, short input chunk length 20 samples.

the very loudest part of the recording, however this does not alter the outcome of the demonstration.

Figure 5.10 shows the output time-frequency visualisation results for an array of DAE's processing an input of recorded voice real data (the *hello* signal). The individual Duffing systems comprising the each DAE were configured as the baseline. The re-shaped and overlapped input data were configured so that each data row in the data matrix was 230 samples long. The findings of Section 5.4 suggested that discarding the chaotic transient had little impact on detection performance provided the ratio of transient length to the data length was $\geqslant 1/3$. This condition was not met by the set up used here, where the ratio was found to be $\backsim 1/2$. The choice was made to exploit transient discard for the demonstration shown in Figure 5.10.

Finally, the use of real data such as that used here, presented an additional problem not encountered so far in the thesis. Generally, real data will have variable amplitude or power, including any component of the input data that is the signal to be detected. It was therefore necessary to include an additional processing step before the data was passed into the array of DAE's. The overall variance of the data was measured and the overall amplitude scaled accordingly so that the signal component had an amplitude sufficient to trigger transition in the Duffing systems. In other words the aim is to scale the input so that the wanted signal has an amplitude $\geqslant A_m$. This is always going to be a trial and error process. If the S/N happens to be very low it may take several scaling attempts before the signal manifests in the Duffing array visualisation.

The configuration used in the voice data example shown above was selected on the basis of a trial-and-error approach. There are several parameters that affect the visual quality of the result including, frequency step size, RK4 step size, data matrix dimensions, overlap, replica amplitude, the coarse nature of adopting only four phase steps, the input signal scaling and the number of cycles in the limit cycle replica.

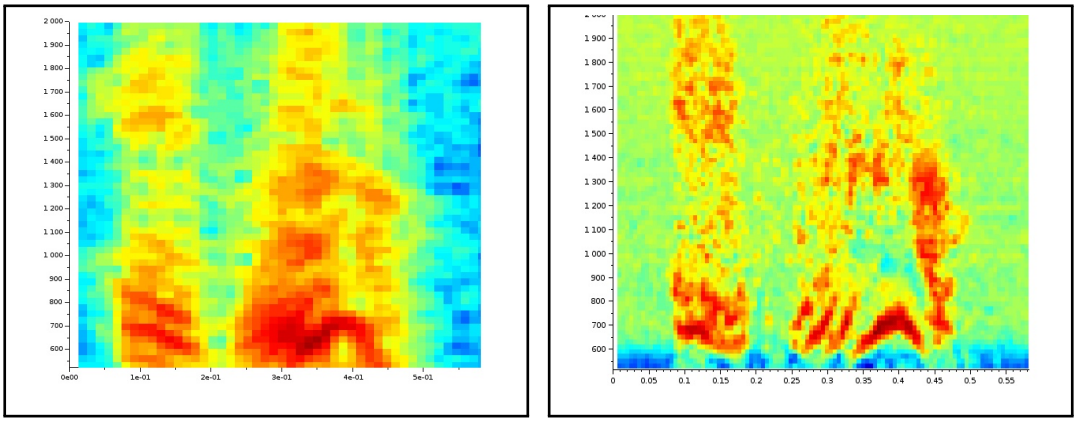

(a) (b)

Figure 5.10: One second of recorded voice data (saying the word *'hello'*), truncated to about 0.6 seconds in length. All plot axes: First TIME (seconds), second FREQUENCY (Hz) and third unscaled value for either; amplitude or correlation (a): Conventional PSD spectrogram using Hamming windowed FFT overlapped 0.666, size 1024, of the input data, $10 \times \log_{10}$ scale. (b): Array of DAE's at 25 Hz step, 200 initial transient points discarded in all time-frequency cells, time axis chunks 230, points overlapped 0.666.

The test simulations used to optimise the configuration in order to produce the figure shown above revealed a consistent problem with the method. There is severe roll off in the spectrogram at very low frequencies, which in this configuration meant no detections were seen below approximately 500Hz. There is known to be significant signal content below this frequency, in the *'hello'* voice data used here. Identifying the cause and developing a solution is left to future work, along with further investigation into the underlying factors determining the bandwidth of a DAE, and therefore the resolution of the data shown above.

It is thought that there are several mechanisms that may affect the success of the DAE array approach. These are catalogued below:

1 If the chunk of data presented to the Duffing filter is too short, the correlation fails and signal content is lost.

2 If the input sample rate is too high this requires the chunk length to much longer in order to pass enough cycles to the correlator for it to produce a meaningful value. A high sample rate therefore has a similar

effect as passing chunk of data to the correlator that is too short. Unless the chunk length is increased as the sample rate is increased, to ensure enough cycles are generated, the correlation will fail.

3 If the Runge-Kutta step size is too wide the phase space trajectories become corrupted and any meaningful output from the correlation processing breaks down.

4 A robust understanding of appropriate data compression/scaling methods needs to be developed. This is not so trivial as might be expected given the nonlinear behaviour of the spectrogram method, across the frequency axis.

5 The zero padding used in the replica correlation detection severely affects the spectrogram resolution.

6 The frequency normalised Duffing configuration renders the limit cycle trajectory size *almost* invariant with frequency. Any signal components that cause full transition could therefore potentially destroy the amplitude variation seen in the basic FFT spectrogram. The monotonic amplitude variation is potentially converted *almost* into an on/off nonlinear discontinuity.

5.7 Snapping shrimp

Much of this chapter has been devoted to building towards the construction of a practical pre-processing scheme and detection stage, that can be applied to real data. The development of a wideband version of the nonlinear pre-processing scheme, with a novel detection stage, and shown in the previous section, was successful in demonstrating the principle can work. In this final section another application to real data is discussed, here the focus is not detection over a wide frequency band but detection in the presence of loud biological noise.

A single DAE was used in the analysis here, ROC analysis was the metric used to

quantify detection performance. The input data was an additive mixture of noise and a single sine wave tone, however the noise used here is real underwater biological data taken from a wav file recording of the impulsive noise produced by a colony of snapping shrimp recorded near the Hopkins Marine Station in Monterey Bay (USA) [119]. The recording was originally made and saved as an 'aiff' file. A necessary conversion to 'wav' format, at a sample rate of 44100 samples per second per channel, was carried out after downloading because the simulation tools used here do not read 'aiff' formatted sound files.

The ROC analysis aim is to compare the detection performance of a four-phase DAE unit using correlation detection, with that of a linear FFT and amplitude threshold detector with no nonlinear pre-processing. The simulated sine wave input signal samples were added to a new section of the real snapping shrimp data samples, at each ROC iteration. The original recording is approximately 3 to 4 minutes long, which meant that short sections were able to be selected at random at each ROC iteration without repetition. The noise data were scaled separately to the added sine wave signal, in order to set a desired input S/N. In these test the SNR was set to -21dB with the sine wave signal amplitude set to the minimum detectable $A_m = 0.0201$. The randomly selected short data lengths of noise were 1500 samples long. Apart from these modifications to the ROC analysis process, the procedure is identical to that used elsewhere in this thesis. The ROC curve results from 1500 realisations are shown in Figure 5.11.

The four-phase DAE using replica correlation detection applied to highly impulsive noise is successful in detecting the added sine wave. The ROC curve for the DAE test (dashed line, cross marks) is significantly higher at low false alarm rates than the directly comparable FFT with amplitude threshold linear detection scheme at the same input S/N (solid line, cross marks). The FFT only curve is highly asymmetric, the TPR falls sharply at FPR values less than about 0.25.

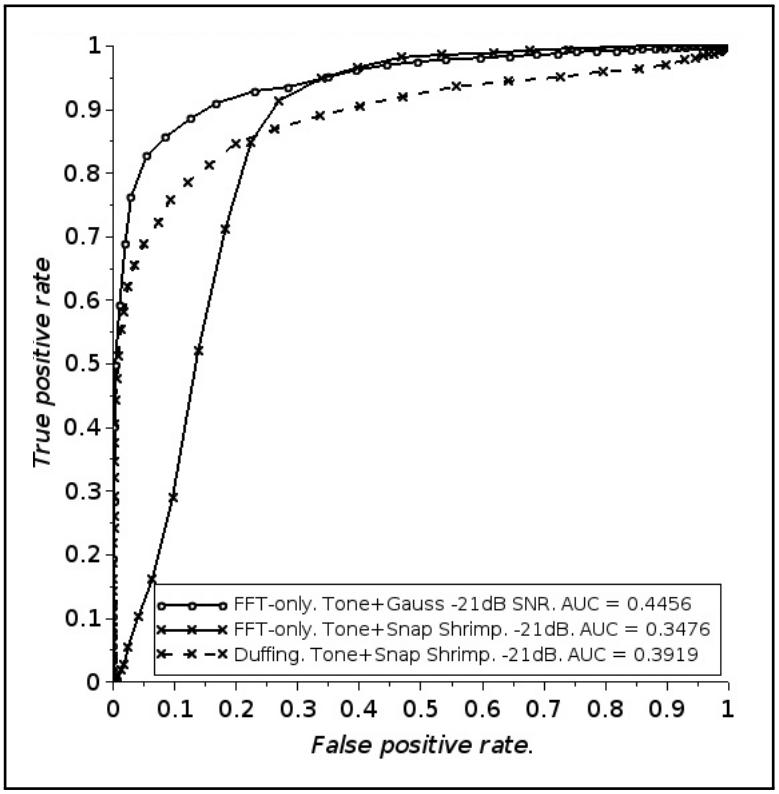

Figure 5.11: ROC curves using Monterey Bay snapping shrimp impulsive noise with an additive simulated sine wave. Two solid line curves: Basic FFT with no nonlinear pre-processing and using amplitude threshold detection. Sine wave in Gaussian white noise and sine wave in snapping shrimp impulsive noise. Dashed line ROC curve: Sine wave in snapping shrimp impulsive noise, using DAE with four-phase pre-processing and detection. RK4 solver step 0.00004, internal and input sine wave frequencies $f_0 = f = 628$Hz, internal and input sine wave amplitudes $\gamma_c = 0.812$ and $A_m = 0.0201$, replica amplitude 1.0 using 3 cycles, 200 initial transient points discarded.

It was shown earlier using a similar analysis with simulated impulsive noise and sine wave input (no real data), that the FFT only detection scheme had a symmetric ROC curve. The result that is comparable in set up to the one shown in Figure 5.11, is discussed in Section 4.6 and shown in Figure 4.16. In both cases the baseline Duffing configuration was used, however there are two main differences. Firstly, in the earlier result a single Duffing oscillator was used with amplitude threshold detection on a fixed bin in the frequency domain, whereas a full DAE unit was used for the result shown in this section. Secondly, the input impulsive noise used in the earlier result was constructed from multiple versions of the modelled finite length impulse spike,

shown in Figure 4.15 (b). Both sets of results agree in that both nonlinear pre-processing and detection schemes outperform a simple FFT based linear detection scheme. However, the disagreement between the two sets of results on the shape of the curves (asymmetrical versus symmetrical) may be because the impulse spike model is not sufficiently representative of real snapping shrimp impulse spike. More specifically, a time-series comprised of modelled spikes may be less impulsive than than the real biological data.

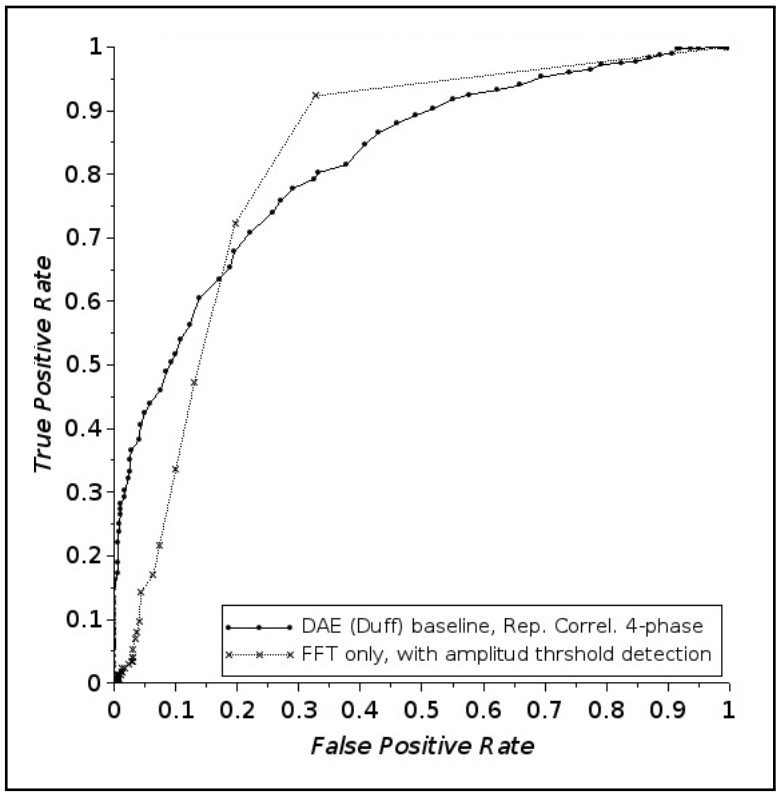

Figure 5.12: ROC curves using simulated impulsive noise with an added simulated sine wave. Dashed line curve: Basic FFT with no nonlinear pre-processing and using amplitude threshold detection. Sine wave with simulated power eleven impulse noise. Solid line ROC curve: Sine wave with simulated power eleven impulse noise, using DAE with four-phase processing and replica correlation detection. RK4 solver step 0.00004, internal and input sine wave frequencies $f_0 = f = 630.24$Hz, internal and input sine wave amplitudes $\gamma_c = 0.812$ and $A_m = 0.0201$, replica amplitude 0.84 using 15 cycles, 200 initial transient points discarded.

The proposed explanation offered above, for the difference in ROC curve shapes is explored in Figure 5.12. Here, the real biological noise data is replaced with fully simulated impulsive noise. The noise was generated by producing Gaussian white noise with a noise deviation set to 0.34, and raising the noise time-series to the eleventh power. The sine wave signal was added as before, and the combined input comprised of 5250 samples of impulsive noise and tone. The advantage of this approach is that the large excursions of each impulse spike in the input time-series are much shorter in time-length than the impulses modelled in the earlier results.

Using simulated noise that is far more impulsive than the models used in Chapter 4 produces the asymmetry in the ROC curve for the FFT only detection scheme, as shown in Figure 5.12. This evidence supports the conclusion that the more impulsive the input noise is, the worse a linear detection scheme based on FFT and amplitude thresholding, performs. As the impulsiveness increases, the performance of the linear detector falls below that of the nonlinear DAE scheme at low FPR values. It is left to future work to explore this result further to test its robustness.

5.8 Discussion

The aim of this chapter was to complete the analysis of a range of behaviours found in the Duffing transition mechanism, and to use those properties to develop a detection scheme that could be applied to real data. Some of the properties offered only marginal benefit to a practical nonlinear detector. For example, discarding the initial chaotic transient that occurs at the output from a transitioned nonlinear system, only improves performance by a small amount for extremely short output data lengths. In contrast, the nonlinear DAE system with correlation and four-phase processing has the property that its detection performance does not appear to vary significantly with an increasingly impulsive input signal. A linear system however, does appear to lose performance for highly impulsive input.

The DAE approach was found to increase the computation time, however it showed that it is possible to build a wideband array to detect sine waves and other input signals, over wide frequency bands. It is recognised that the four-phase approach is a simple solution to the problem of unknown phase at the input. There is scope to improve this aspect. A complex version of the Duffing system was chosen by Deng *et al.* [8] to form a detector of weak complex signals. Although Deng *et al.* continue the erroneous claim of noise immunity for nonlinear system detectors in their 2012 paper, this does not detract from the potential of their complex form Duffing system to provide an alternative mitigation of the problem of unknown phase of an input periodic signal. The benefit postulated in this thesis, is that as a minimum such a system could be implemented as a much faster algorithm. This is because the complex form can easily be cast as a first order system, so that two quadrature Duffing systems can be used instead of four separate Duffing oscillators, to detect the signal of unknown phase.

Chapter 6

Conclusions

6.1 Introduction

Two nonlinear mechanisms commonly found in models of nonlinear systems have been investigated for their potential to improve detection performance for a set of different types of input signal. The main goal of the work presented here was to apply nonlinear processing techniques to specific underwater acoustic detection problems, and to comprehensively and robustly measure the performance of these systems in terms of the impact on detection.

The first nonlinear mechanism examined was Stochastic Resonance (SR), which was the subject of Chapter 3. The next two chapters explored the mechanism of transition from chaos to stable motion. In both these cases, and for the first time, a comprehensive detection performance quantification was carried out using Receiver Operating Characteristics (ROC) analysis. The results of this analysis have generated the most comprehensive set of performance measures, and firmly establishes the real status of whether nonlinear systems can be usefully exploited in underwater detection problems. These results have the advantage that the quantified performances can be safely compared to any future detection performance ROC analysis, *on any type of detector* operating on the same input data. This is novel, and in contrast to the

majority of the performance measures in the literature, such as output S/N [4] or gain [25], which are poorly defined and cannot safely be used in comparisons.

6.2 Stochastic resonance

The configuration of the nonlinear system is crucial in enabling the stochastic resonance effect to manifest. It has been shown that only a part of the total configuration space available for a normalised system, will enable the resonant effect to appear. Assuming any exploitable improvement in detection performance can only reside in the stochastic resonance region then the usefulness of nonlinear systems in that respect is therefore constrained to a subset of combinations of system parameter values that generate SR.

Unfortunately there are a number of partially inter-dependent nonlinear system parameters that require adjustment to meet the conditions for SR and to optimise the detection of the wanted part of any input signal. In particular the optimal detector configuration for best performing detection using SR, depends on the input S/N, the input overall energy level (variance) and on the frequency of the wanted component. The upper bound on frequency (imposed via the Kramers rate condition) can be easily be extended however this requires adjustment of two additional system parameters, the two factors controlling the size of the linear and nonlinear displacement terms. The system is no longer normalised but is now parameter-adjusted in order to optimise the SR effect for the particular input S/N value. The optimal stochastic resonance based detector is dependent on knowledge of the input signal, which further reduces the usefulness of SR to improve detection.

An appropriately configured Langevin system stimulated by an appropriate input sine wave will become stochastically resonant provided the conditions for SR are met. These conditions were detailed in Section 2.4.3. The output is periodic with a fundamental frequency identical to the input frequency, but at some input S/N

regimes the output exhibits additional harmonics. The shape of the periodic component of the timeseries output from a nonlinear system, changes as the system's overall energy content increases past that required for SR. The shape morphs from a single sinusoid, to a summed sequence of a small number of higher frequency harmonics, and back to a sinusoid. This change offers a possible explanation for the shape of the classic SR indication, the non-monotonic output S/N curve.
Signal-to-noise ratio measured on only the fundamental frequency and ignoring the harmonics may present a falsely low S/N value in the nonlinear regime. The total signal power is divided amongst the fundamental and its harmonics. However the share of the energy retained in the fundamental varies.

It was shown in Section 3.4 that the damping factor in a Duffing system can affect the onset of SR, without changing the size of the SR peak. Higher input S/N (lower noise for the same signal amplitude) bring about SR for increased damping. This means it becomes possible to add more noise as a method of optimising the input S/N for the SR peak, where the assumed detection benefit will occur.

The detection performance was quantified for a small number of cases, using ROC analysis. The amplitude variation statistics with signal present and absent in one frequency domain bin were collected to generate the ROC curves. Comparison of the detection performance was made, with and without, the nonlinear pre-processing stage. The three cases are represented by Figures 3.7 (sinusoid in white noise), 3.9 (sinusoid in mixed white and impulsive noise) and 3.14 (square wave harmonic input in white noise).

In general the qualitative form of the variation of detection performance with decreasing input S/N, agreed with the form of the variation in output S/N from the nonlinear system. The ROC curves indicated a fall and then a rise in detection performance up to the SR peak. However even at the assumed optimum stochastic resonance, detection performance in all three test cases was significantly lower than the linear comparison case (no nonlinear pre-processing). In fact there was no

improvement found for any tested input S/N case, the greatest underperformance was found as expected at the dip in output S/N point.

The SR peak in output S/N is therefore confirmed as the optimum point at which to operate a nonlinear pre-processor for weak signal detection, even though it was found to offer no benefit over the linear case. In order to exploit SR in this way it would be necessary to mitigate the apparent frequency dependence of the position of the SR peak.

It is suggested that the term stochastic resonance is misleading, when considered as a mechanism with potential to improve the performance of signal detectors. As the SR mechanism is evoked some sense of the onset of a region of increased benefit could be inferred from the label 'resonance'. A better description would to consider a so-called stochastic resonant system as a conventional linear system that suffers from a catastrophic nonlinear reduction or collapse in output S/N over a limited range of input S/N values, where the SR 'peak' is a recovery back to linear behaviour.

6.3 Transition and correlation detection

The transition mechanism explored in Chapters 4 and 5 was more successful in improving detection performance than SR. Yet the transition pre-processor did not outperform a conventional detector, for the Gaussian noise case. The most significant finding was the improvement in detection performance against highly impulsive noise. At low false positive rates, a single Duffing Array Element (DAE) outperforms a conventional detector in the impulsive noise case. However, the differential between nonlinear and linear may depend on input S/N. At high input S/N the benefit over the linear detector is marginal, and may increases at lower S/N. The finding is tentative but may be highly significant in underwater acoustic signal detection, where snapping shrimp produce impulsive noise that often leaves sonar systems unable to detect anything.

It was confirmed in Chapter 5 that it is possible to build a wideband sensor based on Duffing transition pre-processing. The demonstration presented in this thesis used an array of DAE's, each of which included the novel replica correlation detection process and a novel, but crude, mitigation for input signals of unknown phase.

One potential advantage of using the DAE in a wideband array is that there is no inherent (significant) inverse dependency between time and frequency as is found with other more conventional time-frequency transform methods. The use of the qualifier 'significant' is intended to convey that these findings are here considered tentative because the earlier bandwidth investigations were not comprehensive in the sense that all possible factors affecting bandwidth were explored. The implication that the resolution of the time and of the frequency axes can be fully independently set using an array of DAE's, to any desired value is not valid. The results presented later in this section tentatively support the notion of the independence of the two resolutions, but provide a qualitative demonstration of the limitations in both time and frequency resolution inherent in the data and in using the DAE detection approach itself.

Immunity to noise claims in some of the literature initially provided a strong motivation to apply the transition mechanism to detection of underwater signals. In underwater applications the noise problem is relatively severe compared to other detection problems such as non-destructive testing, where the technique has been applied. The extensive detection performance analyses conducted in this thesis clearly show the progressive degradation in performance, as the ratio of input noise power increases compared to signal power. This result is true for both SR and the transition mechanism. It is not an entirely unexpected outcome, however the results here are believed to be the most comprehensive produced to date, and robust enough to assert that these nonlinear systems are not immune to noise.

6.4 Recommendations for future work

Throughout the thesis several suggestions for future work have been made. These are summarised in this section and an assessment of their likely importance or necessity or impact is offered. As might be expected, there are great many potential avenues of research branching from the work presented in this thesis. Only those assessed as showing potential to make the most significant advances are addressed here.

It was shown in Chapter 5 that the Duffing system as a pre-processor can outperform the benchmark linear detector, when the input is dominated by highly impulsive noise. This positive result is very encouraging but it cannot be exploited until its robustness has been better established. The result requires thorough testing; by direct repetition, by repetition in some orthogonal fashion, by examination of the causes, by model development and finally by testing model predictions.

The demonstration of the wide frequency band spectral visualisation based on an array of Duffing Array Elements, was shown in Section 5.6. The demonstration was qualitatively successful, the same spectral components for real data input, could be seen in the visualisation and in the conventional spectrogram. However, a number of issues with the Duffing array concept were identified including the following:

1 A reduction in output with changing frequency either side of a peak output at one frequency. The reduction either side of the peek is very asymmetrical Starting at the peak, as frequency increases the reduction is very slow. In the other direction as frequency reduces, the reduction is very steep. All transition and therefore spectral content is completely lost.

2 A fundamental frequency axis resolution limit. The bandwidth investigation showed this resolution is poor for the replica correlation process, compared to nonlinear pre-processing with a benchmark conventional detector stage.

Future work should explore the causes of these issues, and propose improvements. Probably the most important aspect of this future work would be to establish further confirmation of a new finding presented in this thesis, relating to time/frequency resolution. The first indication of the de-coupling of the inverse relation between time and frequency resolution, as is normally found in conventional linear Fourier transform based spectrograms, was presented in Section 5.6.1.

SR was not found to offer any detection benefit when used as a pre-processor, in the scenarios presented in this thesis. However, the work presented here has highlighted the idea that descriptions of SR *enhancing* the output S/N are misleading. It is certainly the case that for a properly configured stochastically resonant system, the output S/N will fall, then rise and then fall again, as input S/N is decrease monotonically. However, the peak in output S/N attributed to SR was found to be no higher than an equivalent linear system would exhibit. Future work might concentrate on confirming this result in order to alter the general perception that adding noise can be beneficial, over an above that of an equivalent linear system. Clearly this is not directly related to the aim of this thesis, but it nevertheless might become a useful result elsewhere, if it is repeatable.

The concept of coupled nonlinear systems was introduced in Chapter 2. Although the idea did not form part of the work presented in this thesis, sufficient background research was carried out to indicate the large amount of literature on the subject. Many methods of coupling the systems are described in the literature, using from two up to quite large numbers of identical nonlinear systems. Many categories of coupling are also described in the literature, such as lag or lead coupling, phase coupling etc. The implication is there is a large number of additional ways of configuring nonlinear systems that might be explored for their impact on the detection problem. In particular, coupling several different types of system of different dimension (for example the third order Lorenz model to the second order Duffing model), appears to be completely unexplored.

The four-phase approach to managing a SoI of unknown phase is rather crude. A much more elegant linear algebraic approach using a phasor vector, similar to the steering vector used in delay-and-sum beamforming, might offer faster calculation times. Such an approach may also remove the 'holes' in performance where the phase of the input just happens to fall between the pre-set phases of the internal drive terms in the four-phase Duffing oscillator system. A step further on from this would be to explore phase locking, where the multiple Duffing systems currently used, could be reduced back to one system.

Appendix A

Normalisation and the Runge-Kutta implementation.

A.1 Duffing system frequency normalisation

Frequency normalised Duffing system used in this thesis is derived following the procedure of Wang et al. [4], the derivation is repeated here in greater detail for clarity. The time step is re-assigned so that in effect a new time step parameter τ becomes the variable rather than frequency, $t = \omega_0 \tau$ so that $dt = \omega_0 d\tau$.

$$\begin{aligned}
\frac{dx(t)}{dt} &= \frac{dx(\omega_0\tau)}{d\tau} \cdot \frac{d\tau}{dt} \\
&= \left(\frac{1}{\omega_0}\right) \cdot \frac{dx(\omega_0\tau)}{d\tau} \\
&= \left(\frac{1}{\omega_0}\right) \cdot \frac{dx_*(\tau)}{d\tau} \\
\frac{d^2x(t)}{dt^2} &= \frac{d}{dt}\left(\frac{dx(t)}{dt}\right) \cdot \frac{d\tau}{dt}
\end{aligned}$$

$$
\begin{aligned}
&= \left(\frac{1}{\omega_0}\right) . \frac{d}{dt}\left[\left(\frac{dx\left(\omega_0\tau\right)}{d\tau}\right)\left(\frac{1}{\omega_0}\right)\right] \\
&= \left(\frac{1}{\omega_0^2}\right) . \frac{d^2x\left(\omega_0\tau\right)}{d\tau^2} \\
&= \left(\frac{1}{\omega_0^2}\right) . \frac{d^2x_*\left(\tau\right)}{d\tau^2}
\end{aligned} \tag{A.1}
$$

The x_* subscript is dropped but note that the displacement 'x' is now redefined. The time is also redefined by re-labelling τ as 't', this is safe to do since the original definition of 't' is never used again. The new values of velocity and acceleration are substituted back into the original Duffing Equation 4.1 to produce the frequency normalised version of Equation A.2 (recast in 'engineering' notation).

$$
\left(\frac{1}{\omega_0^2}\right)\ddot{x} = -\delta\left(\frac{1}{\omega_0}\right)\dot{x} + \alpha x - \beta x^3 + \gamma cos\left(\omega_0 t + \phi\right) + Acos\left(\omega t\right) + n\left(t\right)
$$

letting

$$
f\left(x,t\right) = \ddot{x}
$$

$$
f\left(x,t\right) = \omega_0^2\left[\gamma cos\left(\omega_0 t + \phi\right) + n\left(t\right) + Acos\left(\omega t\right) - \delta\left(\frac{1}{\omega_0}\right)\dot{x} + \alpha x - \beta x^3\right] \tag{A.2}
$$

A.2 Fixed step Runge-Kutta solver implementation

Generalised analytic solutions to the Duffing equation are not currently available. Local linearisation techniques based on a Taylor expansion and taking the Jacobian of the system (Lyapunov's First Method,chapter 6 [111]) can provide analytic solutions over a very small region about selected fixed points. Other methods based on a Volterra series expansion [112, 110] have also been studied. However the work in this thesis is restricted to solving the Duffing nonlinear system using a numerical method, a fixed step fourth order Runge-Kutta (RK4) solver is used.

Two of the three forcing terms in the Duffing system are realised as a time-series of

discrete samples, separately simulated and input to the system. The third forcing term is the 'internal' periodic term and part of the configuration of the Duffing system. It is realised also as a set of discrete samples however these are generated as part of the numerical solver. A coded implementation of RK4 must therefore operate on a mixture of input samples and internally generated samples. This functionality is not available in standard numerical solver functions built into modelling languages such as Scilab or Matlab, a new implementation of the RK4 algorithm was required. This approach also allows the solver to operate on real data obtained from (for example) a 'wav' file. Provided the sample rate indicated in the wav file header is accurate the new RK4 solver will generate the correct output. It was also necessary to ensure the separately obtained input data set matched the sample rate of the internal data, the new RK4 implementation incorporated re-sampling to achieve this.

Using a fixed step size of h the function to be solved is set as $f(t, x)$ from Equation A.2, the constant step RK4 generic scheme that calculates the x_{n+1} displacement solution point from the previous n^{th} sample (t_n, x_n) is as follows.

$$\begin{aligned} K_1 &= h\ f(t_n, x_n) \\ K_2 &= h\ f\left(t_n + \left(\frac{h}{2}\right), x_n + \left(\frac{h}{2}\right) K_1\right) \\ K_3 &= h\ f\left(t_n + \left(\frac{h}{2}\right), x_n + \left(\frac{h}{2}\right) K_2\right) \\ K_4 &= h\ f(t_n + h, x_n + hK_3) \\ x_{n+1} &= x_n + \frac{1}{6}(K_1 + 2K_2 + 2K_3 + K_4) \end{aligned} \tag{A.3}$$

The Duffing system to be solved is a second order system. In this thesis it is reduced to a coupled system of two first order equations to make implementation in the coded model easier, and to make the code easier to read.

$$\text{Letting:} \qquad x_1 = x \quad \text{and} \quad x_2 = \frac{1}{\omega_0}\dot{x}$$

$$\dot{x_1} = \dot{x} = \omega_0 x_2$$

$$\dot{x_2} = \frac{1}{\omega_0}\ddot{x} \tag{A.4}$$

Substituting A.2 into A.4 generates the following coupled system:

$$\dot{x_1} = \omega_0 x_2$$

$$\dot{x}_2 = \omega_0 \left[\gamma cos\left(\omega_0 t + \phi\right) + n\left(t\right) + Acos\left(\omega t\right) - \delta x_2 + \alpha x_1 - \beta x_1^3\right] \tag{A.5}$$

With t and x now as discrete data representing the n$^{\text{th}}$ point generated from the solver, the first order coupled system is implemented in the RK4 solver in iterative matrix form as follows (two-element column vectors in bold font):

$$\overline{\boldsymbol{K}}_{1,n} = h\ \overline{\boldsymbol{F}}\left(t_n, \overline{\boldsymbol{x}}_n\right)$$

$$\overline{\boldsymbol{K}}_{2,n} = h\ \overline{\boldsymbol{F}}\left(t_n + \left(\frac{h}{2}\right), \overline{\boldsymbol{x}}_n + \left(\frac{h}{2}\right)\overline{\boldsymbol{K}}_{1,n}\right)$$

$$\overline{\boldsymbol{K}}_{3,n} = h\ \overline{\boldsymbol{F}}\left(t_n + \left(\frac{h}{2}\right), \overline{\boldsymbol{x}}_n + \left(\frac{h}{2}\right)\overline{\boldsymbol{K}}_{2,n}\right)$$

$$\overline{\boldsymbol{K}}_{4,n} = h\ \overline{\boldsymbol{F}}\left(t_n + h, \overline{\boldsymbol{x}}_n + h\overline{\boldsymbol{K}}_{3,n}\right)$$

$$\overline{\boldsymbol{x}}_{n+1} = \overline{\boldsymbol{x}}_n + \frac{1}{6}\left(\overline{\boldsymbol{K}}_{1,n} + 2\overline{\boldsymbol{K}}_{2,n} + 2\overline{\boldsymbol{K}}_{3,n} + \overline{\boldsymbol{K}}_{4,n}\right) \tag{A.6}$$

$$\text{where} \quad \overline{\boldsymbol{x}}_n = \begin{pmatrix} x \\ \dot{x} \end{pmatrix} = \begin{pmatrix} x_{1,n} \\ x_{2,n} \end{pmatrix} \qquad \text{and} \qquad \overline{\boldsymbol{F}}\left(t_n, \overline{\boldsymbol{x}}_n\right) = \begin{pmatrix} \dot{x}_{1,n} \\ \dot{x}_{2,n} \end{pmatrix}$$

$$= \begin{pmatrix} \omega_0 x_{2,n} \\ \omega_0 \left[\gamma cos\left(\omega_0 t_n + \phi\right) + n\left(t_n\right) + Acos\left(\omega t_n\right) - \delta x_{2,n} + \alpha x_{1,n} - \beta x_{1,n}^3\right] \end{pmatrix}$$

The input data represented by the terms $Acos(\omega t_n) + n\left(t_n\right)$ and generated separately can now be replaced by an array of sample points $\overline{\boldsymbol{a}}_k$, and so the RK4 solver of A.6

above can be modified as follows:

$$\text{With re-sampling such that} \quad (2n-1) = k$$

$$\text{then} \quad A cos(\omega t_n) + n\,(t_n) \Rightarrow \overline{\boldsymbol{a}}_k = \begin{pmatrix} 0 \\ a_k \end{pmatrix}$$

Separating out the input terms from the earlier definition of $\overline{\boldsymbol{x}}_n$ allows a re-definition of the function as: $\overline{\boldsymbol{F}}\,(t, \overline{\boldsymbol{x}}_n) \Rightarrow \overline{\boldsymbol{F}}\,(t, \overline{\boldsymbol{x}}_n, \overline{\boldsymbol{a}}_k)$. The function the new RK4 algorithm operates on is therefore defined as:

$$\overline{\boldsymbol{F}}\,(t, \overline{\boldsymbol{x}}_n, \overline{\boldsymbol{a}}_k) = \omega_0 \left[\begin{pmatrix} x_{2,n} \\ \left[\gamma cos\,(\omega_0 t_n + \phi) - \delta x_{2,n} + \alpha x_{1,n} - \beta x_{1,n}^3\right] \end{pmatrix} + \begin{pmatrix} 0 \\ a_k \end{pmatrix} \right] \tag{A.7}$$

The RK4 solver algorithm therefore becomes:

$$\begin{aligned}
\overline{\boldsymbol{K}}_{1,n,k} &= h\ \overline{\boldsymbol{F}}\,(t_n, \overline{\boldsymbol{x}}_n, \overline{\boldsymbol{a}}_k) \\
\overline{\boldsymbol{K}}_{2,n,(k+1)} &= h\ \overline{\boldsymbol{F}}\left(t_n + \left(\frac{h}{2}\right)\ ,\ \overline{\boldsymbol{x}}_n + \left(\frac{h}{2}\right)\overline{\boldsymbol{K}}_{1,n,k}\ ,\ \overline{\boldsymbol{a}}_{k+1}\right) \\
\overline{\boldsymbol{K}}_{3,n,(k+1)} &= h\ \overline{\boldsymbol{F}}\left(t_n + \left(\frac{h}{2}\right)\ ,\ \overline{\boldsymbol{x}}_n + \left(\frac{h}{2}\right)\overline{\boldsymbol{K}}_{2,n,(k+1)}\ ,\ \overline{\boldsymbol{a}}_{k+1}\right) \\
\overline{\boldsymbol{K}}_{4,n,(k+2)} &= h\ \overline{\boldsymbol{F}}\left(t_n + h\ ,\ \overline{\boldsymbol{x}}_n + h\overline{\boldsymbol{K}}_{3,n,(k+1)}\ ,\ \overline{\boldsymbol{a}}_{k+2}\right)
\end{aligned} \tag{A.8}$$

The input data points are now separated out from the $\overline{\boldsymbol{x}}_n$ values. The input data points increment to the next value through the four Runge-Kutta stages whereas x and t do not. Provided the re-sampling of the input perturbation has been carried out correctly so that it generates twice as many input data points at half the time step, then the $(k+2)^{\text{th}}$ input point should always coincide in time with the $(n+1)^{\text{th}}$ point.

References

[1] May R M, *Simple mathematical models with very complicated dynamics.*, Nature. 1976;261(5560):459 – 467

[2] Galdi G P, *An introduction to the mathematical theory of the Navier-Stokes equations*, 2nd edition, Springer Science and Business Media, 2011

[3] Stephani H, Kramer D, MacCallum M, Hoenselaers C, and Herlt E, *Exact Solutions of Einstein's Field Equations*, 2nd edition, Cambridge University Press, 2003

[4] Wang G Y, Chen D J, Lin J Y, and Chen X, *The application of chaotic oscillators to weak signal detection*, IEEE T. Ind. Electron. April 1999;46(2):440 – 444

[5] Li Y and Yang B J, *Chaotic system for the detection of periodic signals under the background of strong noise*, Chinese Sci. Bull. March 2003;48(5):508 – 510

[6] von Wagner U, *On Double Crater-Like Probability Density Functions of a Duffing Oscillator Subjected to Harmonic and Stochastic Excitation*, Nonlinear Dynam. 2002;28(3 - 4):343 – 355

[7] Jin T and Zhang H, *Statistical approach to weak signal detection and estimation using Duffing chaotic oscillators*, Sci. China Ser. F. November 2011;54(11):2324 – 2337

[8] Deng X, Liu H, and Long T, *A new complex Duffing oscillator used in complex signal detection*, Chinese Sci. Bull. June 2012;57(17):2185 – 2191

REFERENCES

[9] Inchiosa M E and Bulsara A R, *Nonlinear dynamic elements with noisy sinusoidal forcing: Enhancing response via nonlinear coupling*, Phys. Rev. E. 1995;52:327 – 339

[10] Pecora L M, Carroll T L, Johnson G A, Mar D J, and Heagy J F, *Fundamentals of synchronization in chaotic systems, concepts, and applications*, Chaos. December 1997;7(4):520 – 543

[11] Rulkov N, Sushchik M, Tsimring L, and Abarbanel H, *Generalized synchronization of chaos in directionally coupled chaotic systems*, Phys. Rev. E. February 1995;51(2):980 – 994

[12] Raj S P and Rajasekar S, *Migration control in two coupled Duffing oscillators*, Phys. Rev. E. May 1997;55:6237 – 6240

[13] Rosenblum M G, Pikovsky A S, and u Kurths J, *Phase Synchronization of Chaotic Oscillators*, Phys. Rev. Lett. March 1996;76(11):1804 – 1807

[14] ——, *From Phase to Lag Synchronization in Coupled Chaotic Oscillators*, Phys. Rev. Lett. June 1997;78(22):4193 – 4196

[15] Pikovsky A S and Rosenblum M G, *Phase synchronization of regular and chaotic self-sustained oscillators*, in: *Synchronization: Theory and application*, (Editors) Pikovsky A and Maistrenko Y, volume 109 of *NATO SCIENCE SERIES, SERIES II: MATHEMATICS, PHYSICS AND CHEMISTRY*, NATO Adv Study Inst, SPRINGER, PO BOX 17, 3300 AA DORDRECHT, NETHERLANDS, 2003 (pages 187 – 219), conference of the NATO-Advanced-Study-Institute on Synchronization, YALTA, UKRAINE, MAY 19-JUN 01, 2002

[16] Lifshitz R and Cross M C, *Response of parametrically driven nonlinear coupled oscillators with application to micromechanical and nanomechanical resonator arrays*, Phys. Rev. B. 1 April 2003;67(13)

[17] Yeh J P and Wu K L, *A simple method to synchronize chaotic systems and its application to secure communications*, Math. Comput. Model. May 2008;47(9 - 10):894 – 902

[18] Li N, Li L, Yang D, Zhao Y, and Yang Y, *The Research of Weak Fault Signal Detection Based on the Duffing Oscillator Coupled Synchronization*, in: *Proceedings of the Fourth International Workshop on Chaos-Fractals Theories and Applications (IWCFTA 2011)*, IEEE, IEEE Computer Society, Los Alamitos, CA, USA, 2011 (pages 319 – 323), fourth International Workshop on Chaos-Fractals Theories and Applications (IWCFTA 2011), 19-21 Oct. 2011, Hangzhou, China

[19] Wu Y, Huang S, and Xie W, *Stochastic Resonance Phenomenon of Two-coupled Duffing Oscillator and its Application on Weak Signal Detection.*, Sensors & Transducers. 2014;169:1726–5479

[20] Asdi A and Tewfik A, *Detection of weak signals using adaptive stochastic resonance*, in: *1995 International conference on acoustics, speech, and signal processing - conference proceedings, vols 1-5*, BD41X, IEEE, Signal Proc Soc, I E E E, 345 E 47TH ST, NEW YORK, NY 10017, 1995 (pages 1332 – 1335), 1995 International Conference on Acoustics, Speech, and Signal Processing, DETROIT, MI, MAY 09-12, 1995

[21] Kang L, Fu-Zhong W, Guang-Lu Z, and Wei-Hong F, *A self-adaptive stochastic resonance system design and study in chaotic interference*, Chinese Phys. B. December 2013;22(12)

[22] Ma Y, Duan F, Chapeau-Blondeau F, and Abbott D, *Weak-Periodic Stochastic Resonance in a Parallel Array of Static Nonlinearities*, PLoS ONE. 11 March 2013;8(3)

REFERENCES

[23] Chapeau-Blondeau F, Duan F, and Abbott D, *Signal-to-noise ratio of a dynamical saturating system: Switching from stochastic resonator to signal processor*, Physica A. 15 April 2008;387(11):2394 – 2402

[24] Khovanov I A, *Array enhancement of stochastic synchronization and signal-to-noise ratio gain in the nonlinear regime of signal transmission*, Phys. Rev. E. January 2008;77(1 - 1)

[25] Hanggi P, Inchiosa M E, Fogliatti D, and Bulsara A R, *Nonlinear stochastic resonance: The saga of anomalous output-input gain*, Phys. Rev. E. November 2000;62(5 - A):6155 – 6163, dOI = 10.1103/PhysRevE.62.6155

[26] Li Y, Yang B, Yuan Y, and Liu X, *Analysis of a kind of Duffing oscillator system used to detect weak signals*, Chinese Phys. April 2007;16(4):1072 – 1076

[27] Liu J and Li Z, *Lowering the signal-to-noise ratio wall for energy detection using parameter-induced stochastic resonator*, IET Commun. 2 January 2015; 9(1):101 – 107

[28] Burdic W S, *Underwater acoustic system analysis*, Prentice Hall, 1984

[29] Oppenheim A V and Verghese G C, *6.011 Introduction to Communication, Control, and Signal Processing, Spring 2010: Course Notes: Signals, Systems and Inference [Internet]*, Massachusetts Institute of Technology, MIT OpenCourseWare (OCW). 2010, [Accessed 2015 Apr 21]; Available from: http://ocw.mit.edu/courses/electrical-engineering-and-computer-science/6-011-introduction-to-communication-control-and-signal-processing-spring-2010/readings/

[30] Schwartz M and Shaw L, *Signal processing: Discrete spectral analysis, detection, and estimation*, McGraw-Hill Companies, 1975

[31] Fawcett T, *An introduction to ROC analysis*, Pattern Recogn. Lett. June 2006; 27(8):861 – 874

[32] He X, Metz C E, Tsui B M W, Links J M, and Frey E C, *Three-class ROC analysis-A decision theoretic approach under the ideal observer framework*, IEEE T Med Imaging. 2006;25(5):571 – 581

[33] Landgrebe T C W and Duin R P W, *Approximating the multiclass ROC by pairwise analysis*, Pattern Recogn Lett. 2007;28(13):1747 – 1758

[34] Rousseau D, Anand G V, and Chapeau-Blondeau F, *Noise-enhanced nonlinear detector to improve signal detection in non-Gaussian noise*, Signal Process. 2006;86(11):3456 – 3465

[35] Hari V N, Anand G V, Premkumar A B, and Madhukumar A S, *Design and performance analysis of a signal detector based on suprathreshold stochastic resonance*, Signal Process. July 2012;92(7):1745 – 1757

[36] Olson C C, Nichols J M, Todd M D, Michalowicz J V, and Bucholtz F, *Coupling Evolutionary Algorithms With Nonlinear Dynamical Systems: An Efficient Tool for Excitation Design and Optimization*, IEEE T. Evolut. Comput. August 2011;15(4):437 – 443

[37] Thompson J M T and Stewart H, 2 edition, John Wiley and Sons, Chichester, 2002

[38] Duffing G, *Erzwungene Schwingungen bei veränderlicher Eigenfrequenz und ihre technische Bedeutung*, 41 - 42, F. Vieweg & sohn, 1918

[39] Kovacic I and Brennan M J, *The Duffing equation: Nonlinear oscillators and their behaviour*, John Wiley and Sons, 2011

[40] Jung P and Hänggi P, *Amplification of small signals via stochastic resonance*, Phy. Rev. A. 1991;44(12):8032

[41] Wang J, He Q, and Kong F, *Adaptive Multiscale Noise Tuning Stochastic Resonance for Health Diagnosis of Rolling Element Bearings*, IEEE T. Instrum. Meas. February 2015;64(2):564 – 577

[42] Kwasniok F, *Analysis and modelling of glacial climate transitions using simple dynamical systems*, Philos T Roy Soc A. 2013;371(1991):20110472

[43] Benzi R, Sutera A, and Vulpiani A, *The mechanism of stochastic resonance*, J. Phys. A: Math. Gen. 1981;14(11):L453 – L457

[44] Zhang H, Xu B, Li J, and Jiang Z P, *Evaluation of the method based on PSR techniques for target detection in reverberation*, J. Phys. A: Math. Theor. 2009; 42(19):195004

[45] Casado-Pascual J, Gómez-Ordóñez J, Morillo M, and Hänggi P, *Subthreshold stochastic resonance: Rectangular signals can cause anomalous large gains*, Phy. Rev. E. 2003;68(6):061104

[46] Fox R, *Stochastic resonance in a double well*, Phys. Rev. A. 15 April 1989; 39(8):4148 – 4153

[47] Gammaitoni L, Hanggi P, Jung P, and Marchesoni F, *Stochastic resonance*, Rev. Mod. Phys. January 1998;70(1):223 – 287

[48] Barreira L and Pesin Y, *Lectures on Lyapunov exponents and smooth ergodic theory*, Proc Symp Pure Math. 2001;69:3 – 90

[49] Wolf A, Swift J B, Swinney H L, and Vastano J A, *Determining Lyapunov exponents from a time series*, Physica D. 1985;16(3):285 – 317

[50] Eckmann J P, Kamphorst S O, Ruelle D, Ciliberto S, et al., *Liapunov exponents from time series*, Phys. Rev. A. December 1986;34(6):4971 – 4979

[51] Sano M and Sawada Y, *Measurement of the Lyapunov Spectrum from a Chaotic Time Series*, Phys. Rev. Lett. September 1985;55(10):1082 – 1085

[52] Zeni A R and Gallas J A C, *Lyapunov exponents for a Duffing oscillator*, Physica D. 1995;89(1 - 2):71 – 82

[53] Sprott J C, *Numerical calculation of largest Lyapunov exponent. [Internet]*, Department of Physics, University of Wisconsin, Madison. 1997, [Accessed 2012 Apr 12]; Available from: http://sprott.physics.wisc.edu/chaos/lyapexp.htm

[54] Kantz H and Schreiber T, 2 edition, Cambridge university press, 2004

[55] Ginelli F, Poggi P, Turchi A, ' H C, Livi R, and Politi A, *Characterizing Dynamics with Covariant Lyapunov Vectors*, Phys. Rev. Lett. September 2007; 99:130601

[56] Pazó D, Szendro I G, López J M, and Rodríguez M A, *Structure of characteristic Lyapunov vectors in spatiotemporal chaos* , Phys. Rev. E. July 2008;78(05):016209

[57] Bulsara A R and Gammaitoni L, *Tuning in to noise*, Phys. Today. March 1996; 49(3):39 – 45

[58] Hanggi P, Talkner P, and Borkovec M, *Reaction-rate theory - 50 years after Kramers*, Rev. Mod. Phys. April 1990;62(2):251 – 341

[59] Yi T, Xiaomei X, and Minghui Z, *Application of stochastic resonance theory in weak underwater acoustic signal detection*, in: *Communication Technology (ICCT), 2010 12th IEEE International Conference on*, IEEE, 2010 (pages 1268 – 1270)

[60] McNamara B and Wiesenfeld K, *Theory of stochastic resonance*, Phys. Rev. A. 1 May 1989;39(9):4854 – 4869

[61] Gammaitoni L, Marchesoni F, Menichellasaetta E, and Santucci S, *Stochastic resonance in bistable systems*, Phys. Rev. Lett. 23 January 1989;62(4):349 – 352

[62] Gammaitoni L, Marchesoni F, Menichella-Saetta E, and Santucci S, *Gammaitoni et al. Reply*, Phys. Rev. Lett. November 1990;65:2607 – 2607

[63] Stocks N G, Stein N D, and McClintock P V E, *Stochastic resonance in monostable systems*, J. Phys. A: Math. Gen. 1993;26(7):L385

[64] Benzi R, Parisi G, Sutera A, and Vulpiani A, *A theory of stochastic resonance in climatic-change*, SIAM J Appl Math. 1983;43(3):565 – 578

[65] Lai Z H and Leng Y G, *Generalized Parameter-Adjusted Stochastic Resonance of Duffing Oscillator and Its Application to Weak-Signal Detection*, SENSORS. September 2015;15(9):21327 – 21349, dOI = 10.3390/s150921327

[66] McNamara B, Wiesenfeld K, and Roy R, *Observation of stochastic resonance in a ring laser*, Phys. Rev. Lett. 20 June 1988;60(25):2626 – 2629

[67] Miloshevich G, Khomeriki R, and Ruffo S, *Stochastic Resonance in the Fermi-Pasta-Ulam Chain*, Phys. Rev. Lett. 2009;102(2):020602

[68] Nicolis G, Nicolis C, and McKernan D, *Stochastic resonance in chaotic dynamics*, J. Stat. Phys. January 1993;70(1 - 2):125 – 139, Nato advanced research workshop : Stochastic resonance in physics and biology, san diego, ca, mar 30-apr 03, 1992

[69] Wang F Z, Chen W S, Qin G R, Guo D Y, and Liu J L, *Experimental analysis of stochastic resonance in a Duffing system*, Chinese Phys. Lett. January 2003; 20(1):28 – 30

[70] Arathi S, Rajasekar S, and Kurths J, *Characteristics of Stochastic Resonance in Asymmetric Duffing Oscillator*, Int. J. Bifurcat. Chaos. 2011;21(09):2729 – 2739

[71] Dykman M, Mannella R, McClintock P, and Stocks N, *Stochastic resonance in bistable systems - comment*, Phys. Rev. Lett. 12 November 1990;65(20):2606

[72] Rousseau D and Chapeau-Blondeau F, *Stochastic resonance and improvement by noise in optimal detection strategies*, Digit. Signal Process. January 2005; 15(1):19 – 32

[73] Chen H, Varshney P K, Kay S M, and Michels J H, *Theory of the stochastic resonance effect in signal detection: Part I - Fixed detectors*, IEEE T. Signal

Proces. July 2007;55(7 - 1):3172 – 3184, IEEE International Conference on Acoustics, Speech and Signal Processing, Toulouse, FRANCE, MAY 14-19, 2006

[74] Kay S, *Noise Enhanced Detection as a Special Case of Randomization*, IEEE Signal Proc. Let. 2008;15(416IL):709 – 712

[75] Inchiosa M E and Bulsara A R, *Signal detection statistics of stochastic resonators*, Phys. Rev. E. March 1996;53(3):R2021 – R2024

[76] Rajasekar S, Jeyakumari S, Chinnathambi V, and Sanjuan M A F, *Role of depth and location of minima of a double-well potential on vibrational resonance*, J. Phys. A-Math. Theor. 19 November 2010;43(46)

[77] Aldridge J S and Cleland A N, *Noise-enabled precision measurements of a duffing nanomechanical resonator*, Phys. Rev. Lett. 22 April 2005;94(15)

[78] Kosko B and Mitaim S, *Robust stochastic resonance: Signal detection and adaptation in impulsive noise*, Phys. Rev. E. November 2001;64(5 - 1)

[79] Guo G and Mandal M, *Design of stochastic-resonator-based detector using bistable system*, in: *2010 International conference on signal processing and communications (spcom)*, BTO74, IEEE, IEEE, 345 E 47TH ST, NEW YORK, NY 10017 USA, 2010 International Conference on Signal Processing and Communications, Indian Inst Sci, Bangalore, INDIA, JUL 18-21, 2010

[80] Benzi R, Parisi G, Sutera A, and Vulpiani A, *Stochastic resonance in climatic change*, Tellus. 1982;34(1):10 – 16

[81] Mitaim S and Kosko B, *Adaptive stochastic resonance*, Pr. Inst. Electr. Elect. November 1998;86(11):2152 – 2183

[82] Gammaitoni L, Hanggi P, Jung P, and Marchesoni F, *Stochastic Resonance: A remarkable idea that changed our perception of noise*, Eur. Phys. J. B. May 2009;69(1):1 – 3

[83] Li L F and Zhu J Y, *Gravitational wave detection: Stochastic resonance method with matched filtering*, Gen. Relat. Gravit. November 2011;43(11):2991 – 3000

[84] Su L, Yang Q, Zhang Y, and Li J, *Noise Immunity of Duffing Oscillator and its Applications in Weak UWB Signal Detection.*, Journal of Networks. 2012;7(3)

[85] Ye Q, Huang R, He X, and Zhang C, *A SR-based radon transform to extract weak lines from noise images*, in: *Image Processing, 2003. ICIP 2003. Proceedings. 2003 International Conference on*, volume 1, IEEE, 2003 (pages I – 849)

[86] Shu-Yao J, Fei Y, Ke-Yu C, and En C, *Application of stochastic resonance technology in underwater acoustic weak signal detection*, in: *OCEANS 2016-Shanghai*, IEEE, 2016 (pages 1 – 5)

[87] Birx D L and Pipenberg S J, *Chaotic oscillators and complex mapping feed forward networks (CMFFNs) for signal detection in noisy environments*, in: *IJCNN International Joint Conference on Neural Networks (Cat. No.92CH3114-6)*, IEEE; Int. Neural Network Soc, IEEE, New York, NY, USA, 1992 (pages 881 – 8 – vol – 2), IJCNN International Joint Conference on Neural Networks, 7-11 June 1992, Baltimore, MD, USA

[88] Glenn C M and Hayes S, *Weak signal detection by small-perturbation control of chaotic orbits*, in: *Microwave Symposium Digest, 1996., IEEE MTT-S International*, volume 3, 1996 (pages 1883 – 1886 – vol – 3)

[89] Wang J, Zhou J, and Peng B, *Weak signal detection method based on Duffing oscillator*, Kybernetes. 2009;38(10):1662 – 1668

[90] Wang G Y and He S L, *A quantitative study on detection and estimation of weak signals by using chaotic duffing oscillators*, IEEE T. Circuits-I. July 2003; 50(7):945 – 953

[91] Brennan M J, Kovacic I, Carrella A, and Waters T P, *On the jump-up and jump-down frequencies of the Duffing oscillator*, J. Sound Vib. 23 December 2008;318(4 - 5):1250 – 1261

[92] Ho C, Lang Z Q, and Billings S A, *A frequency domain analysis of the effects of nonlinear damping on the Duffing equation*, Mech. Syst. Signal Pr. 2014; 45(1):49 – 67

[93] Huang P, Pi Y, and Zhao Z, *Weak GPS Signal Acquisition Algorithm Based on Chaotic Oscillator*, Eurasip J. Adv. Sig. Pr. 2009;(862618)

[94] Li C and Qu L, *Applications of chaotic oscillator in machinery fault diagnosis*, Mech. Syst. Signal Pr. January 2007;21(1):257 – 269

[95] Hu N Q and Wen X S, *The application of Duffing oscillator in characteristic signal detection of early fault*, J. Sound Vib. 11 December 2003;268(5):917 – 931

[96] Wang H and Shi M, *Detection of line-spectrum of radiated noises from underwater target based on chaotic system*, in: *2013 IEEE International Conference on Signal Processing, Communication and Computing (ICSPCC 2013)*, IEEE, Piscataway, NJ, USA, 2013 (pages 4 – pp), 2013 IEEE International Conference on Signal Processing, Communication and Computing (ICSPCC 2013), 5-8 Aug. 2013, KunMing, China

[97] Zheng S, Guo H, Li Y, Wang B, and Zhang P, *A new method for detecting line spectrum of ship-radiated noise using Duffing oscillator*, Chinese Sci. Bull. July 2007;52(14):1906 – 1912

[98] Li Y, Yang B J, Badal J, Zhao X P, Lin H B, and Li R L, *Chaotic system detection of weak seismic signals*, Geophys. J. Int. September 2009;178(3):1493 – 1522

[99] Song W, Deng S, Yang J, and Cheng Q, *Tool Wear Detection Based on Duffing-Holmes Oscillator*, Math. Probl. Eng. 2008;(510406)

[100] Chen H Y, Lv J T, Zhang S Q, Zhang L G, and Li J, *Chaos weak signal detecting algorithm and its application in the ultrasonic Doppler bloodstream speed measuring*, in: *7th International Symposium on Measurement Technology and Intelligent Instruments*, (Editors) Jiang X J and Whitehouse D J, volume 13 of *JOURNAL OF PHYSICS CONFERENCE SERIES*, IOP PUBLISHING LTD, DIRAC HOUSE, TEMPLE BACK, BRISTOL BS1 6BE, ENGLAND, 2005 (pages 320 – 324), 7Th Symposium on Measurement Technology and Intelligent Instruments, Univ Huddersfield, Huddersfield, ENGLAND, SEP 06-08, 2005

[101] Gao S L, Zhong S C, Wei K, and Ma H, *Weak signal detection based on chaos and stochastic resonance*, Acta Phys. Sin. 2012;61(18)

[102] Xie T, Wei X, and Yu R, *Noise Immunity Analysis in External Excitation Chaotic Oscillator Detecting System*, in: *Proceedings 2010 International Conference on Intelligent System Design and Engineering Application (ISDEA 2010)*, Hunan Univ. of Technol., IEEE Computer Society, Los Alamitos, CA, USA, 2010 (pages 1013 – 1016), 2010 International Conference on Intelligent System Design and Engineering Application (ISDEA 2010), 13-14 Oct. 2010, Changsha, China

[103] Casado-Pascual J, Cubero D, and Baltanás J P, *Stochastic resonance with weak monochromatic driving: Gains above unity induced by high-frequency signals*, EUROPHYS LETT. 2007;77(5):50004

[104] Wenz G M, *Acoustic ambient noise in the ocean: Spectra and sources*, The Journal of the Acoustical Society of America. 1962;34(12):1936 – 1956

[105] Lyons A P and Abraham D A, *Statistical characterization of high-frequency shallow-water seafloor backscatter*, J. Acoust. Soc. Am. September 1999;106(3 - 1):1307 – 1315

[106] Versluis M, Schmitz B, von der Heydt A, and Lohse D, *How snapping shrimp snap: Through cavitating bubbles.*, Science. 2000;289(5487):2114 – 2117

[107] Everest F A, Young R W, and Johnson M W, *Acoustical characteristics of noise produced by snapping shrimp*, J. Acoust. Soc. Am. March 1948;20(2):137–142

[108] Morillo M and Gómez-Ordóñez J, *Amplification and distortion of a periodic rectangular driving signal by a noisy bistable system.*, Phys. Rev. E. 1995; 51(2):999 – 1003

[109] Kanamaru T, *Duffing oscillator [Internet]*, Scholarpedia. 2008, [Accessed 2017 Aug 30]; Available from: http://www.scholarpedia.org/article/Duffing_oscillator

[110] Li L M and Billings S A, *Analysis of nonlinear oscillators using Volterra series in the frequency domain*, J. Sound Vib. 17 January 2011;330(2):337 – 355

[111] Leigh J R, *Essentials of nonlinear control theory*, IET, 1983

[112] Worden K and Manson G, *Random vibrations of a Duffing oscillator using the Volterra series*, J. Sound Vib. 1998;217(4):781 – 789

[113] Yusufoglu E A, *Numerical solution of Duffing equation by the Laplace decomposition algorithm*, Appl. Math. Comput. 15 June 2006;177(2):572 – 580

[114] Enterprises S and contributors, *Scilab online help: number properties. [Internet]*, Scilab Enterprises. 2011, [Accessed 2015 July 20]; Available from: http://www.scilab.org/

[115] Fitzpatrick R, *Integration of ODE's: Runge-Kutta methods*. March 2006, website. University of Texas at Austin. http://farside.ph.utexas.edu/teaching/329/lectures/node35.html. Page accessed 19th May 2014

[116] Grebogi C, Ott E, and Yorke J, *Critical exponent of chaotic transients in nonlinear dynamic-systems*, Phys. Rev. Lett. 15 September 1986;57(11):1284 – 1287

[117] ——, *Crises, sudden changes in chaotic attractors, and transient chaos*, Physica D. 1983;7(1 - 3):181 – 200

[118] Bermudez-Gomez C R, Enriquez-Caldera R, and Martinez-Carballido J, *Chirp signal detection using the Duffing oscillator*, in: *2012 22nd International Conference on, Electrical Communications and Computers (CONIELECOMP)*, IEEE, 2012 (pages 344 – 349)

[119] Chafe C, Sethi U, Davis G, and contributors, *Sound, Digital Sound, and Massive Sound Media: Underwater Sound Pages. [Internet]*, Center for Computer Research in Music and Acoustics: Stanford University. 2005 - Accessed - 2012 - September - 12; Available from: Https://Ccrma.Stanford.Edu/ cc/soco/underwater/sounds.Html